

**DENSITY FUNCTIONAL THEORY STUDY OF ALCOHOL
SYNTHESIS REACTIONS ON ALKALI-PROMOTED MO₂C
CATALYSTS**

A Dissertation
Presented to
The Academic Faculty

by

Liwei Li

In Partial Fulfillment
of the Requirements for the Degree
Doctor of Philosophy in the
School of Chemical and Biomolecular Engineering

Georgia Institute of Technology
May 2014

COPYRIGHT 2014 BY LIWEI LI

**DENSITY FUNCTIONAL THEORY STUDY OF ALCOHOL
SYNTHESIS REACTIONS ON ALKALI-PROMOTED MO₂C
CATALYSTS**

Approved by:

Dr. David S. Sholl, Advisor
School of Chemical and Biomolecular
Engineering
Georgia Institute of Technology

Dr. Christopher W. Jones
School of Chemical and Biomolecular
Engineering
Georgia Institute of Technology

Dr. Pradeep K. Agrawal
School of Chemical and Biomolecular
Engineering
Georgia Institute of Technology

Dr. Carsten Sievers
School of Chemical and Biomolecular
Engineering
Georgia Institute of Technology

Dr. Jean-Luc Brédas
School of Chemistry and Biochemistry
Georgia Institute of Technology

Date Approved: [March 24, 2014]

To my parents, Feng Li and Li Gong

ACKNOWLEDGEMENTS

First of all, I would like to express my sincere gratitude to my advisor Dr. David Sholl. When I first joined the group 5 years ago, I was a freshman in graduate school, with limited English proficiency, zero experience in academic presentation, and absolutely no idea about molecular modeling and DFT. It is his encouragement, advice and support that guided me through those years during my Ph.D. Besides all the invaluable advice he has given in my research, his work enthusiasm and work ethic have set an excellent example for me and will continue to be a guideline in my future career.

I would like to express my appreciation to Dr. Christopher Jones, Dr. Pradeep Agrawal at Georgia Institute of Technology and Dr. Robert Davis at University of Virginia, whom I collaborated with in my thesis project. Their expertise in heterogeneous catalysis has provided numerous useful insights and inspirations to me to complete this thesis. I would also like to thank Dr. Carsten Sievers and Dr. Jean-Luc Brédas, who serves on my committee, for their helpful comments and suggestions.

I would like to offer my special thanks to Dr. Daniela Ferrari and Dr. David Barton from The Dow Chemical Company. None of this work would have been possible without valuable discussions with them and funding from the company.

I would also like to thank many previous and current Sholl group members: Dr. Shiqiang Hao, Dr. Taku Watanabe, Dr. Thomas Manz, Dr. Ji Zang, Dr. Seda Keskin, Dr. Sang-Eun Jee, Dr. Jeong Woo Han, Dr. Ki Chul Kim, Dr. Mohamad Kassae, Dr. Xuerong Shi, Dr. Hanjun Fang, Dr. Iyad Hijazi, Dr. Salah Boulfefel, Dr. Veronika Walkosz, Dr. Rongshun Zhu, Dr. Melissa Lucero, Dr. Sung Gu Kang, Dr. Emmanuel

Haldoupis, Dieh Teng, Ambarish Kulkarni, Nita Chandrasekhar, Timothy van Heest, Daniel Wei, Kelly Nicholson, Rohan Awati, Alex Fergusson, Namory Keita, Jaeyub Chung, Seung Won Choi, Jason Gee, Jeff Camp, Hakan Demir. Specifically, I would like to thank Dr. Shiqiang Hao for his generous help in teaching me to perform DFT calculation when I first joined the group. I would like to thank Dr. Jeong Woo Han, who derived many results on the bulk and surface structures of Mo_2C (in Chapter 3 of this thesis) which laid out the basis of my work. I would also like to thank Dr. Thomas Manz, who developed the DDEC charges which is used extensively in my thesis, and gave many useful comments and suggestions. Besides Sholl group members, I would like to acknowledge students in our collaborators' group: Dr. Michael Morrill from Jones Group and Dr. Heng Shou from Davis group who performed the experiments described in this thesis and provided a lot of valuable discussions.

Finally, I would like to express my very great appreciation to my mother, Li Gong, and my farther Feng Li, who always love and support me.

Liwei Li, Atlanta, 03/12/2014

TABLE OF CONTENTS

	Page
ACKNOWLEDGEMENTS	iv
LIST OF TABLES	x
LIST OF FIGURES	xii
SUMMARY	xvii
<u>CHAPTER</u>	
1 INTRODUCTION	1
1.1 Alcohol synthesis from syngas reactions	1
1.2 Alkali promoted Mo ₂ C as a promising catalyst	2
1.3 Thesis summary	3
1.4 References	7
2 COMPUTATIONAL METHODS	10
3 DETERMINATION OF REPRESENTATIVE SURFACE STRUCTURE OF Mo ₂ C FOR ALCOHOL SYNTHESIS REACTIONS	15
3.1 Introduction	15
3.2 Computational methods	18
3.3 Results and Discussion	19
3.3.1 Bulk structure of Mo ₂ C	19
3.3.2 Surface structure and particle shape of Mo ₂ C	20
3.3.3 K and Rb adsorption on Mo ₂ C	23
3.3.4 Surface reconstruction of Mo ₂ C (001) surface	26
3.4 Conclusions	29
3.5 References	31

APPENDIX 3.A	35
APPENDIX 3.B	36
APPENDIX 3.C	39
4 ANALYSIS OF SYNGAS REACTION NETWORK TO IDENTIFY THE SELECTIVITY DETERMINING ELEMENTARY STEPS	42
4.1 Introduction	42
4.2 Computational methods	44
4.3 Results and Discussion	45
4.3.1 Bulk and surface structure of Mo ₂ C catalyst	45
4.3.2 Syngas reaction network	46
4.3.3 Adsorption of reaction intermediates	48
4.3.4 Approximation of activation energy	50
4.3.5 Microkinetic model	52
4.3.6 Results	56
4.4 Conclusions	69
4.5 References	72
APPENDIX 4.A	78
APPENDIX 4.B	97
APPENDIX 4.C	99
APPENDIX 4.D	104
5 INVESTIGATION OF ALKALI PROMOTER FORMATION ON MO ₂ C CATALYSTS FOR ALCOHOL SYNTHESIS REACTIONS - A JOINT STUDY OF INFRARED SPECTROSCOPY AND DFT	105
5.1 Introduction	105
5.2 Methods	108
5.2.1 Catalyst synthesis	108

5.2.2	Diffuse reflectance Infrared Fourier transform spectroscopy	109
5.2.3	Computational methods	110
5.3	Results and Discussion	113
5.3.1	Infrared spectroscopy results and DFT calculation of CO adsorption on bare Mo ₂ C catalysts	113
5.3.2	Infrared spectroscopy results and DFT calculation of CO adsorption on Rb-promoted Mo ₂ C catalysts	118
5.3.3	Rb promoter formation mechanism on Mo ₂ C catalysts	123
5.4	Conclusions	124
5.5	References	125
	APPENDIX 5.A	129
6	INVESTIGATION OF ALKALI PROMOTER'S EFFECT ON CO INSERTION ON MO ₂ C CATALYSTS	131
6.1	Introduction	131
6.2	Computational methods	132
6.3	Results and Discussion	135
6.3.1	Adsorption of RbO promoter and CO insertion reaction intermediates on Mo ₂ C (001) surface	135
6.3.2	Charge analysis of RbO promoter and CO insertion reaction intermediates on Mo ₂ C (001) surface	138
6.3.3	Investigation of the effect of RbO on the transition state of CO insertion reaction on Mo ₂ C (001) surface	141
6.4	Conclusions	145
6.5	References	146
7	ON THE RELATIONSHIP BETWEEN MO K EDGE ENERGIES AND DFT COMPUTED PARTIAL CHARGES	147
7.1	Introduction	147
7.2	Computational and experimental methods	149

7.3 Results and Discussion	150
7.4 Conclusions	160
7.5 References	161
APPENDIX 7.A	165
8 CONCLUSIONS	170

LIST OF TABLES

	Page
Table 3.1: The adsorption energies and dipole moments of K in the limit of zero coverage for the seven surfaces obtained as described in the text.	26
Table 3.B.1: Unit cell vectors for a (1×1) surface used in this chapter.	36
Table 3.B.2: Fractional coordinates for a (1×1) unreconstructed bare Mo ₂ C (001) surface.	37
Table 3.B.3: Fractional coordinates for a (1×1) reconstructed bare Mo ₂ C (001) surface.	38
Table 3.C.1: Unit cell vectors for a (2×2) surface used in this chapter.	39
Table 3.C.2: Fractional coordinates for K adsorbed on a (2×2) unreconstructed bare Mo ₂ C (001) surface.	40
Table 3.C.3: Fractional coordinates for K adsorbed on a (2×2) reconstructed bare Mo ₂ C (001) surface.	41
Table 4.1: Adsorption energy of gas phase species as computed with DFT.	49
Table 4.2: Comparison between adsorption energy calculated from TPD peak temperature and DFT-rPBE functional.	50
Table 4.3: Steady state surface coverages at typical experimental condition of 573 K, 30 bar of syngas with CO:H ₂ in an 1:1 ratio.	56
Table 4.4: Comparison between computed and experimental selectivities, using experimental data from Shou et al..	57
Table 4.5: Selectivities of total hydrocarbons and total alcohols at different temperatures (on CO ₂ -free basis).	58
Table 4.6: Selectivities of total hydrocarbons and total alcohols at different pressures (on CO ₂ -free basis).	58
Table 4.7: Degrees of rate control for selected steps under reaction condition at 573 K, 30 bar of syngas with CO/H ₂ = 1:1.	62
Table 4.8: Degrees of selectivity control for selected steps under reaction condition at 573 K, 30 bar of syngas with CO/H ₂ = 1:1.	64
Table 4.A.1: Unit cell vectors for a (1×1) surface used in this chapter.	78

Table 4.A.2: Fractional coordinates for a (1×1) reconstructed bare Mo ₂ C (001) surface.	79
Table 4.A.3: Adsorption sites of syngas reaction intermediates adsorbed on reconstructed bare Mo ₂ C (001) surface.	80
Table 4.B.1: List of elementary steps with reaction enthalpy and activation energy in the reaction network used in this chapter.	97
Table 4.D.1: Steady state coverage solved from microkinetic model at 573 K, 30 bar of syngas with CO/H ₂ in an 1:1 ratio.	104
Table 5.1: DFT calculated CO adsorption energy and vibrational frequency on the reconstructed Mo ₂ C (001) surface.	116
Table 5.2: DFT calculated CO adsorption energy and vibrational frequency on the modified reconstructed Mo ₂ C (001) surface.	121
Table 5.A.1: Unit cell vectors for a (2×2) surface.	129
Table 5.A.2: Fractional coordinates for RbO adsorbed on a (2×2) reconstructed Mo ₂ C (001) surface.	130
Table 6.1: DDEC charges of RbO promoter and CO insertion reaction intermediates on Mo ₂ C (001) surface.	139
Table 6.2: DDEC charges of the transition state [CH ₃ CO] structure of the CO insertion on Mo ₂ C (001) surface.	144
Table 7.1: Structural information and DFT computed charges for Mo containing materials.	151
Table 7.2: Results from DFT computations and XANES experiments.	152
Table 7.A.1: Unit cell vectors and coordinates for bulk MoS ₂ in P63/mmc space group.	165
Table 7.A.2: Unit cell vectors and coordinates for bulk MoS ₂ in R3mH space group.	165
Table 7.A.3: Unit cell vectors and coordinates for bulk Mo ₂ C in Pbcn space group.	166
Table 7.A.4: Unit cell vectors and coordinates for bulk MoO ₂ in P121/c1 space group.	166
Table 7.A.5: Unit cell vectors and coordinates for bulk MoO ₃ in Pbnm space group.	167
Table 7.A.6: Unit cell vectors and coordinates for bulk MoO ₃ in Pbma space group.	168

Table 7.A.7: Unit cell vectors and coordinates for bulk Rb_2MoO_4 in $C12/m1$ space group.
169

LIST OF FIGURES

	Page
Figure 3.1: The most stable bulk structure of β - Mo_2C phase viewed along the [010] axis.	19
Figure 3.2: The surface free energies of seven low Miller index surfaces plotted as a function of $\mu_{\text{C}} - \mu_{\text{C}}(\text{bulk})$.	20
Figure 3.3: The predicted equilibrium crystal shapes of Mo_2C determined from the Wulff construction using the surface free energies at the lower and upper bound of $\mu_{\text{C}} - \mu_{\text{C}}(\text{bulk})$.	22
Figure 3.4: The adsorption energy of K and Rb as a function of coverage on $\text{Mo}_2\text{C}(001)$. The solid curve shows a fit of the data to the Albano model.	24
Figure 3.5: (a) Unreconstructed and (b) reconstructed bare (001) surface.	28
Figure 3.6: STM image of "honeycomb" structure on $\text{Mo}_2\text{C}(001)$ surface.	28
Figure 3.7: Top view of K adsorption on (a) unreconstructed and (b) reconstructed (001) surfaces.	29
Figure 3.A.1: The adsorption energy of K at three distinct coverages on six Mo_2C surfaces as computed with DFT. The solid curves show fits of the data to the Albano model.	35
Figure 4.1: Top view of reconstructed C-terminated Mo_2C (001) surface used in this chapter.	46
Figure 4.2: Syngas reaction network examined in this chapter. Gas phase reactants (products) are shown in circles (rectangles).	48
Figure 4.3: Schematic showing the quasi-chemical approximation.	52
Figure 4.4: Rates of elementary steps in the reaction network at steady state. Gas phase reactants (products) are shown in circles (rectangles).	60
Figure 4.5: Important selectivity determining steps within the main reaction mechanism illustrated in Figure 4.4.	65
Figure 4.6: Selectivity promoting steps for CH_4 and CO_2 at different levels of error on the slope and intercept terms in the BEP relation.	66
Figure 4.7: Selectivity promoting and inhibiting steps for ethane at different levels of error on the slope and intercept terms in the BEP relation.	68

Figure 4.8: Selectivity promoting and inhibiting steps for ethanol at different levels of error on the slope and intercept terms in the BEP relation.	68
Figure 4.A.1: Adsorption geometry of CO on Mo top sites on reconstructed bare Mo ₂ C (001) surface.	81
Figure 4.A.2: Adsorption geometry of CO on C top sites on reconstructed bare Mo ₂ C (001) surface.	81
Figure 4.A.3: Adsorption geometry of H on reconstructed bare Mo ₂ C (001) surface.	82
Figure 4.A.4: Adsorption geometry of O on reconstructed bare Mo ₂ C (001) surfaces.	82
Figure 4.A.5: Adsorption geometry of CH on reconstructed bare Mo ₂ C (001) surface.	83
Figure 4.A.6: Adsorption geometry of CH ₂ on reconstructed bare Mo ₂ C (001) surface.	83
Figure 4.A.7: Adsorption geometry of OH on reconstructed bare Mo ₂ C (001) surface.	84
Figure 4.A.8: Adsorption geometry of CH ₃ on reconstructed bare Mo ₂ C (001) surface.	84
Figure 4.A.9: Adsorption geometry of CH ₄ on reconstructed bare Mo ₂ C (001) surface.	85
Figure 4.A.10: Adsorption geometry of HCO on reconstructed bare Mo ₂ C (001) surface.	85
Figure 4.A.11: Adsorption geometry of H ₂ CO on reconstructed bare Mo ₂ C (001) surface.	86
Figure 4.A.12: Adsorption geometry of H ₃ CO on reconstructed bare Mo ₂ C (001) surface.	86
Figure 4.A.13: Adsorption geometry of CH ₃ OH on reconstructed bare Mo ₂ C (001) surface.	87
Figure 4.A.14: Adsorption geometry of H ₂ O on reconstructed bare Mo ₂ C (001) surface.	87
Figure 4.A.15: Adsorption geometry of CO ₂ on reconstructed bare Mo ₂ C (001) surface.	88
Figure 4.A.16: Adsorption geometry of COOH on reconstructed bare Mo ₂ C (001) surface.	88
Figure 4.A.17: Adsorption geometry of HCOO on reconstructed bare Mo ₂ C (001) surface.	89
Figure 4.A.18: Adsorption geometry of H ₂ COO on reconstructed bare Mo ₂ C (001) surface.	89

Figure 4.A.19: Adsorption geometry of C ₂ H on reconstructed bare Mo ₂ C (001) surface.	90
Figure 4.A.20: Adsorption geometry of CHCH on reconstructed bare Mo ₂ C (001) surface.	90
Figure 4.A.21: Adsorption geometry of CCH ₃ on reconstructed bare Mo ₂ C (001) surface.	91
Figure 4.A.22: Adsorption geometry of CH ₂ CH ₂ on reconstructed bare Mo ₂ C (001) surface.	91
Figure 4.A.23: Adsorption geometry of C ₂ H ₅ on reconstructed bare Mo ₂ C (001) surface.	92
Figure 4.A.24: Adsorption geometry of C ₂ H ₆ on reconstructed bare Mo ₂ C (001) surface.	92
Figure 4.A.25: Adsorption geometry of CH ₃ CO on reconstructed bare Mo ₂ C (001) surface.	93
Figure 4.A.26: Adsorption geometry of CH ₃ CHO on reconstructed bare Mo ₂ C (001) surface.	93
Figure 4.A.27: Adsorption geometry of CH ₃ CH ₂ O on reconstructed bare Mo ₂ C (001) surface.	94
Figure 4.A.28: Adsorption geometry of CH ₃ CH ₂ OH on reconstructed bare Mo ₂ C (001) surface.	94
Figure 4.A.29: Adsorption geometry of CH ₂ CO on reconstructed bare Mo ₂ C (001) surface.	95
Figure 4.A.30: Adsorption geometry of CHCH ₂ on reconstructed bare Mo ₂ C (001) surface.	95
Figure 4.A.31: Adsorption geometry of CHCH ₃ on reconstructed bare Mo ₂ C (001) surface.	96
Figure 4.C.1: Comparison of MF, QCA and MC for interaction energy = 0.0001 eV (repulsive) at 573 K.	100
Figure 4.C.2: Comparison of MF, QCA and MC for interaction energy = 0.05 eV (repulsive) at 573 K.	101
Figure 4.C.3: Comparison of MF, QCA and MC for interaction energy = 0.2 eV (repulsive) at 573 K.	102

Figure 4.C.4: Comparison of MF, QCA and MC for interaction energy = -0.2 eV (attractive) at 573 K.	103
Figure 5.1: Top view of reconstructed hexagonal α -Mo ₂ C (001) surface.	111
Figure 5.2: IR spectroscopy of gaseous species in CO hydrogenation at 573 K, 30 bar syngas over 5 wt.% Rb-2 wt.% Mo ₂ C/Al ₂ O ₃ .	114
Figure 5.3: Diffuse reflectance Fourier transform spectra of adsorbed CO on 2 wt.% Mo ₂ C/Al ₂ O ₃ at room temperature after being pretreated at 573 K, in 30 bar syngas (H ₂ /CO = 1) for 12 h and in 1 bar H ₂ for 1h.	115
Figure 5.4: Top and side view of CO adsorption on reconstructed hexagonal Mo ₂ C (001) surface: (a) CO-free; (b) CO adsorbed on C top sites; (c) CO adsorbed on Mo top sites.	116
Figure 5.5: Diffuse reflectance Fourier transform spectra of adsorbed CO on samples at room temperature after being pretreated at 573 K, in 30 bar syngas (H ₂ /CO = 1) for 12 h and in 1 bar H ₂ for 1h: (a) 2 wt.% Mo ₂ C/Al ₂ O ₃ ; (b) 2 wt.% Rb-2 wt.% Mo ₂ C/Al ₂ O ₃ ; (c) 5 wt.% Rb-2 wt.% Mo ₂ C/Al ₂ O ₃ ; (d) 7.5 wt.% Rb-2 wt.% Mo ₂ C/Al ₂ O ₃ ; (e) 10 wt.% Rb-2 wt.% Mo ₂ C/Al ₂ O ₃ . Spectra are offset for clarity.	119
Figure 5.6: Top and side view of CO adsorption on Rb-modified reconstructed hexagonal Mo ₂ C (001) surface: (a) no adsorbed CO; (b) CO adsorbed on C top sites; (c) CO adsorbed on Mo top sites; and CO adsorption on RbO-modified reconstructed hexagonal Mo ₂ C (001) surface: (d) no adsorbed CO; (e) CO adsorbed on C top sites; (f) CO adsorbed on Mo top sites.	121
Figure 5.7: Hypothesis of Rb promoter formation mechanism on Mo ₂ C catalyst for alcohol synthesis.	124
Figure 6.1: Top view of reconstructed hexagonal α -Mo ₂ C (001) surface.	133
Figure 6.2: Top view of RbO adsorbed on (2×2) Mo ₂ C (001) surface.	135
Figure 6.3: Top view of CO adsorbed on Mo top (left) and C top (right) on (2×2) Mo ₂ C (001) surface.	135
Figure 6.4: Top view of CH ₃ adsorbed on (2×2) Mo ₂ C (001) surface.	136
Figure 6.5: Top view of CH ₃ CO adsorbed on (2×2) Mo ₂ C (001) surface.	136
Figure 6.6: Top view of RbO co-adsorbed with CO on Mo top (left) and C top (right) sites on (2×2) Mo ₂ C (001) surface.	137
Figure 6.7: Top view of RbO co-adsorbed with CH ₃ on (2×2) Mo ₂ C (001) surface.	137

Figure 6.8: Top view of RbO co-adsorbed with CH ₃ CO on (2×2) Mo ₂ C (001) surface.	138
Figure 6.9: Schematic of RbO co-adsorbed with CO on Mo ₂ C surface.	140
Figure 6.10: Schematic of RbO co-adsorbed with CH ₃ on Mo ₂ C surface.	141
Figure 6.11: Schematic of RbO co-adsorbed with CH ₃ CO on Mo ₂ C surface.	141
Figure 6.12: Top and side view of CO co-adsorbed with CH ₃ on two adjacent C top sites on Mo ₂ C (001) surface as the initial state of CO insertion reaction route.	142
Figure 6.13: Top and side view of CH ₃ CO on C top sites on Mo ₂ C (001) surface as the final state of CO insertion reaction route.	143
Figure 6.14: Potential energy along the reaction coordinates of CO insertion on Mo ₂ C (001) surface with the top and side view of the transition state [CH ₃ CO] structure.	144
Figure 6.15: Schematic of RbO co-adsorbed with the transition state [CH ₃ CO] structure on Mo ₂ C surface.	145
Figure 7.1: XANES data for Mo-containing compounds. Data were calibrated according to a Mo foil reference with the first derivative of the first peak assigned to 20000 eV.	153
Figure 7.2: Mo K-edge energy vs. formal oxidation state for Mo-containing compounds. Fitted line has an R-squared value of 0.72155.	154
Figure 7.3: Mo K-edge energy vs. Bader charge for Mo-containing compounds. Fitted line has an R-squared value of 0.88282.	155
Figure 7.4: Mo K-edge energy vs. DDEC charge for Mo-containing compounds. The linear relation fitted by least squares regression is K-edge Energy = 20005.28 + 3.57 × Mo DDEC charges with an R-squared value of 0.97853.	157
Figure 7.5: Prediction of DDEC charges of catalyst samples from their Mo K-edge energies using the linear relation found from Fig. 7.4.	159

SUMMARY

As an important chemical raw material, alcohols can be used as fuels, solvents and chemical feedstocks to produce a variety of downstream products. With limited fossil fuel resources, alcohol synthesis from syngas reactions can be a potential alternative to the traditional petroleum based alcohol synthesis. Among many catalysts active for syngas to alcohol processes, alkali promoted Mo_2C has shown promising performance. More interestingly, the alkali promoter was found to play an important role in shifting the reaction selectivity from hydrocarbons to alcohols. However, limited understanding of the mechanism of this alkali promoter effect is available due to the complexity of syngas reaction mechanism and low content of alkali added to the catalysts.

In this thesis, we performed a comprehensive investigation of the alkali promoter effect with density functional theory (DFT) calculations as our primary tool. We first examine various Mo_2C surfaces to determine a representative surface structure active to alkali adsorption. On this particular surface, we develop a syngas reaction network including relevant reaction mechanisms proposed in previous literature. With energetics derived from DFT calculations and a BEP relation, we predict the syngas reaction selectivity and find it to be in excellent agreement with experimental results. The dominant reaction mechanism and selectivity determining steps are determined from sensitivity analysis. We also propose a formation mechanism of alkali promoters on Mo_2C catalysts that shows consistency between experimental IR and DFT computed vibrational frequencies. Finally, the effect of alkali promoters on the selectivity determining steps for syngas reactions are investigated from DFT calculations and charge

analysis. We are able to rationalize the role of alkali promoters in shifting the reaction selectivity from hydrocarbons to alcohols on Mo_2C catalysts.

CHAPTER 1

INTRODUCTION

1.1 Alcohol synthesis from syngas reactions

As an important raw material in the modern society, alcohol can be used as fuel, solvent and chemical feedstock. While the current chemical industry heavily relies on petroleum based olefins as the building blocks, alcohol could be an alternative for synthesis of chemicals since it is renewable, environmental-friendly, and can be derived from a variety of sources.¹⁻⁴ Traditionally, alcohols were either produced from hydration of olefins from oil refinery, or fermentation of biomass derived sugars. The former process is subject to the limited fossil fuel resources, while the latter is not economically feasible for producing industrial grade pure alcohols. In contrast to these processes, alcohol synthesis from syngas ($\text{CO}+\text{H}_2$) could be a promising approach.

As a versatile chemical feedstock, syngas can be either derived from conventional sources, such as coal and natural gas, or renewable sources like biomass.⁵ Extensive research has been performed to investigate producing downstream chemicals from syngas reactions.⁶ Fischer-Tropsch synthesis, aiming at converting syngas to hydrocarbons, has been successfully implemented on a commercial scale. Similarly, methanol synthesis from syngas, has been commercialized over Cu-based catalysts. However, no commercially viable process exists to date that can convert syngas to ethanol and higher alcohols.

1.2 Alkali promoted Mo₂C as a promising catalyst

Catalytic conversion from syngas to downstream products has been investigated experimentally with various homogeneous and heterogeneous catalysts.^{1,2,7,8} Among the heterogeneous catalysts, Mo₂C based catalysts exhibited promising performance due to their noble-metal-like catalytic properties, relatively low cost, and resistance to sulfur poisoning.^{9,10} Mo₂C has been reported in many catalytic applications, such as steam reforming,¹¹⁻¹³ Fischer-Tropsch synthesis,^{10,14-16} water gas shift reaction,¹⁷⁻¹⁹ and higher alcohol synthesis.²⁰⁻²² Interestingly, when an alkali promoter is added to the catalysts, the syngas reaction selectivity has been shown to shift significantly from hydrocarbons to alcohols.^{20,22-24} Woo et al. reported enhanced selectivity towards linear C₁-C₇ alcohols with addition of K₂CO₃ as a promoter.²⁰ Xiang et al. performed a series of studies on performance of Mo₂C catalysts for mixed alcohol synthesis with doped K and other transition metals, as promoters.^{21,25-28} Recently, Shou et al. investigated reactivity of Rb promoted catalysts regarding the influence of passivation and Rb promoter with several spectroscopic techniques.²²⁻²⁴ All this evidence suggested that an alkali promoter is crucial to the catalytic performance for alcohol synthesis reactions. However, limited knowledge of alkali promoter effects has been obtained experimentally to date, due to the complexity of these catalysts, where an Mo₂C phase, the alkali promoter, and the catalyst support may all be important. The elucidation of the alkali promoter effect requires additional approach that can examine catalysts at a more detailed level.

As a rapidly developing modeling technique in recent years, density functional theory (DFT) has been applied to investigate many important catalytic reactions, including ammonia synthesis, water gas shift, Fischer Tropsch synthesis, etc..²⁹⁻³² It has

shown a useful in understanding the fundamental properties of heterogeneous catalysts. Regarding Mo₂C catalysts, a number of DFT studies have been performed.³³⁻⁴⁴ Kitchin et al. examined the β-Mo₂C (001) surface along with the closed-packed surfaces of other carbides to compare properties of various carbides surfaces.³⁵ Ren et al. investigated adsorption of several small molecules on β-Mo₂C (001), including H, CO, CO₂, O₂, CH_x and C₂H₄.^{38,45} Tominaga et al. studied individual reaction steps associated with several reactions on β-Mo₂C (001) including the water gas shift reaction, CH₄ reforming, and hydrodesulfurization of thiophene.^{41,46,47} Shi et al. performed calculations on several aspects of Mo₂C catalysts, from the surface properties, adsorption of CO and NO, to dissociation of these gas molecules on Mo₂C surface.^{39,40} Pistonesi et al. studied adsorption of alkali metal on Mo₂C surfaces and its effect on CO adsorption and dissociation.⁴⁸ Medford et al. applied *ab initio* thermodynamics and DFT to study the stability of surface structure of Mo₂C and adsorption of reactive intermediates as well as C-O bond dissociation on the Mo₂C surface.³⁶ Although these studies have provided useful insights into Mo₂C catalysts, none of them have investigated alkali promoter's role in shifting reaction selectivity from hydrocarbons to alcohols for alcohol synthesis on Mo₂C catalysts. Also, few of them provided experimental validation to support their conclusions.

1.3 Thesis summary

In order to address these limitations, we seek to present a comprehensive study on the alkali promoter effect for alcohol synthesis on Mo₂C catalysts. A complete description of alkali promoted alcohol synthesis on Mo₂C catalysts will be provided, from the bulk structure of Mo₂C, the active surface structure of Mo₂C, the syngas

reaction network, alkali promoter formation and finally the mechanism of alkali promoter shifting the reaction selectivity. Further, we collaborate with an experimental group supervised by Prof. Robert Davis at University of Virginia to validate our modeling work. A summary of the contents in later chapters is given below.

In Chapter 2, we provide a simple overview of density functional theory (DFT) which will be our primary method throughout the entire thesis for predicting the physical and chemical properties of the systems we have interest in.

In Chapter 3, we examine the bulk and surface structures of Mo_2C to determine a representative surface structure for syngas reactions study in further chapters. Specifically, several low Miller index surface structures of Mo_2C were first cleaved from hexagonal phase bulk Mo_2C , and their surface free energies were calculated. The equilibrium crystal shape of Mo_2C was then predicted by minimizing the total surface free energy. Adsorption of K and Rb on these surfaces was computed, where Mo_2C (001) was found to bind K and Rb most strongly. This surface was also shown to favor a reconstruction in the absence of adsorbates. Therefore, the reconstructed Mo_2C (001) was determined as a representative surface structure.

In Chapter 4, a surface reaction network analysis was performed on the reconstructed Mo_2C (001) surface, with the objective of identifying the elementary steps that contribute most to the reaction selectivity shift from hydrocarbons to alcohols upon promotion with alkali. Adsorption of 32 reaction intermediates was examined, followed by computation of the reaction energy of 53 elementary steps using DFT, with activation energies approximated by a BEP relation. From kinetic theory and transition state theory, a microkinetic model was constructed, and the steady state reaction selectivities of

products were computed and found to be in excellent agreement with experimental results. Finally, the contribution of each elementary step to the reaction selectivity was quantitatively measured by sensitivity analysis. CO insertion ($\text{CO}^* + \text{CH}_3^*$) was suggested to be responsible for the selectivity of hydrocarbons over alcohols.

In Chapter 5, we investigate alkali promoter formation and its effect on CO adsorption by DFT calculations and IR spectroscopy to elucidate how alkali promoters are formed on Mo_2C catalysts. Experimentally, the IR peak associated with CO adsorption was found to undergo a red shift upon Rb promoter addition. This IR peak shift was well explained by computed CO vibrational frequency changes with RbO coadsorbed. An alkali promoter formation mechanism was proposed, where surface hydroxyl groups generated in catalyst preparation were replaced by Rb_2CO_3 to form RbO species on the surface.

In Chapter 6, with RbO as the active form of alkali promoter and CO insertion ($\text{CO}^* + \text{CH}_3^*$) as the elementary step contribute most to the selectivity shift from hydrocarbons to alcohols proposed in previous chapters, we look into how CO insertion take place on Mo_2C surface at a more detailed level, and how RbO can affect the activation energy of this step. A complete charge analysis on CO^* , CH_3^* , CH_3CO^* and RbO was performed by the Density Derived Electrostatic and Chemical (DDEC) charge assignment method, where it was shown that distinct surface dipoles were created by electron transfer between the Mo_2C surface and adsorbed intermediates. The transition state of CO insertion was further located by Nudged Elastic Band (NEB) calculations. Finally, the dipole interaction between RbO and transition state $[\text{CO}-\text{CH}_3]$ structure was

found to favor the CO insertion mechanism, explaining the alkali promoter's role in shift reaction selectivity from hydrocarbons to alcohols.

Besides the main topic of the thesis described from Chapter 3 to Chapter 6, we establish a linear correlation between experimental X-ray Absorption Near Edge Structure (XANES) energy and computed DDEC charge for several Mo-containing materials. This effort was originally motivated by an experimental observation where MoS₂ gave significant lower XANES edge energy than MoO₂, although Mo in both materials have the formal oxidation state of +4. By comparing three different charge assignment methods: the formal oxidation state, the Bader charge and the DDEC charge for several Mo containing materials, we show that only DDEC charge can accurately represent partial charge of Mo in layered materials like MoS₂. A linear relation was established between XANES edge energy and the DDEC charge that can be used to provide a simple "snapshot" of oxidation state of Mo in supported catalyst samples.

Finally, we conclude the major results in this thesis and outline challenges and opportunities for future work of this topic in Chapter 8.

1.4 References

- (1) Spivey, J. J.; Egbebi, A. *Chem. Soc. Rev.* **2007**, *36*, 1514.
- (2) Subramani, V.; Gangwal, S. K. *Energy Fuels* **2008**, *22*, 814.
- (3) Surisetty, V. R.; Dalai, A. K.; Kozinski, J. *Appl. Catal. A-Gen.* **2011**, *404*, 1.
- (4) Zaman, S.; Smith, K. J. *Catal. Rev.-Sci. Eng.* **2012**, *54*, 41.
- (5) Huber, G. W.; Iborra, S.; Corma, A. *Chemical Reviews* **2006**, *106*, 4044.
- (6) Rostrup-Nielsen, J. R.; Nielsen, R. *Catal. Rev.-Sci. Eng.* **2004**, *46*, 247.
- (7) Gupta, M.; Smith, M. L.; Spivey, J. J. *Acs Catalysis* **2011**, *1*, 641.
- (8) Xiang, Y. Z.; Chitry, V.; Liddicoat, P.; Felfer, P.; Cairney, J.; Ringer, S.; Kruse, N. *J. Am. Chem. Soc.* **2013**, *135*, 7114.
- (9) Kojima, R.; Aika, K. *Appl. Catal. A-Gen.* **2001**, *219*, 141.
- (10) Oyama, S. T. *Catalysis Today* **1992**, *15*, 179.
- (11) Oshikawa, K.; Nagai, M.; Omi, S. *J. Phys. Chem. B* **2001**, *105*, 9124.
- (12) Claridge, J. B.; York, A. P. E.; Brungs, A. J.; Marquez-Alvarez, C.; Sloan, J.; Tsang, S. C.; Green, M. L. H. *Journal of Catalysis* **1998**, *180*, 85.
- (13) Barthos, R.; Solymosi, F. *Journal of Catalysis* **2007**, *249*, 289.
- (14) Kojima, I.; Miyazaki, E.; Yasumori, I. *J. Chem. Soc.-Chem. Commun.* **1980**, 573.
- (15) Park, K. Y.; Seo, W. K.; Lee, J. S. *Catalysis Letters* **1991**, *11*, 349.
- (16) Griboval-Constant, A.; Giraudon, J. M.; Leclercq, G.; Leclercq, L. *Appl. Catal. A-Gen.* **2004**, *260*, 35.
- (17) Moon, D. J.; Ryu, J. W. *Catalysis Letters* **2004**, *92*, 17.
- (18) Patt, J.; Moon, D. J.; Phillips, C.; Thompson, L. *Catalysis Letters* **2000**, *65*, 193.
- (19) Nagai, M.; Matsuda, K. *Journal of Catalysis* **2006**, *238*, 489.
- (20) Woo, H. C.; Park, K. Y.; Kim, Y. G.; Nam, I. S.; Chung, J. S.; Lee, J. S. *Applied Catalysis* **1991**, *75*, 267.

- (21) Xiang, M. L.; Li, D. B.; Li, W. H.; Zhong, B.; Sun, Y. H. *Fuel* **2006**, *85*, 2662.
- (22) Shou, H.; Davis, R. J. *Journal of Catalysis* **2011**, *282*, 83.
- (23) Shou, H.; Ferrari, D.; Barton, D. G.; Jones, C. W.; Davis, R. J. *ACS Catalysis* **2012**, *2*, 1408.
- (24) Shou, H.; Li, L.; Ferrari, D.; Sholl, D. S.; Davis, R. J. *Journal of Catalysis* **2013**, *299*, 150.
- (25) Xiang, M. L.; Li, D. B.; Li, W. H.; Zhong, B.; Sun, Y. H. *Catalysis Communications* **2007**, *8*, 503.
- (26) Xiang, M. L.; Li, D. B.; Li, W. H.; Zhong, B.; Sun, Y. H. *Catalysis Communications* **2007**, *8*, 513.
- (27) Xiang, M. L.; Li, D. B.; Xiao, H. C.; Zhang, J. L.; Li, W. H.; Zhong, B.; Sun, Y. H. *Catalysis Today* **2008**, *131*, 489.
- (28) Xiang, M. L.; Li, D. B.; Zou, J.; Li, W. H.; Sun, Y. H.; She, X. C. *Journal of Natural Gas Chemistry* **2010**, *19*, 151.
- (29) Honkala, K.; Hellman, A.; Remediakis, I. N.; Logadottir, A.; Carlsson, A.; Dahl, S.; Christensen, C. H.; Norskov, J. K. *Science* **2005**, *307*, 555.
- (30) Norskov, J. K.; Abild-Pedersen, F.; Studt, F.; Bligaard, T. *Proceedings of the National Academy of Sciences of the United States of America* **2011**, *108*, 937.
- (31) Norskov, J. K.; Bligaard, T.; Hvolbaek, B.; Abild-Pedersen, F.; Chorkendorff, I.; Christensen, C. H. *Chem. Soc. Rev.* **2008**, *37*, 2163.
- (32) Norskov, J. K.; Bligaard, T.; Rossmeisl, J.; Christensen, C. H. *Nat. Chem.* **2009**, *1*, 37.
- (33) Han, J. W.; Li, L.; Sholl, D. S. *The Journal of Physical Chemistry C* **2011**, *115*, 6870.
- (34) Hugosson, H. W.; Eriksson, O.; Nordstrom, L.; Jansson, U.; Fast, L.; Delin, A.; Wills, J. M.; Johansson, B. *Journal of Applied Physics* **1999**, *86*, 3758.
- (35) Kitchin, J. R.; Norskov, J. K.; Barteau, M. A.; Chen, J. G. G. *Catalysis Today* **2005**, *105*, 66.
- (36) Medford, A. J.; Vojvodic, A.; Studt, F.; Abild-Pedersen, F.; Norskov, J. K. *Journal of Catalysis* **2012**, *290*, 108.

- (37) Pistonesi, C.; Juan, A.; Farkas, A. P.; Solymosi, F. *Surface Science* **2008**, *602*, 2206.
- (38) Ren, J.; Huo, C. F.; Wang, J. G.; Li, Y. W.; Jiao, H. J. *Surface Science* **2005**, *596*, 212.
- (39) Shi, X. R.; Wang, S. G.; Wang, H.; Deng, C. M.; Qin, Z. F.; Wang, J. G. *Surface Science* **2009**, *603*, 852.
- (40) Shi, X.-R.; Wang, J.; Hermann, K. *The Journal of Physical Chemistry C* **2010**, *114*, 13630.
- (41) Tominaga, H.; Nagai, M. *J. Phys. Chem. B* **2005**, *109*, 20415.
- (42) Tominaga, H.; Nagai, M. *Appl. Catal. A-Gen.* **2005**, *282*, 5.
- (43) Vojvodic, A. *Catalysis Letters* **2012**, *142*, 728.
- (44) Wang, T.; Liu, X. W.; Wang, S. G.; Huo, C. F.; Li, Y. W.; Wang, J. G.; Jiao, H. J. *Journal of Physical Chemistry C* **2011**, *115*, 22360.
- (45) Ren, J.; Huo, C. F.; Wang, J. G.; Cao, Z.; Li, Y. W.; Jiao, H. J. *Surface Science* **2006**, *600*, 2329.
- (46) Tominaga, H.; Nagai, M. *Applied Catalysis A: General* **2007**, *328*, 35.
- (47) Tominaga, H.; Nagai, M. *Appl. Catal. A-Gen.* **2008**, *343*, 95.
- (48) Pistonesi, C.; Juan, A.; Farkas, A. P.; Solymosi, F. *Surface Science* **2010**, *604*, 914.

CHAPTER 2

COMPUTATIONAL METHODS

Density functional theory (DFT) is one of the most widely used computational methods to investigate the electronic structure of many-body systems such as atoms, molecules, and condensed phases. In this chapter, we present a brief overview of DFT, which will be our primary method to study the topics discussed in this thesis. A detailed introduction of DFT is beyond the scope of this chapter, as excellent review articles and books are readily available.¹⁻⁹

In 1926, the Austrian physicist Erwin Schrodinger first published his famous work describing quantum state of physical systems - the Schrodinger equation. However, exact analytic solution to the equation only exists for very simple systems such as a single hydrogen atom since the dimension of the problem grow rapidly when multiple electrons are involved. With the advance of modern computing ability, growing attention was focused on developing numerical methods to solve the Schrodinger equation.

The idea of DFT are based on two fundamental mathematical theorems proved by Hohenberg and Kohn.¹⁰ They first showed that the ground state total energy of a system of interacting electrons is a unique functional of the electron density. The Hohenberg-Kohn theorem states that there exists a unique mapping between the ground state electron density and the ground state wave function of the system. They further identified that the electron density that minimizes the energy of the overall functional is the true electron density corresponding to the full solution of the Schrodinger equation. In 1965, Kohn and Sham showed that the problem of multiple interacting electrons can be

mapped to a set of non-interacting electrons in an effective external potential, leading to a set of self-consistent, single particle equations known as the Kohn-Sham equations:¹¹

$$\left[-\frac{\hbar^2}{2m}\nabla^2 + V(\vec{r}) + V_H(\vec{r}) + V_{xc}(\vec{r})\right]\Psi_i(\vec{r}) = \varepsilon_i\Psi_i(\vec{r}) \quad (2.1)$$

In this equation, the energy of a system is decomposed into four principal components: the kinetic energy, the nuclei-electron static interaction, the electron-electron static interaction, and the non-classical electron-electron interactions. While the first three components can be well represented in their exact forms, the form of the non-classical interactions is not known. To address these non-classical effects, a concept named as exchange correlation energy functional was created. This functional can be approximated by various theoretical methods. Typically, DFT calculations for solid materials employed two types of approximations: the local density approximation (LDA) and the generalized gradient approximation (GGA) to describe the exchange correlation energy functional. The LDA assumes that the energy of each electron can be related to the energy of that electron in a uniform electron gas with the same global density as the local electron density in the actual system. The GGA includes corrections for local gradients in the electron density and is often implemented as an improvement of the LDA.

Throughout the thesis, we have employed plane wave DFT calculations using the Vienna *ab initio* Simulation Package (VASP).¹²⁻¹⁴ The projector augmented wave (PAW) method^{15,16} was used to describe ionic cores in these calculations. The revised Perdew-Burke-Ernzerhof (rPBE) functional^{17,18} was applied to describe the exchange correlation contributions to the total energy. Compared with other frequently used functionals such as PBE and PW91, rPBE functional has shown improved accuracy for calculating adsorption energy on solid material surfaces.¹⁹ All of our calculations have

used plane wave basis functions using periodic boundary conditions to model the bulk and surface structures of the materials of interest. More details for DFT calculations on each topic are presented in the corresponding chapter.

References

- (1) Hammer, B.; Norskov, J. K. In *Advances in Catalysis, Vol 45* 2000; Vol. 45, p 71.
- (2) Greeley, J.; Norskov, J. K.; Mavrikakis, M. *Annual Review of Physical Chemistry* **2002**, *53*, 319.
- (3) Sholl, D. S.; Steckel, J. A. *Density functional theory: a practical introduction*; John Wiley & Sons, Inc., 2009.
- (4) Payne, M. C.; Teter, M. P.; Allan, D. C.; Arias, T. A.; Joannopoulos, J. D. *Reviews of Modern Physics* **1992**, *64*, 1045.
- (5) Parr, R. G., Weitao, Y. *Density-Functional Theory of Atoms and Molecules*; Oxford University Press: Oxford, 1994.
- (6) Koch, W., Holthausen, M. C. *A Chemist's Guide to Density Functional Theory*; Wiley-VCH: Berlin, 2001.
- (7) Martin, R. M. *Electronic Structure: Basic Theory and Practical Methods*; Cambridge University Press: Cambridge, 2004.
- (8) Seminario, J. M., Politzer, P. P. *Modern Density Functional Theory - A Tool for Chemistry, Theoretical and Computational Chemistry*; Elsevier: Amsterdam, 1995.
- (9) Fiolhais, C., Noguera, F., Marques, M. A. L. *A Primer in Density-Functional Theory*; Springer-Verlag: Berlin, 2003.
- (10) Hohenberg, P.; Kohn, W. *Physical Review B* **1964**, *136*, B864.
- (11) Kohn, W.; Sham, L. J. *Physical Review* **1965**, *140*, 1133.
- (12) Kresse, G.; Furthmuller, J. *Physical Review B* **1996**, *54*, 11169.
- (13) Kresse, G.; Hafner, J. *Physical Review B* **1993**, *48*, 13115.
- (14) Kresse, G.; Hafner, J. *Journal of Physics-Condensed Matter* **1994**, *6*, 8245.
- (15) Blochl, P. E. *Physical Review B* **1994**, *50*, 17953.
- (16) Kresse, G.; Joubert, D. *Physical Review B* **1999**, *59*, 1758.
- (17) Perdew, J. P.; Burke, K.; Ernzerhof, M. *Physical Review Letters* **1996**, *77*, 3865.
- (18) Perdew, J. P.; Burke, K.; Ernzerhof, M. *Physical Review Letters* **1997**, *78*, 1396.

- (19) Hammer, B.; Hansen, L. B.; Norskov, J. K. *Physical Review B* **1999**, *59*, 7413.

CHAPTER 3

DETERMINATION OF REPRESENTATIVE SURFACE STRUCTURE OF Mo_2C FOR ALCOHOL SYNTHESIS REACTIONS

3.1 Introduction

Transition metal carbides are interesting as catalysts because of their extreme hardness,¹ high melting points,² and excellent electric and thermal conductivities.³ Within this class of materials, molybdenum carbides have exhibited excellent catalytic behavior in reactions including ammonia synthesis,⁴ water-gas shift,⁵ hydrogenation of CO ^{6,7} or benzene,^{8,9} hydrodenitrogenation,¹⁰ hydrodesulfurization,¹¹ and hydrocarbon isomerization.¹² Molybdenum carbides are potentially promising substitutes for expensive noble metals due to their similar catalytic properties,¹³ accompanied by resistance to sulfur poisoning.^{13,14}

In the Mo-C phase diagram at least six different phases have been identified,¹⁵ including two phases of Mo_2C (one orthorhombic and one hexagonal). Among these phases, only two types of Mo_2C and one MoC phase are found to be stable at room temperature.^{15,16} There is some confusion in the literature regarding the names of Mo_2C phases, with some authors referring to orthorhombic Mo_2C as $\alpha\text{-Mo}_2\text{C}$.¹⁷⁻²¹ We prefer to follow the convention defined by the Joint Committee on Powder Diffraction Standards (JCPDS) data files,²²⁻²⁴ in which hexagonal Mo_2C , orthorhombic Mo_2C , and hexagonal MoC are denoted α , β , and γ , respectively. $\beta\text{-Mo}_2\text{C}$ has been studied extensively since it has a well-determined structure in which carbon atoms occupy half of the octahedral sites

in an ordered way. In α - Mo_2C , Mo atoms form a hexagonally close packed structure while carbon atoms fill half of the octahedral interstitial sites randomly. In order to study the structure of α - Mo_2C , various carbon occupancy structures were proposed and investigated in literature,^{25,26} and the eclipsed configuration identified by Haines et al.²⁶ was found to be most stable. We restrict our attention in this work to this eclipsed hexagonal configuration.

The surface properties of catalytic materials can be modified by doping with alkali metals.²⁷⁻³³ Since K is relatively inexpensive, it is widely used as a promoter in industrial applications. Woo et al. reported significant changes in the selectivity to C_1 - C_7 linear alcohols relative to hydrocarbons from synthesis gas for experiments in which molybdenum carbides were promoted with K_2CO_3 .¹⁴ Xiang et al. have reported in experiments for mixed alcohol synthesis from CO hydrogenation that both β - Mo_2C and α - MoC_{1-x} produced light hydrocarbons and by adding K as a promoter, they showed a distinctive selectivity shift from hydrocarbons to alcohols.²⁹ In general terms, this promotion effect is thought to be associated with the charge transfer to the catalyst surface due to the exceptionally low ionization potential of alkali metal. The addition of alkali promoters generates electrostatic fields at the surface, inducing substantial changes in the process of adsorption and catalytic reactions.³²

Theoretical studies have been applied to a range of physical, chemical, and electronic properties of the molybdenum carbides, including the adsorption and reaction of small species on the surfaces. Hugosson et al. have extensively examined the relative stabilities of Mo-C phases and the effect of vacancies on phase stability.¹⁵ Kitchin et al. investigated the β - Mo_2C (001) [β - Mo_2C (0001) in their notation] surface along with the

close-packed surfaces of other carbides to compare the chemical properties of various carbide surfaces.³⁴ DFT calculations for the adsorption of small molecules on β -Mo₂C (001) have been also performed, including the adsorption O₂ and CO³⁵ [α -Mo₂C (0001) in their notation], CO₂, H, CH_x (x=0-3), C₂H₄^{20,35} [α -Mo₂C (0001) in their notation], and methanol.³⁶ Tominaga et al. have studied individual reaction steps associated with several reactions on β -Mo₂C (001) including the water-gas shift reaction,³⁷ CH₄ reforming,³⁸ and hydrodesulfurization of thiophene.³⁹ In all of these studies, it appears that attention was given to the (001) surface because this is most densely packed surface of β -Mo₂C. Shi et al. reported DFT calculations for a range of low-index surfaces of α -Mo₂C [β -Mo₂C in their notation]²⁵ and further investigated CO and NO adsorption and dissociation on the α -Mo₂C (001) surface.⁴⁰ They observed that the mixed Mo/C termination of the (011) surface, not (001), had the lowest surface free energy among the surfaces they considered. Pistonesi et al. recently studied K promoter effects on dissociation of methanol on the β -Mo₂C (001) surface.⁴¹ None of the existing DFT studies of α -Mo₂C have considered the properties of alkali atom as a promoter on the surface. A small number of DFT calculations are available examining this issue on other materials.^{42,43}

In this chapter, we use DFT calculations to study the bulk and surfaces of α -Mo₂C to determine a representative surface structure reactive for alkali-promoted alcohol synthesis reactions. To make progress towards this goal, we assume that the catalytic activity of Mo₂C is associated with the terraces of stable surfaces of the material rather than being dominated by a rate-determining step dictated by a step edge or other defect. This assumption also underlies the DFT studies listed above, although it is rarely stated explicitly. Further, we believe that on the representative surface, alkali promoter

must adsorb and interact with reaction intermediates. This choice implies that we must determine what Mo_2C surfaces on a typical catalyst particle bind alkali most strongly. To this end, we examine the adsorption energies and geometries of K and Rb on seven low-index surfaces to determine the most preferred surface for alkali atom adsorption. A surprising finding from our calculations is that the bulk-terminated surface that binds K and Rb most strongly undergoes a surface reconstruction in the absence of any adsorbed species. The reconstructed surface binds K and Rb even more strongly than the bulk-terminated surface. We conclude that this reconstructed $\alpha\text{-Mo}_2\text{C}$ (001) surface is a representative surface structure for further surface reactivity investigation.

3.2 Computational methods

Our plane wave DFT calculations were performed with the Vienna *ab initio* simulation package (VASP).⁴⁴⁻⁴⁷ We employed the revised Perdew-Burke-Ernzerhof (rPBE) generalized gradient functional^{48,49} along with the projector augmented wave (PAW)^{50,51} method to describe ionic cores. A plane wave expansion with a cutoff of 400 eV was used for all calculations. Geometries were relaxed using a conjugate gradient algorithm until the forces on all unconstrained atoms were less than 0.03 eV/Å.

Calculations for adsorbed K and Rb on each surface were performed at various coverages to understand coverage effects as discussed later. A $6\times 6\times 1$ Monkhorst-Pack k-point mesh was used for a (1×1) surface unit cell, which was sufficient to give well converged results. For calculations at lower coverages, the number of k-points in the Monkhorst-Pack mesh was appropriately reduced. Calculations for H and CO adsorption with or without coadsorbed K were performed using a (2×2) surface unit cell with a $3\times 3\times 1$ Monkhorst-Pack k-point mesh. Geometries and energies for gas phase species

were calculated using supercells equivalent to those for the largest slab calculations. When examining adsorption, molecules were placed on only one side of the slab. Dipole corrections were therefore applied in computing all of the energies reported below.^{52,53}

3.3 Results and Discussion

3.3.1 Bulk structure of Mo₂C

The α -Mo₂C phase has an hexagonal crystal structure, with $a = 3.011 \text{ \AA}$, $b = 3.011 \text{ \AA}$, and $c = 4.771 \text{ \AA}$.⁵⁴ The DFT-optimized hexagonal lattice constants for α -Mo₂C phase ($a = 6.08 \text{ \AA}$, $b = 6.07 \text{ \AA}$, and $c = 4.72 \text{ \AA}$) are in good agreement with the experimental values (here we have to double a and b because the original unit cell from experiment needs to be extended to define the eclipsed configuration unit cell). This bulk structure is illustrated in Fig. 3.1. Calculations with the bulk structure confirmed that this material is metallic.

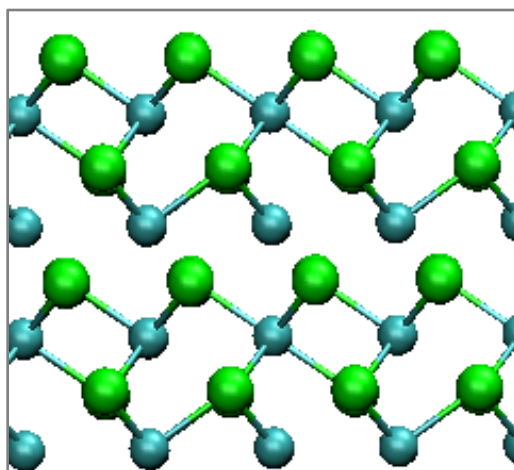


Figure 3.1: The most stable bulk structure of β -Mo₂C phase viewed along the [010] axis. Mo (C) atoms are shown as green (blue) spheres.

3.3.2 Surface structure and particle shape of Mo₂C

We cleaved this structure along seven low Miller index planes, namely (001), (010), (100), (110), (101), and (111), to construct surfaces. Each surface was represented by slabs 10-15 Å thick. All possible bulk terminations perpendicular to the surface normal to these planes were considered. The (001), (010), and (111) surfaces have both pure Mo and pure C terminations. The (100), (110), and (101) surfaces have mixed Mo/C terminations. The (011) surface has a pure Mo termination and a mixed Mo/C termination. In all calculations, no atoms in the slab were constrained and a vacuum spacing of 14 Å was used normal to the surface.

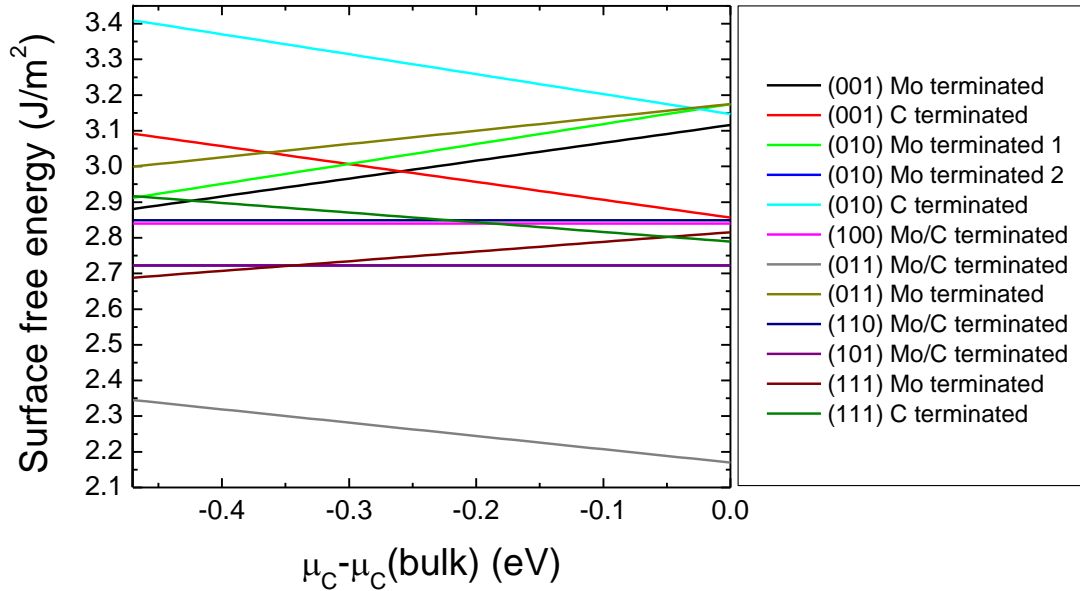


Figure 3.2: The surface free energies of seven low Miller index surfaces plotted as a function of $\mu_C - \mu_{C(\text{bulk})}$. For each surface, the results for all possible terminations are shown.

In all of our calculations the surfaces were constructed as symmetric slabs. This implies that some of the surface slabs were non-stoichiometric. As a result, the surface energy, σ , is calculated by^{25,55-58}

$$\sigma = (E_{\text{slab}} - n_{\text{Mo}}\mu_{\text{Mo}} - n_{\text{C}}\mu_{\text{C}}) / 2A. \quad (3.1)$$

Here, E_{slab} is the total energy of the slab, A is the surface area of one side of the slab, μ_x is the chemical potential of species x , and n_y is the number of atoms of species y in the supercell. After some algebra using the relationships described by previous reports,^{25,55-58} the surface energy can be expressed as a function of difference between the chemical potential for a C atom, μ_{C} , and the chemical potential in bulk phase of C, $\mu_{\text{C}}(\text{bulk})$. If a surface is stoichiometric within the symmetric slabs, Eq. (3.1) can be reduced to the usual expression for the surface energy,⁴⁷

$$\sigma = (E_{\text{slab}} - nE_{\text{bulk}}) / 2A, \quad (3.2)$$

where E_{bulk} is the bulk total energy per Mo_2C unit and n is the number of Mo_2C units in the slab. In earlier work, Shi et al. compared the surface energies of different terminations using Eq. (3.2), and then used the predictions from these calculations to compare the surface energies of a variety of low index surfaces.²⁵ This approach is potentially problematic because differing surface terminations should be compared using Eq. (3.1). In our work, we calculated the surface energy for each surface with each possible terminations using Eq. (3.1), as shown in Fig. 3.2. In Fig. 3.2, the C-terminated (010) surface has the highest surface free energy at almost all the ranges of $\mu_{\text{C}} - \mu_{\text{C}}(\text{bulk})$. Details regarding the definition and interpretation of $\mu_{\text{C}} - \mu_{\text{C}}(\text{bulk})$ are given in the earlier work by

Shi et al. The lowest surface free energy is the mixed Mo/C-terminated (011) surface, in agreement with Shi et al.'s calculations.²⁵

As can be seen from Fig. 3.2, the range of surface energies among the set of surfaces we examined is not large, with energies varying from 2.2-3.4 J/m². Once the surface energies are known, the equilibrium crystal shape (ECS) of the material can be predicted from the Wulff construction.⁵⁹⁻⁶² We used this approach to examine the ECS for a range of carbon chemical potentials. Figure 3.3 shows that resulting ECS at the upper and lower bounds for μ_C . Intermediate values of the μ_C give similar results. One immediate observation from this figure is that the (001) surface, which has been the focus of much earlier theoretical work, is not the only dominant surface on Mo₂C crystals in terms of the surface area associated with this surface.

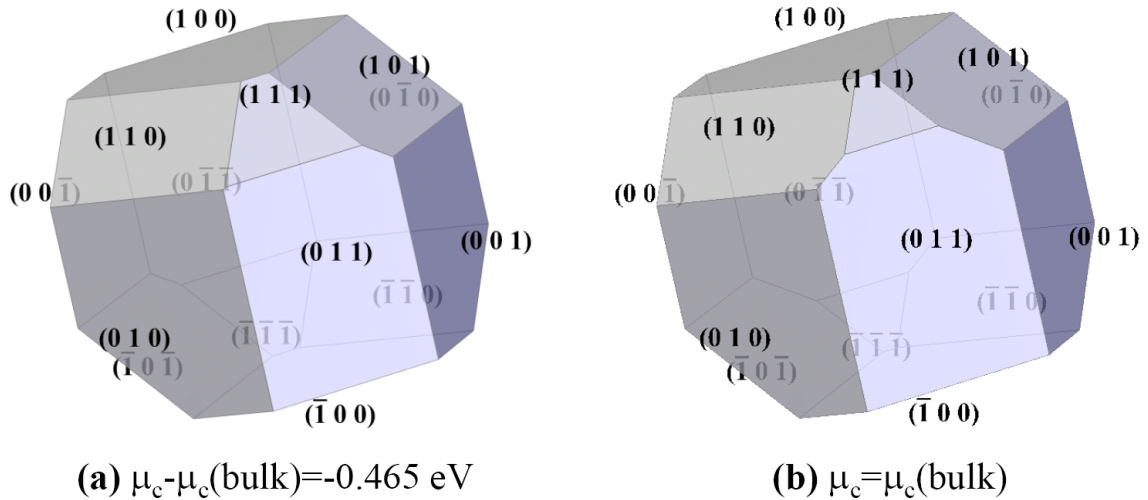


Figure 3.3: The predicted equilibrium crystal shapes of Mo₂C determined from the Wulff construction using the surface free energies at the lower and upper bound of $\mu_C - \mu_C(\text{bulk})$.

3.3.3 K and Rb adsorption on Mo₂C surfaces

As described in the Introduction, we are interested in alkali adsorption in the limit of low alkali coverages on a catalyst particle. We have therefore examined K adsorption on the seven low Miller index surfaces mentioned in section 3.3.2. For these calculations only the termination with the lowest surface energy among the terminations we examined on each surface was considered except for the (001) surface, for which we considered both Mo- and C-terminated surfaces since they had similar surface free energy. The adsorption energy, E_{ads} , of an atom or molecule was defined by

$$E_{\text{ads}} = (E_{\text{surf}} + E_{\text{adsorbate}}) - E_{\text{total}} \quad (3.3)$$

where E_{total} is the total energy of the system containing the adsorbed species, E_{surf} is the total energy for the optimized bare surface, and $E_{\text{adsorbate}}$ is the total energy for the adsorbate in the gas phase. With this definition, positive adsorption energies correspond to energetically favored states.

Figure 3.4 shows an example of the calculated K adsorption energy at six surface coverages on α -Mo₂C(001). Coverage is expressed in terms of the adsorbate number density in \AA^{-2} . In order to have confidence that a global minimum can be identified, large numbers of adsorption configurations must be examined for studying atomic or molecular adsorption.⁶³⁻⁶⁶ To address this challenge, we examined a variety of initial configurations by dividing a (1×1) surface unit cell of the (001) surface into a 4×3 grid at intervals of ~1.6 \AA . K is then positioned 3.3 \AA above each grid point so that we have 12 initial configurations for adsorption on the surface. Each configuration was relaxed to find a local energy minimum for the adsorbed molecule. The structure with the most stable adsorption energy among the energy minima found in this way was used to perform

lower coverage calculations. The adsorption energies shown in Fig. 3.4 are the result of these coverage dependent calculations.

Figure 3.4 shows that the adsorption energy of K is strongly dependent upon coverage. This is not surprising, as strong repulsive interactions induced by the dipole moment of adsorbed K are expected. Based on the steep work function changes upon the K adsorption, Bugyi et al. suggested that the K promoter donates charge to the surface upon adsorption on this kind of surface.^{30,31} Our charge calculations by Bader analysis⁶⁷⁻⁶⁹ at the highest coverage, $32.0 \text{ \AA}^2/\text{atom}$, support the observation, showing that a charge of $-0.9 e$ is transferred into the surface from K. This charge transfer creates a dipole moment associated with an adsorbed K.

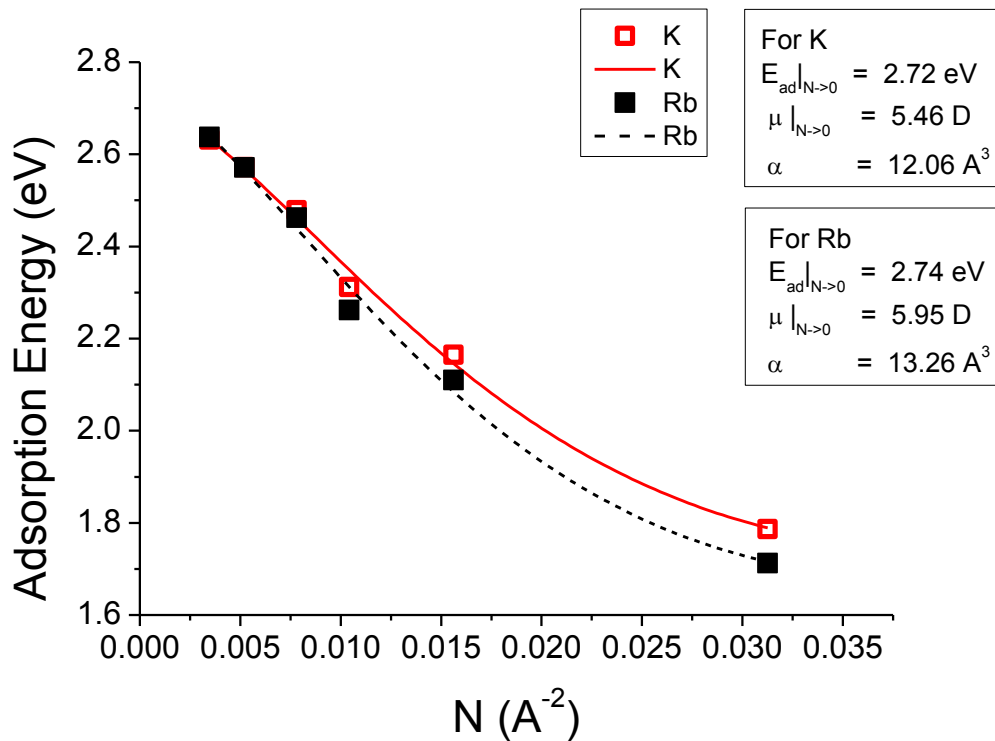


Figure 3.4: The adsorption energy of K and Rb as a function of coverage on $\text{Mo}_2\text{C}(001)$. The solid curve shows a fit of the data to the Albano model.⁷⁰

We can model the coverage dependent adsorption using a simple electrostatic method developed by Albano.⁷⁰ The coverage dependent adsorption energy is assumed to be entirely due to repulsive dipole-dipole interactions on the surface. This model has been successfully applied to several experiments including desorption of K from metal surfaces,⁷⁰ desorption of K in the presence of coadsorbed O,⁷⁰ molecular desorption of CH₃Cl from Pd(100),⁷¹ and atomic I desorption from Ni surfaces.⁷² The Albano model can be written as

$$E_{\text{ad}} = E_{\text{ad}}|_{N \rightarrow 0} - 1.602 \times \frac{9 \times (\mu|_{N \rightarrow 0})^2 \times N^{3/2}}{(1 + 9 \times \alpha \times N^{3/2})^2}. \quad (3.4)$$

Here, E_{ad} is the adsorption energy (in eV), $E_{\text{ad}}|_{N \rightarrow 0}$ is the adsorption energy in the limit of zero coverage (in eV), $\mu|_{N \rightarrow 0}$ is the static dipole moment of the K-Mo₂C surface bond in the limit of zero coverage (in Debye), N is the surface coverage in atoms (in Å⁻²), α is the constant polarizability of the adsorbed K (in Å³), 9 is the geometric factor applicable to a hexagonal or square array of adsorbates, and 1.602 is the unit conversion factor. Fitting Eq. (3.4) to the data in Fig. 3.4 gives $E_{\text{ad}}|_{N \rightarrow 0}$, $\mu|_{N \rightarrow 0}$, and α values of 2.72 eV, 5.46 D, and 12.06 Å³, respectively.

We used an approach similar to the one described above to calculate the coverage dependent adsorption energies of K for the other surfaces. For simplicity, we assumed that the polarizability of adsorbed K is independent of the surface orientation and equal to the value deduced above, 12.06 Å³. With this assumption the Albano model includes only two parameters, which we fitted for each surface from computed adsorption energies at three distinct coverages. Table 3.1 summarizes $E_{\text{ad}}|_{N \rightarrow 0}$ and $\mu|_{N \rightarrow 0}$ for each surface. For

(001) surface, results are only shown for the C-terminated surface; K had much less favorable adsorption energies on the Mo-terminated surface. Among the seven surfaces, (001) has the highest adsorption energy and dipole moment. On this basis, we selected the (001) surface for further calculations involving adsorption of intermediates of alcohol synthesis reactions.

Table 3.1: The adsorption energies and dipole moments of K in the limit of zero coverage for the seven surfaces obtained as described in the text.

Surface	C-term (001)	Mo-term (001)	(100)	(110)	(010)	(011)	(101)	(111)
$E_{\text{ad}} _{N \rightarrow 0}$ (eV)	2.72	2.00	2.21	1.84	1.70	2.31	1.96	2.70
$\mu _{N \rightarrow 0}$ (D)	5.46	3.41	3.83	3.29	1.95	4.41	2.95	4.26

To examine whether the results for K also apply to other alkali metals, we also studied Rb adsorption on Mo₂C (001) surface as a comparison with K adsorption. Calculations were performed at the same set of coverages as for K, and the Albano model was again used to fit the data. The results are shown in Fig. 3.4. The geometry, adsorption energy, and dipole moment (as determined from the Albano model) are very similar for Rb and K.

3.3.4 Surface reconstruction of Mo₂C (001) surface

We noted above that most previous DFT calculations examining surfaces of α -Mo₂C used the (001) surface, even though later calculations by Shi et al.²⁵ showed that the (011) surface has a markedly lower surface energy. Our analysis of K and Rb binding energies, however, suggests that it is quite appropriate to focus attention on the (001) surface if we are interested in low coverages of alkali on catalyst particles. While

performing calculations with α -Mo₂C(001), however, we made the surprising observation that this surface can reconstruct, even in the absence of adsorbates. Figure 3.5 shows both unreconstructed and reconstructed bare (001) surfaces. The surface energy is lowered by 0.18 J/m² for any value of $\mu_c - \mu_c(\text{bulk})$ by this reconstruction. This structure was initially observed in calculations involving CO adsorption, but subsequent calculations confirmed that the reconstructed bare surface in the absence of CO has 1.47 eV/unit cell lower total energy than the unreconstructed one. During the reconstruction, C atoms move in a way that they form hexagons on the surface with adjacent C atoms separated ~ 3.5 Å. Our reconstructed surface is similar to a honeycomb ($\sqrt{3} \times \sqrt{3}$)R30° C-terminated structure on α -Mo₂C(001) previously reported by scanning tunneling microscopy (STM),^{73,74} as shown in Fig. 3.6. This observation implies that earlier calculations^{20,35-39} examining adsorption on α -Mo₂C(001) may not capture all features of these systems because they did not include the surface reconstruction. The existence of a reconstruction for the (001) surface prompted us to consider whether surface reconstructions might also exist for some of the other surfaces we have considered. It is of course not possible to make any definitive statements about this possibility, but examination of the other surfaces shown in Fig. 3.2 based on coordination-based arguments did not suggest any obvious candidates for reconstruction.

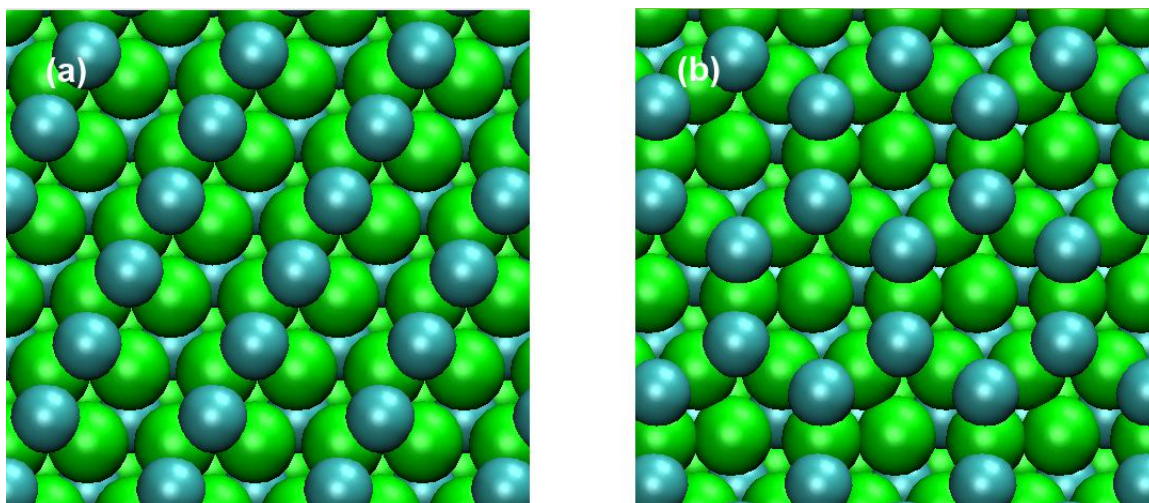


Figure 3.5: (a) Unreconstructed and (b) reconstructed bare (001) surface. Mo atoms are shown as green spheres and C atoms as blue spheres.

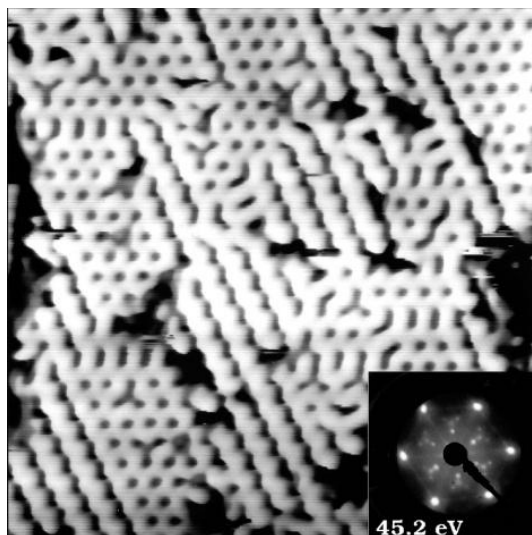


Figure 3.6: STM image of “honeycomb” structure on Mo_2C (001) surface.⁷⁴ Copyright 1999 The Japan Society of Applied Physics

Above, we argued that adsorption of K on the unreconstructed (001) surface is the most stable among the surfaces we considered. It is therefore important to compare K adsorption on the bulk terminated and reconstructed (001) surfaces. Possible adsorption sites on the reconstructed surface were determined as described above at a coverage of

32.0 Å²/atom. The binding energy of K was then calculated in the most stable site on each surface with one K adsorbed in a (2×2) surface unit cell, which gives an area of 127.9 Å²/atom. The results from these calculations are shown in Fig. 3.7. K binds on the unreconstructed (001) surface by coordinating with two C atoms and two Mo atoms. On the reconstructed surface, the adsorbed atom is coordinated with three C atoms and three Mo atoms. The adsorption energy of K on the unreconstructed (reconstructed) surface at this coverage is 2.48 eV (2.64 eV). That is, the reconstructed surface binds K more tightly than the unreconstructed surface and is therefore an appropriate surface to consider when examining the properties of K at low coverage on catalyst particles.

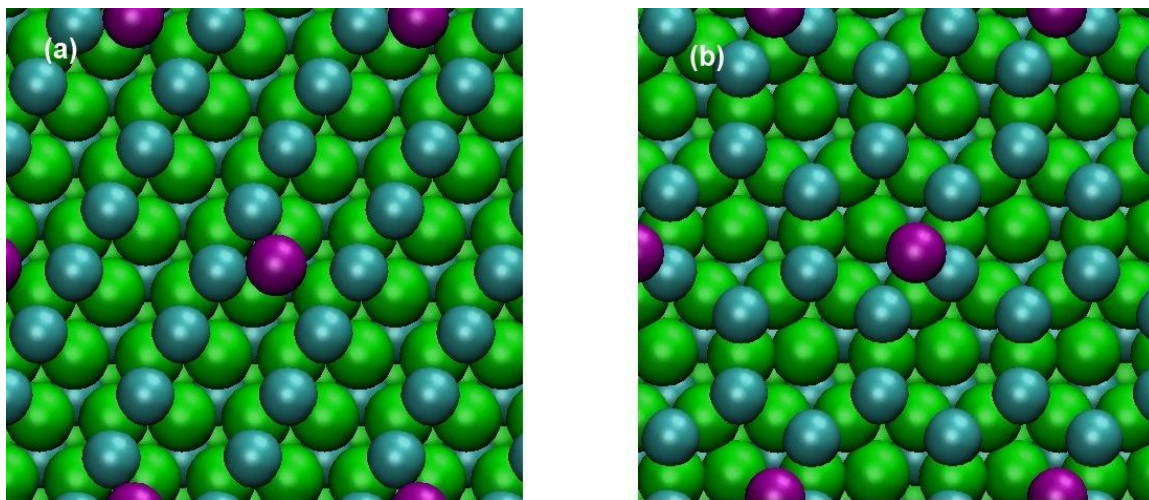


Figure 3.7: Top view of K adsorption on (a) unreconstructed and (b) reconstructed (001) surfaces. In addition to the atoms described in Fig. 3.5, K atoms are shown in purple.

3.4 Conclusions

In order to provide fundamental information on what surface of Mo₂C catalysts contribute to alkali promoted alcohol synthesis reactions, DFT calculations were performed to study the stability of seven low-index bare surfaces of α-Mo₂C and the

adsorption of alkali on those surfaces. We used the Wulff construction to predict the equilibrium crystal shape of Mo_2C using surface energies calculated from DFT. Even though the (011) surface has the lowest surface energy, we found that at low coverages, K atoms adsorb more strongly on the (001) surface. The adsorption of Rb was found to be very similar to the adsorption of K. During further investigation of the (001) surface, we observed a surface reconstruction that is favored for the bare surface in which the top layer of C atoms on the surface form hexagonal arrays. The adsorption of K was energetically favored on the reconstructed (001) surface. Our finding is in agreement with “honeycomb” structure observed in STM image of Mo_2C surface in the literature. Therefore, we conclude that the reconstructed C-terminated $\alpha\text{-Mo}_2\text{C}(001)$ is a useful representative surface structure for further surface reactivity study.

3.5 References

- (1) Liao, J. J.; Wilcox, R. C.; Zee, R. H. *Scripta Metallurgica Et Materialia* **1990**, *24*, 1647.
- (2) Hwu, H. H.; Chen, J. G. *Chem. Rev.* **2005**, *105*, 185.
- (3) Nelson, J. A.; Wagner, M. J. *Chem. Mater.* **2002**, *14*, 4460.
- (4) Kojima, R.; Aika, K. *Appl. Catal. A-Gen.* **2001**, *219*, 141.
- (5) Patt, J.; Moon, D. J.; Phillips, C.; Thompson, L. *Catal. Lett.* **2000**, *65*, 193.
- (6) Ranhotra, G. S.; Bell, A. T.; Reimer, J. A. *J. Catal.* **1987**, *108*, 40.
- (7) Park, K. Y.; Seo, W. K.; Lee, J. S. *Catal. Lett.* **1991**, *11*, 349.
- (8) Lee, J. S.; Yeom, M. H.; Lee, D. S. *J. Mol. Catal.* **1990**, *62*, L45.
- (9) Lee, J. S.; Yeom, M. H.; Park, K. Y.; Nam, I. S.; Chung, J. S.; Kim, Y. G.; Moon, S. H. *J. Catal.* **1991**, *128*, 126.
- (10) Schwartz, V.; da Silva, V. T.; Oyama, S. T. *J. Mol. Catal. A-Chem.* **2000**, *163*, 251.
- (11) Rodriguez, J. A.; Dvorak, J.; Jirsak, T. *Surf. Sci.* **2000**, *457*, L413.
- (12) Ledoux, M. J.; Cuong, P. H.; Guille, J.; Dunlop, H. *J. Catal.* **1992**, *134*, 383.
- (13) Oyama, S. T. *Catal. Today* **1992**, *15*, 179.
- (14) Woo, H. C.; Park, K. Y.; Kim, Y. G.; Nam, I. S.; Chung, J. S.; Lee, J. S. *Appl. Catal.* **1991**, *75*, 267.
- (15) Hugosson, H. W.; Eriksson, O.; Nordstrom, L.; Jansson, U.; Fast, L.; Delin, A.; Wills, J. M.; Johansson, B. *J. Appl. Phys.* **1999**, *86*, 3758.
- (16) Velikanova, T. Y.; Kublii, V. Z.; Khaenko, B. V. *Sov. Powder. Metall. Met. Ceram.* **1988**, *27*, 891.
- (17) Liu, P.; Rodriguez, J. A.; Hou, H.; Muckerman, J. T. *J. Chem. Phys.* **2003**, *118*, 7737.
- (18) Liu, P.; Rodriguez, J. A. *J. Chem. Phys.* **2004**, *120*, 5414.

- (19) Liu, P.; Rodriguez, J. A.; Asakura, T.; Gomes, J.; Nakamura, K. *J. Phys. Chem. B* **2005**, *109*, 4575.
- (20) Ren, J.; Huo, C. F.; Wang, J. G.; Cao, Z.; Li, Y. W.; Jiao, H. J. *Surf. Sci.* **2006**, *600*, 2329.
- (21) Ren, J.; Wang, J. G.; Huo, C. F.; Wen, X. D.; Cao, Z.; Yuan, S. P.; Li, Y. W.; Jiao, H. J. *Surf. Sci.* **2007**, *601*, 1599.
- (22) *Powder Diffraction File, JCPDS International Center for Diffraction Data Pennsylvania, 2004.*
- (23) Piquemal, J.-Y.; Potvin, C.; Manoli, J.-M.; Djéga-Mariadassou, G. *Catal. Lett.* **2004**, *92*, 189.
- (24) Pielaszek, J.; Mierzwa, B.; Medjahdi, G.; Mareche, J. F.; Puricelli, S.; Celzard, A.; Furdin, G. *Appl. Catal. A-Gen.* **2005**, *296*, 232.
- (25) Shi, X. R.; Wang, S. G.; Wang, H.; Deng, C. M.; Qin, Z. F.; Wang, J. G. *Surf. Sci.* **2009**, *603*, 852.
- (26) Haines, J.; Leger, J. M.; Chateau, C.; Lowther, J. E. *J. Phys.-Condens. Mat.* **2001**, *13*, 2447.
- (27) Kotarba, A.; Adamski, G.; Piskorz, W.; Sojka, Z.; Sayag, C.; Djéga-Mariadassou, G. *J. Phys. Chem. B* **2004**, *108*, 2885.
- (28) Xiang, M. L.; Li, D. B.; Xiao, H. C.; Zhang, J. L.; Li, W. H.; Zhong, B.; Sun, Y. H. *Catal. Today* **2008**, *131*, 489.
- (29) Xiang, M. L.; Li, D. B.; Li, W. H.; Zhong, B.; Sun, Y. H. *Fuel* **2006**, *85*, 2662.
- (30) Bugyi, L.; Oszko, A.; Solymosi, F. *Surf. Sci.* **2000**, *461*, 177.
- (31) Bugyi, L.; Solymosi, F. *J. Phys. Chem. B* **2001**, *105*, 4337.
- (32) King, D. A.; Woodruff, D. P. *The Chemical Physics of Solid Surfaces, Coadsorption, Promoters and Poisons*; Elsevier: Amsterdam, 1993; Vol. 6.
- (33) Haider, M. A.; Gogate, M. R.; Davis, R. J. *J. Catal.* **2009**, *261*, 9.
- (34) Kitchin, J. R.; Norskov, J. K.; Barteau, M. A.; Chen, J. G. *Catal. Today* **2005**, *105*, 66.
- (35) Ren, J.; Huo, C. F.; Wang, J. G.; Li, Y. W.; Jiao, H. J. *Surf. Sci.* **2005**, *596*, 212.

- (36) Pistonesi, C.; Juan, A.; Farkas, A. P.; Solymosi, F. *Surf. Sci.* **2008**, *602*, 2206.
- (37) Tominaga, H.; Nagai, M. *J. Phys. Chem. B* **2005**, *109*, 20415.
- (38) Tominaga, H.; Nagai, M. *Appl. Catal. A-Gen.* **2007**, *328*, 35.
- (39) Tominaga, H.; Nagai, M. *Appl. Catal. A-Gen.* **2008**, *343*, 95.
- (40) Shi, X.-R.; Wang, J.; Hermann, K. *J. Phys. Chem. C* **2010**, *114*, 13630.
- (41) Pistonesi, C.; Juan, A.; Farkas, A. P.; Solymosi, F. *Surf. Sci.* **2010**, *604*, 914.
- (42) Linic, S.; Barteau, M. A. *J. Am. Chem. Soc.* **2004**, *126*, 8086.
- (43) Liu, Z.-P.; Hu, P. *J. Am. Chem. Soc.* **2001**, *123*, 12596.
- (44) Kresse, G.; Furthmuller, J. *Phys. Rev. B* **1996**, *54*, 11169.
- (45) Kresse, G.; Hafner, J. *Phys. Rev. B* **1993**, *47*, 558.
- (46) Kresse, G.; Hafner, J. *J. Phys.: Condens. Matter* **1994**, *6*, 8245.
- (47) Sholl, D. S.; Steckel, J. A. *Density functional theory : a practical introduction*; John Wiley & Sons, Inc.: Hoboken, NJ, 2009.
- (48) Perdew, J. P.; Burke, K.; Ernzerhof, M. *Phys. Rev. Lett.* **1996**, *77*, 3865.
- (49) Perdew, J. P.; Burke, K.; Ernzerhof, M. *Phys. Rev. Lett.* **1997**, *78*, 1396.
- (50) Blöchl, P. E. *Phys. Rev. B* **1994**, *50*, 17953.
- (51) Kresse, G.; Joubert, D. *Phys. Rev. B* **1999**, *59*, 1758.
- (52) Bengtsson, L. *Phys. Rev. B* **1999**, *59*, 12301.
- (53) Neugebauer, J.; Scheffler, M. *Phys. Rev. B* **1992**, *46*, 16067.
- (54) Rudy, E.; Windisch, S.; Stosick, A. J.; Hoffman, J. R. *Transactions of the Metallurgical Society of Aime* **1967**, *239*, 1247.
- (55) Siegel, D. J.; Hector, L. G.; Adams, J. B. *Surf. Sci.* **2002**, *498*, 321.
- (56) Rapcewicz, K.; Chen, B.; Yakobson, B.; Bernholc, J. *Phys. Rev. B* **1998**, *57*, 7281.
- (57) Batyrev, I.; Alavi, A.; Finnis, M. W. *Faraday Discuss.* **1999**, *114*, 33.

- (58) Zhang, W.; Smith, J. R. *Phys. Rev. B* **2000**, *61*, 16883.
- (59) Wulff, G. Z. *Kryst. Mineral.* **1901**, *34*, 449.
- (60) Shi, H. Q.; Stampfl, C. *Phys. Rev. B* **2008**, *77*, 094127.
- (61) Soon, A.; Wong, L.; Delley, B.; Stampfl, C. *Phys. Rev. B* **2008**, *77*, 125423.
- (62) Kim, K. C.; Dai, B.; Johnson, J. K.; Sholl, D. S. *Nanotechnology* **2009**, *20*, 204001.
- (63) Šljivancanin, Ž.; Gothelf, K. V.; Hammer, B. *J. Am. Chem. Soc.* **2002**, *124*, 14789.
- (64) Bhatia, B.; Sholl, D. S. *Angew. Chem. Int. Ed.* **2005**, *44*, 7761.
- (65) Han, J. W.; Sholl, D. S. *Langmuir* **2009**, *25*, 10737.
- (66) Han, J. W.; Sholl, D. S. *Phys. Chem. Chem. Phys.* **2010**, *12*, 8024.
- (67) Henkelman, G.; Arnaldsson, A.; Jonsson, H. *Comp. Mater. Sci.* **2006**, *36*, 354.
- (68) Sanville, E.; Kenny, S. D.; Smith, R.; Henkelman, G. *J. Comput. Chem.* **2007**, *28*, 899.
- (69) Tang, W.; Sanville, E.; Henkelman, G. *J. Phys.-Condens. Mat.* **2009**, *21*, 084204.
- (70) Albano, E. V. *J. Chem. Phys.* **1986**, *85*, 1044.
- (71) Berko, A.; Erley, W.; Sander, D. *J. Chem. Phys.* **1990**, *93*, 8300.
- (72) Myli, K. B.; Grassian, V. H. *Langmuir* **1995**, *11*, 849.
- (73) Lo, R. L.; Fukui, K.; Otani, S.; Iwasawa, Y. *Surface Science* **1999**, *440*, L857.
- (74) Lo, R. L.; Fukui, K.; Otani, S.; Oyama, S. T.; Iwasawa, Y. *Japanese Journal of Applied Physics Part 1-Regular Papers Short Notes & Review Papers* **1999**, *38*, 3813.

APPENDIX 3.A

COVERAGE DEPENDENT ADSORPTION ENERGIES OF K FOR THE SIX LOW MILLER INDEX SURFACES

We assumed that the polarizability of adsorbed K is independent of the surface orientation and equal to the value deduced from K adsorption on (001), 12.06 \AA^3 . With this assumption the Albano model includes only two parameters (the adsorption energy in the limit of zero coverage and the static dipole moment of the K-Mo₂C surface bond in the limit of zero coverage), which we fitted for each surface from computed adsorption energies at three distinct coverages.

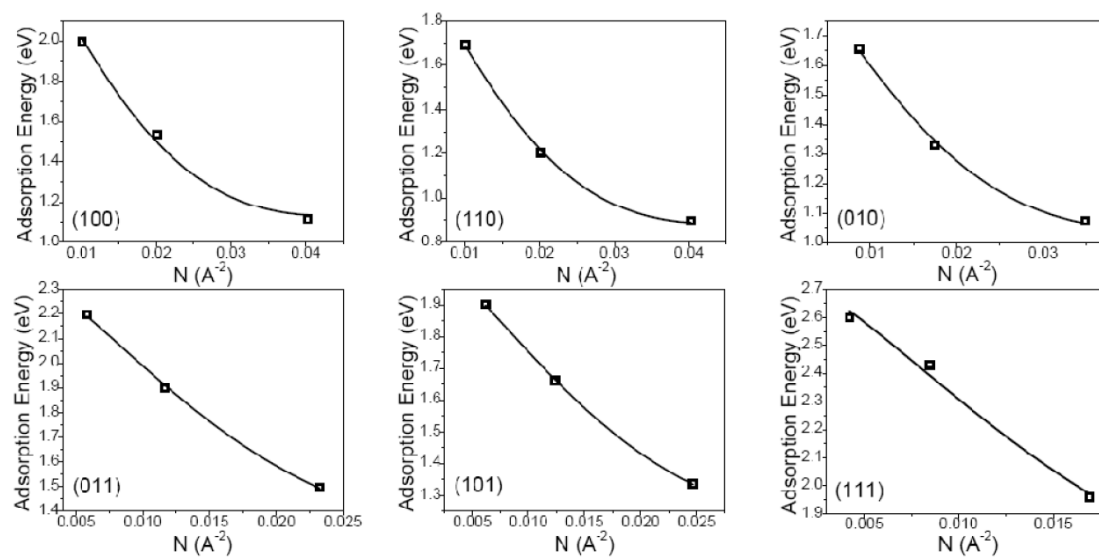


Figure 3.A.1: The adsorption energies of K at three distinct coverages on six Mo₂C surfaces as computed with DFT. The solid curves show fits of the data to the Albano model.

APPENDIX 3.B
STRUCTURE INFORMATION FOR THE OPTIMIZED
UNRECONSTRUCTED AND RECONSTRUCTED BARE (001)
SURFACES

This appendix lists the coordinates for the most stable structures of unreconstructed and reconstructed bare Mo₂C (001) surfaces discussed in this chapter. The coordinates for each surface are defined for a single supercell of a (1×1) surface unit cell with all coordinates in Å. A table defining unit cell vectors for supercell is also listed in Å.

Table 3.B.1: Unit cell vectors for a (1×1) surface used in this chapter. (in Å)

	x	y	z
a	5.268	3.036	0.000
b	0.000	6.072	0.000
c	0.000	0.000	22.296

Table 3.B.2: Fractional coordinates for a (1×1) unreconstructed bare Mo₂C (001) surface.

No.	Atom	x	y	z
1	Mo	0.164990	0.167504	0.367819
2	Mo	0.164990	0.667505	0.367818
3	Mo	0.693552	0.153222	0.368159
4	Mo	0.693551	0.653224	0.368159
5	Mo	0.990845	0.004576	0.266539
6	Mo	0.990845	0.504576	0.266539
7	Mo	0.482544	0.008726	0.261022
8	Mo	0.482544	0.508725	0.261022
9	Mo	0.184070	0.157964	0.162388
10	Mo	0.184068	0.657965	0.162388
11	Mo	0.675839	0.162080	0.156891
12	Mo	0.675839	0.662080	0.156891
13	Mo	0.973086	0.013455	0.055261
14	Mo	0.973086	0.513457	0.055261
15	Mo	0.501712	-0.000859	0.055578
16	Mo	0.501709	0.499143	0.055579
17	C	0.828858	0.335568	0.413685
18	C	0.828877	0.835558	0.413684
19	C	0.336393	0.331802	0.319216
20	C	0.336394	0.831803	0.319216
21	C	0.833325	0.333336	0.211709
22	C	0.833325	0.833336	0.211709
23	C	0.330307	0.334843	0.104211
24	C	0.330308	0.834845	0.104210
25	C	0.837831	0.331086	0.009716
26	C	0.837827	0.831087	0.009717

Table 3.B.3: Fractional coordinates for a (1×1) reconstructed bare Mo₂C (001) surface.

No.	Atom	x	y	z
1	Mo	0.125397	0.187303	0.361401
2	Mo	0.196846	0.651581	0.375069
3	Mo	0.687340	0.161500	0.372538
4	Mo	0.687340	0.651165	0.372538
5	Mo	-0.008513	0.008050	0.264783
6	Mo	-0.008512	0.500460	0.264783
7	Mo	0.498880	0.000561	0.265293
8	Mo	0.481443	0.509278	0.261460
9	Mo	0.180812	0.159591	0.162283
10	Mo	0.183950	0.658022	0.162797
11	Mo	0.673698	0.162884	0.156639
12	Mo	0.673699	0.663413	0.156639
13	Mo	0.972729	0.013357	0.055492
14	Mo	0.972729	0.513904	0.055492
15	Mo	0.502734	-0.001372	0.056194
16	Mo	0.501198	0.499396	0.056033
17	C	0.520175	0.489918	0.421657
18	C	0.827817	0.836092	0.415597
19	C	0.339377	0.331324	0.319874
20	C	0.339376	0.829304	0.319873
21	C	0.829083	0.335457	0.211830
22	C	0.835798	0.832099	0.211094
23	C	0.328486	0.335579	0.104140
24	C	0.328487	0.835924	0.104139
25	C	0.837374	0.331310	0.010163
26	C	0.836798	0.831598	0.009789

APPENDIX 3.C

STRUCTURE INFORMATION FOR K ADSORPTION IN THE MOST STABLE STATES ON BOTH UNRECONSTRUCTED AND RECONSTRUCTED BARE (001) SURFACES

This appendix lists the coordinates for the most stable structures of K adsorption on both unreconstructed and reconstructed bare Mo₂C (001) surfaces discussed in this chapter. The coordinates for the adsorbate are defined for a single supercell of a supercell of a (2×2) surface unit cell with all coordinates in Å. The shaded section of the table give the coordinates of the adsorbate; all other coordinates define the portion of the surface atoms.

Table 3.C.1: Unit cell vectors for a (2×2) surface used in this chapter. (in Å)

	x	y	z
a	10.536	6.072	0.000
b	0.000	12.143	0.000
c	0.000	0.000	22.296

Table 3.C.2: Fractional coordinates for K adsorbed on a (2×2) unreconstructed bare Mo₂C (001) surface.

No.	Atom	x	y	z	No.	Atom	x	y	z
1	Mo	0.082972	0.083164	0.368121	54	Mo	0.496532	0.752292	0.266170
2	Mo	0.082991	0.333856	0.368120	55	Mo	0.742959	0.504199	0.260233
3	Mo	0.349200	0.075391	0.367572	56	Mo	0.742930	0.754182	0.260886
4	Mo	0.348831	0.327273	0.369251	57	Mo	0.593938	0.578063	0.162212
5	Mo	0.997414	0.001262	0.266468	58	Mo	0.593920	0.828030	0.162183
6	Mo	0.997618	0.251189	0.266227	59	Mo	0.839815	0.580455	0.156921
7	Mo	0.242704	0.003634	0.261294	60	Mo	0.839971	0.830014	0.156898
8	Mo	0.242704	0.253655	0.261290	61	Mo	0.487740	0.506135	0.055393
9	Mo	0.094060	0.078017	0.162348	62	Mo	0.487844	0.756235	0.055350
10	Mo	0.094060	0.327923	0.162347	63	Mo	0.753080	0.498460	0.055278
11	Mo	0.339539	0.080228	0.156899	64	Mo	0.752825	0.748595	0.055245
12	Mo	0.339643	0.330100	0.156863	65	C	0.413706	0.168723	0.413767
13	Mo	0.988214	0.005726	0.055256	66	C	0.420913	0.415628	0.415891
14	Mo	0.988087	0.255958	0.055410	67	C	0.169536	0.165229	0.320103
15	Mo	0.252567	0.998735	0.055211	68	C	0.170306	0.414856	0.319667
16	Mo	0.252572	0.248696	0.055211	69	C	0.418121	0.165758	0.211474
17	Mo	0.583990	0.083747	0.367763	70	C	0.418357	0.415607	0.211541
18	Mo	0.584441	0.333083	0.366276	71	C	0.167045	0.166477	0.103940
19	Mo	0.848405	0.075541	0.368221	72	C	0.167095	0.416514	0.103929
20	Mo	0.847322	0.326348	0.368589	73	C	0.421173	0.164334	0.009464
21	Mo	0.496919	0.001538	0.266156	74	C	0.421667	0.414101	0.009468
22	Mo	0.496532	0.251173	0.266167	75	C	0.913642	0.168440	0.414529
23	Mo	0.742927	0.002885	0.260886	76	C	0.913685	0.417904	0.414532
24	Mo	0.742956	0.252841	0.260232	77	C	0.670267	0.164225	0.318668
25	Mo	0.593921	0.078049	0.162183	78	C	0.670572	0.414712	0.317718
26	Mo	0.593937	0.328000	0.162212	79	C	0.918854	0.165457	0.211555
27	Mo	0.839815	0.079730	0.156921	80	C	0.918856	0.415687	0.211556
28	Mo	0.839764	0.330117	0.156871	81	C	0.667138	0.166371	0.103746
29	Mo	0.487924	0.006039	0.055380	82	C	0.667012	0.416495	0.103704
30	Mo	0.487843	0.255923	0.055351	83	C	0.921797	0.164061	0.009502
31	Mo	0.752825	0.998579	0.055245	84	C	0.921800	0.414144	0.009503
32	Mo	0.753079	0.248461	0.055278	85	C	0.420915	0.663440	0.415890
33	Mo	0.084644	0.582883	0.368108	86	C	0.413727	0.917550	0.413768
34	Mo	0.084625	0.832478	0.368109	87	C	0.170819	0.664593	0.319209
35	Mo	0.347728	0.576130	0.370861	88	C	0.170299	0.914839	0.319676
36	Mo	0.348832	0.823889	0.369254	89	C	0.418356	0.666038	0.211542
37	Mo	0.997412	0.501322	0.266468	90	C	0.418120	0.916118	0.211475
38	Mo	0.997392	0.751303	0.266652	91	C	0.167113	0.666444	0.103959
39	Mo	0.243295	0.503258	0.261183	92	C	0.167096	0.916391	0.103931
40	Mo	0.243294	0.753449	0.261187	93	C	0.421661	0.664242	0.009469
41	Mo	0.094131	0.577886	0.162354	94	C	0.421166	0.914502	0.009463
42	Mo	0.094130	0.827983	0.162356	95	C	0.915756	0.667055	0.413863
43	Mo	0.339786	0.580108	0.156897	96	C	0.915708	0.917208	0.413861
44	Mo	0.339644	0.830257	0.156863	97	C	0.670273	0.665500	0.318667
45	Mo	0.988213	0.506063	0.055256	98	C	0.669115	0.915442	0.319726
46	Mo	0.988239	0.755883	0.055140	99	C	0.918752	0.665779	0.211723
47	Mo	0.252856	0.498579	0.055299	100	C	0.918750	0.915468	0.211723
48	Mo	0.252854	0.748568	0.055299	101	C	0.667138	0.666492	0.103746
49	Mo	0.584443	0.582471	0.366276	102	C	0.667195	0.916402	0.103823
50	Mo	0.584001	0.832252	0.367764	103	C	0.921340	0.664373	0.009380
51	Mo	0.848411	0.576055	0.368229	104	C	0.921340	0.914294	0.009380
52	Mo	0.848458	0.825760	0.367962	105	K	0.610272	0.444857	0.511373
53	Mo	0.495877	0.502061	0.266294					

Table 3.C.3: Fractional coordinates for K adsorbed on a (2×2) reconstructed bare Mo₂C (001) surface.

No.	Atom	x	y	z	53	Mo	0.510750	0.496225	0.267406
1	Mo	0.077781	0.085726	0.364239	54	Mo	0.510750	0.743032	0.267406
2	Mo	0.114412	0.317797	0.377970	55	Mo	0.764124	0.492941	0.267946
3	Mo	0.358854	0.072792	0.375960	56	Mo	0.755541	0.747782	0.264504
4	Mo	0.358855	0.318358	0.375960	57	Mo	0.604959	0.572525	0.165211
5	Mo	0.010793	0.996413	0.267926	58	Mo	0.606625	0.821805	0.165726
6	Mo	0.011205	0.242457	0.267597	59	Mo	0.851357	0.574373	0.159802
7	Mo	0.264439	0.992636	0.268670	60	Mo	0.851327	0.824601	0.159928
8	Mo	0.255387	0.247308	0.264481	61	Mo	0.500610	0.499553	0.058687
9	Mo	0.104885	0.072465	0.165366	62	Mo	0.500610	0.749845	0.058687
10	Mo	0.106903	0.321552	0.165827	63	Mo	0.765827	0.492090	0.059274
11	Mo	0.351582	0.074223	0.159949	64	Mo	0.765079	0.742496	0.059027
12	Mo	0.351582	0.324201	0.159949	65	C	0.275332	0.237339	0.425067
13	Mo	0.000612	0.999531	0.058837	66	C	0.430199	0.409761	0.419285
14	Mo	0.000889	0.249720	0.058765	67	C	0.184913	0.158009	0.322964
15	Mo	0.265761	0.992161	0.059358	68	C	0.184913	0.407082	0.322962
16	Mo	0.264844	0.242582	0.059028	69	C	0.429477	0.160265	0.215192
17	Mo	0.577190	0.086407	0.364675	70	C	0.432484	0.408478	0.214156
18	Mo	0.613609	0.319536	0.378249	71	C	0.179152	0.160320	0.107308
19	Mo	0.858400	0.073656	0.376310	72	C	0.179152	0.410538	0.107308
20	Mo	0.858481	0.318607	0.374798	73	C	0.433436	0.158287	0.013263
21	Mo	0.511108	0.996188	0.267974	74	C	0.432932	0.408453	0.012832
22	Mo	0.511108	0.242711	0.267974	75	C	0.776268	0.239503	0.425580
23	Mo	0.764884	0.992560	0.269249	76	C	0.929953	0.410024	0.418952
24	Mo	0.755541	0.246681	0.264503	77	C	0.684648	0.158313	0.323633
25	Mo	0.605236	0.072386	0.165538	78	C	0.684694	0.407100	0.322255
26	Mo	0.606626	0.321579	0.165726	79	C	0.929141	0.160274	0.214973
27	Mo	0.851328	0.074079	0.159928	80	C	0.932812	0.408597	0.214082
28	Mo	0.851357	0.324277	0.159802	81	C	0.678975	0.160407	0.107212
29	Mo	0.500708	-0.000457	0.058836	82	C	0.678901	0.410534	0.107090
30	Mo	0.500709	0.249757	0.058836	83	C	0.933763	0.158166	0.013199
31	Mo	0.765772	0.992118	0.059344	84	C	0.933014	0.408497	0.012825
32	Mo	0.765080	0.242433	0.059026	85	C	0.274412	0.737794	0.425557
33	Mo	0.077782	0.586496	0.364239	86	C	0.430195	0.910045	0.419285
34	Mo	0.113493	0.818255	0.378339	87	C	0.185058	0.658181	0.323101
35	Mo	0.358861	0.573370	0.376345	88	C	0.185059	0.906763	0.323101
36	Mo	0.358861	0.817772	0.376346	89	C	0.429005	0.660502	0.214724
37	Mo	0.011204	0.496344	0.267596	90	C	0.432484	0.909045	0.214157
38	Mo	0.010793	0.742800	0.267926	91	C	0.178851	0.660561	0.107204
39	Mo	0.264439	0.492929	0.268670	92	C	0.178851	0.910598	0.107204
40	Mo	0.255918	0.747043	0.264698	93	C	0.433388	0.658311	0.013134
41	Mo	0.104885	0.572659	0.165366	94	C	0.432931	0.908625	0.012832
42	Mo	0.106658	0.821676	0.165907	95	C	0.776274	0.734227	0.425580
43	Mo	0.351195	0.574183	0.159829	96	C	0.928762	0.910623	0.419270
44	Mo	0.351195	0.824630	0.159829	97	C	0.684693	0.658211	0.322256
45	Mo	0.000888	0.499397	0.058765	98	C	0.684649	0.907042	0.323634
46	Mo	0.000612	0.749862	0.058836	99	C	0.929140	0.660593	0.214973
47	Mo	0.265761	0.492087	0.059358	100	C	0.932505	0.908751	0.214344
48	Mo	0.264848	0.742581	0.059062	101	C	0.678900	0.660575	0.107090
49	Mo	0.575644	0.587180	0.363227	102	C	0.678974	0.910628	0.107213
50	Mo	0.613610	0.816859	0.378250	103	C	0.933762	0.658078	0.013199
51	Mo	0.858482	0.572913	0.374798	104	C	0.932881	0.908563	0.012843
52	Mo	0.858400	0.817947	0.376310	105	K	0.768329	0.490832	0.528796
53	Mo	0.510750	0.496225	0.267406					

CHAPTER 4

ANALYSIS OF SYNGAS REACTION NETWORK TO IDENTIFY THE SELECTIVITY DETERMINING ELEMENTARY STEPS

4.1 Introduction

With limited fossil fuel resources, extensive research efforts have been devoted to find alternative building blocks in the chemical industry. Among many candidates, syngas is potentially promising as it can be either derived from conventional sources such as coal and natural gas, or renewable sources like biomass.^{1,2} Syngas can be converted to downstream products directly through syngas reactions. However, since these reactions produce a series of products, managing reaction selectivity often turns out to be critical.³⁻⁹

Molybdenum carbides have been reported in many catalysis applications such as steam reforming,¹⁰⁻¹² Fischer-Tropsch synthesis,¹³⁻¹⁷ water gas shift,¹⁸⁻²⁰ and higher alcohol synthesis,²¹⁻²³ due to their noble-metal-like catalytic properties, relative low cost, and resistance to poisoning. More interestingly, as a syngas reaction catalyst, molybdenum carbides were found to shift reaction selectivity significantly from hydrocarbons to alcohols with alkali promoters.^{21,23,24} In principle, understanding the relation between selectivity and catalyst structure could eventually help us designing catalyst selective to specific product. However, little progress has been made in this endeavor to date due to the complexity of the syngas reaction mechanism.

A number of theoretical studies have been performed for Mo₂C on structure information,²⁵⁻²⁹ adsorption behavior,²⁵⁻²⁸ stability,^{25,26,29-31} and catalytic

performance.^{27,32-35} Recently, Medford et al. applied *ab initio* thermodynamics and DFT to study the stability of surface structures of Mo₂C and adsorption of reactive intermediates as well as C-O bond dissociation on the Mo₂C surface.³⁶ Pistonesi et al. studied adsorption of alkali metal on Mo₂C surfaces and its effect on CO adsorption and dissociation.³⁷ Tominaga et al. reported energetics of CO hydrogenation and C-O bond cleavage on molybdenum and cobalt molybdenum carbide catalysts.³⁸ Most of these studies focus on specific elementary steps, with the inherent assumption that this gives an adequate descriptor of catalyst performance. This could be potentially problematic for several reasons: 1) these steps might not have the lowest activation energy among competing processes; 2) these steps might be the lowest activation-energy steps, but still not necessarily the rate-determining steps (RDS), since kinetically, reaction rates also depend on surface coverage; 3) these steps might be the RDS for certain products, but not necessarily the ones responsible for controlling overall selectivity. Addressing these issues are especially important for a complex reaction system where reaction pathways could be numerous and intricate.

Motivated by these observations, in this chapter, we seek to provide a broad perspective on syngas reaction using a Mo₂C catalyst by describing a complex reaction network and determining which steps contribute most to the overall reaction selectivity. Specifically, we first develop a reaction network containing relevant syngas reactions, including Fischer-Tropsch synthesis, methanol synthesis, ethanol synthesis and water gas shift reaction. All the reaction energies in this network were calculated by Density Functional Theory (DFT) while activation energies were approximated by Bronsted-Evans-Polanyi (BEP) relations. With these energies as inputs, a microkinetic

model was formulated and the reaction selectivity was computed and compared with experimental results. Finally, sensitivity analysis was applied to determine the overall model's sensitivity on changes of each elementary step. This chapter gives insights into the reaction mechanism of syngas reactions on Mo₂C catalysts and serves as a useful example of determining descriptors for a complex reaction network.

4.2 Computational methods

Our plane wave DFT calculations were performed with the Vienna *ab initio* simulation package (VASP).³⁹⁻⁴² We employed the revised Perdew-Burke-Ernzerhof (rPBE) generalized gradient functional^{43,44} along with the projector augmented wave (PAW)^{45,46} method to describe ionic cores. A plane wave expansion with a cutoff of 400 eV was used for all calculations. Geometries were relaxed using a conjugate gradient algorithm until the forces on all unconstrained atoms were less than 0.03 eV/Å.

For surface structure calculation, a 6×6×1 Monkhorst-Pack k-point mesh was used for (1×1) surface unit cell, which was sufficient to give well-converged results. For calculations on a (2×2) surface unit cell, the number of k-points in the Monkhorst-Pack meshes was reduced to 3×3×1. Geometries and energies for gas phase species were calculated using supercells equivalent to those for the largest slab calculations. When examining adsorption, molecules were placed on only one side of the slab. Dipole corrections were therefore applied in computing all of the energies reported below.^{47,48} The adsorption energy, $E_{\text{adsorption}}$, of an atom or molecule was defined by

$$E_{\text{adsorption}} = (E_{\text{surface}} + E_{\text{adsorbate}}) - E_{\text{total}} \quad (4.1)$$

where E_{total} is the total energy of the system containing the adsorbed species, E_{surface} is the total energy for the optimized bare surface, and $E_{\text{adsorbate}}$ is the total energy for the adsorbate in the gas phase. With this definition, positive adsorption energies correspond to energetically favored states. Adsorbate coverages were defined by considering a surface with an adsorbed species on every surface molybdenum atom to have coverage of 1 monolayer (ML). This means that placing one adsorbate in a 1×1 unit cell gives a coverage of 0.25 ML.

4.3 Results and Discussion

4.3.1 Bulk and surface structure of Mo_2C catalyst

The bulk and surface structures of the molybdenum carbide catalyst modeled in this chapter are based on the work discussed in Chapter 3.²⁶ In Chapter 3, lattice parameters of the hexagonal Mo_2C bulk structure were confirmed to be in good agreement with experimental results. By comparing surface free energy and adsorption energy of alkali metal (K and Rb) atoms for different low-Miller-index surfaces of Mo_2C , the $\text{Mo}_2\text{C}(001)$ surface was determined to be one of the major surfaces found on Mo_2C particles in equilibrium as well as the one having the greatest affinity and dipole moment for K/Rb atoms. This surface is also known to favor a reconstruction in the absence of adsorbates,^{49,50} which results in both Mo-top and C-top sites for adsorption. As we demonstrate below, reaction intermediates adsorb on both Mo-top and C-top sites, so we believe a surface model including Mo-top and C-top sites is more appropriate to represent overall reactivity of Mo_2C than pure Mo-terminated surface or C-terminated surface. Given all the factors mentioned above, the reconstructed hexagonal $\text{Mo}_2\text{C}(001)$ surface

illustrated in Fig. 4.1 was chosen as a representative Mo_2C surface for further calculations.

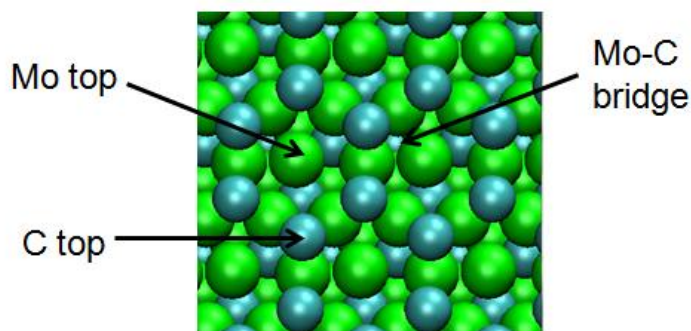


Figure 4.1. Top view of reconstructed C-terminated Mo_2C (001) surface used in this chapter. Molybdenum and carbon atoms are depicted in green and cyan respectively.

4.3.2 Syngas reaction network

As mentioned earlier, syngas reaction on Mo_2C catalysts can generate products including hydrocarbons, alcohols, water and CO_2 . In order to model reaction selectivity, reaction pathways towards all of these products should be considered, which involves water gas shift reactions, Fischer-Tropsch (FT) synthesis, methanol synthesis and higher alcohol synthesis. A tremendous amount of research has been performed to understand the mechanisms of these four types of reactions.^{3-7,51-57} In terms of theoretical studies, Cheng et al. performed DFT calculation for Fischer-Tropsch(FT) synthesis on Co,^{58,59} Ru, Fe, Rh, and Re surfaces⁶⁰ and analyzed the C-C chain growth mechanism.^{61,62} Choi et al. performed extensive DFT calculations to investigate ethanol synthesis on Rh(111).⁶³ Grabow et al. presented a comprehensive mean-field microkinetic model for the methanol synthesis and water-gas-shift reactions.⁶⁴ Similar studies have been done by Gokhale et al.,⁶⁵ Madon et al.,⁶⁶ Grabow et al.,⁶⁷ Ferrin et al.,⁶⁸ and Mei et al..⁶⁹ Although

these calculations have been an important tool in elucidating reaction mechanisms, most reaction mechanisms are still under debate, or only understood for certain catalyst system.

In this chapter, for Fischer-Tropsch synthesis, we include various $\text{CH}_x\text{-CH}_y$ coupling reactions suggested by a carbene mechanism.⁷⁰ For ethanol synthesis, we focus on the most studied CO-insertion mechanism,^{63,71,72} where C_2 oxygenates can be formed by $\text{CH}_x\text{-CO}$ coupling. For methanol synthesis, although direct CO hydrogenation ($\text{CO} + 2\text{H}_2 \rightarrow \text{CH}_3\text{OH}$) is often assumed to be the main reaction mechanism, it was suggested that for Cu-based catalysts, CO_2 hydrogenation ($\text{CO}_2^* \rightarrow \text{HCOO}^* \rightarrow \text{H}_2\text{COO}^* \rightarrow \text{H}_3\text{COO}^* \rightarrow \text{H}_3\text{CO}^* \rightarrow \text{CH}_3\text{OH}^*$) was actually responsible for producing methanol.⁷³⁻⁷⁶ Therefore, we include both CO and CO_2 hydrogenation to investigate which one prevails. For water gas shift reactions, both redox and carboxyl mechanisms were included in the network. The former assumes CO is oxidized by atomic O produced from H_2O dissociation,⁷⁷⁻⁷⁹ while the latter involves formation of an intermediate carboxyl group COOH ($\text{CO}^* + \text{OH}^* \rightarrow \text{COOH}^* \rightarrow \text{CO}_2^* + \text{H}^*$).^{65,67} The schematic reaction network is shown in Fig. 4.2. A list of all 53 elementary steps in this network can be found in the Appendix 4.B.

above the (1 × 1) surface unit cell. Most of the intermediates prefer to adsorb on Mo top, C top or Mo-C bridge site, as shown in Fig. 4.1. A list of most (second most) stable site for 31 reaction intermediates can be found in the Appendix 4.A. The adsorption energies of 9 gas phase species were calculated in a similar way in Table 4.1.

Table 4.1. Adsorption energy of gas phase species as computed with DFT.

Species	Adsorption energy (eV/molecule)
CO	1.46
H ₂	1.11
CH ₄	0.11
CH ₃ OH	0.54
H ₂ O	0.61
CO ₂	0.16
C ₂ H ₄	0.55
C ₂ H ₆	0.03
C ₂ H ₅ OH	0.05

As expected, CO was found to be most strongly adsorbed species. As is well known, DFT calculations of this kind tend to overestimate adsorption energies.⁸¹ To address this point, for CO, we compared our computed adsorption energy with TPD experiment results for Mo₂C in Table 4.2. Adsorption energies are not directly measured in TPD experiment, but it can be easily estimated from TPD peak temperature by the Redhead equation.⁸² Two peaks were identified in TPD, which correspond to 1.17 eV/molecule and 0.85 eV/molecule, with energy difference of ~0.3 eV/molecule. On the other hand, in our DFT calculation, CO was found to be adsorbed on Mo top (most stable site) and C top (second most stable site), also with ~0.3 eV/atom energy difference. This supports assigning the two TPD peaks to CO adsorption on Mo top and C top sites.

It is also supported by our earlier results, comparing vibrational frequencies calculated from DFT with IR experiments.²⁴

Table 4.2. Comparison between adsorption energy calculated from TPD peak temperature and DFT-rPBE functional.

Adsorption	TPD peak temperature ⁸³ (adsorption energy*)	Computed adsorption energy from DFT
CO on Mo top	450 K (1.17 eV/molecule)	1.46 eV/molecule
CO on C top	328 K (0.85 eV/molecule)	1.18 eV/molecule
Difference	(0.32 eV/molecule)	0.28 eV/molecule

* Adsorption energy calculated from peak temperature using the Redhead equation with assumed prefactor of $1 \times 10^{13} \text{ s}^{-1}$.

Based on the observations above, we corrected the CO adsorption energy in our model by a factor of 0.8 based on the ratio of the TPD experiment value (1.17 eV/molecule) to the DFT computed value (1.46 eV/molecule) shown above. To be consistent, we also applied this correction factor to the other eight gas phase species in the reaction network. TPD experimental results for these eight species are not readily available. For all the other species adsorbed as reaction intermediates, we chose not to apply this correction since the impact of overestimating their adsorption energies will be cancelled out in the further reaction enthalpy calculation.

4.3.4 Approximation of activation energy

Because of the large number of transition states that would have to be determined to treat each activated process in our reaction network rigorously, our model applied a Bronsted-Evans-Polanyi (BEP) relation to approximate activation energy for all elementary steps. The BEP relation, states that there is an approximately linear relation between activation energy and reaction enthalpy:

$$E_a = \alpha \cdot \Delta H + E_0 \quad (4.2)$$

Several types of bond activation, such as C-C, C-H, C-O bond breaking, on various transition metal surfaces have been examined extensively to test the validity of the BEP approximation.⁸⁴⁻⁸⁷ Here, we employ the parameters reported by Michaelides et al.⁸⁴, where for dehydrogenation reactions,

$$E_a^{\text{diss}} = 0.92\Delta H + 0.87 \quad (4.3)$$

for diatomic activation reactions,

$$E_a^{\text{diss}} = 0.97\Delta H + 1.69 \quad (4.4)$$

and for triatomic activation reactions,

$$E_a^{\text{diss}} = 0.74\Delta H + 1.03, \text{ with all energies in eV.} \quad (4.5)$$

From the principle of reversibility, the activation energy for bond association can be calculated by

$$E_a^{\text{diss}} = E_a^{\text{asso}} + \Delta H \quad (4.6)$$

For each elementary step ($A^* + B^* \rightarrow C^* + D^*$), the reaction enthalpy, ΔH was calculated by

$$\Delta H = E_{C^*} + E_{D^*} - E_{A^*} - E_{B^*} \quad (4.7)$$

where $E_{\text{adsorbate } *}$ can be calculated from DFT calculations.

It should be noted that the correlation used here was developed for transition metal surfaces, rather than transition metal carbides. Thus, when elementary steps happen on surface carbidic site, proper parameters should be chosen carefully. For example, diatomic activation on carbidic site used the triatomic activation parameters shown above. Although in principle, parameters for transition metal carbide surface should be developed, this is a useful way to rapidly estimate activation energies for transition metal

carbide surfaces. A list of activation energy for all steps can be found in the Appendix 4.B.

4.3.5 Microkinetic model

4.3.5.1 Quasi-chemical approximation

With all the energetics available, we can compute reaction rates with a microkinetic model. The most widely applied models for this goal are mean field (MF) and kinetic Monte Carlo (kMC) models⁸⁸. Kinetic Monte Carlo requires predefining the rate of each process (adsorption, reaction, diffusion, etc.) at certain local ordering conditions (interaction with nearby species). We chose not to use kMC because of the complexity of the reaction network we are considering. It was important, however, to adopt an approach beyond the MF level to account for adsorbate-adsorbate interaction. To this end, we used the quasi-chemical approximation (QCA),⁸⁹⁻⁹¹ which assumes there is chemical equilibrium on redistribution of adsorbed species as shown below in Fig. 4.3.

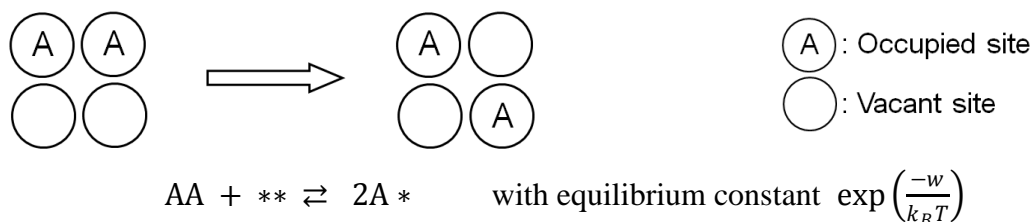


Figure 4.3. Schematic showing the quasi-chemical approximation.

To use the QCA, the interaction energy w between nearest neighbors must be defined. Our model includes 31 distinct adsorbates. For simplicity, w is approximated as the interaction energy between dominant species on the surface. As shown below, oxygen was found to be the dominant species on the surface under typical experimental

conditions. Therefore, the interaction energy between two adsorbed oxygen atoms on the Mo₂C surface was calculated from DFT and used in the application of QCA to all adsorbed gas phase species. The effect of interaction on adsorption, desorption and surface reactions is discussed below.

4.3.5.2 Adsorption, desorption and surface reaction rates

For adsorption of a gas phase species, the rate is defined in kinetic theory by⁹²

$$r_{ads} = \sigma(1 - \sum\theta_i)e^{-\frac{E_{a,ads}}{k_B T}} \cdot \frac{P}{\sqrt{2\pi m k_B T}} \quad (4.8)$$

where σ is the steric factor which represents the probability that a molecule possessing sufficient energy $E_{a,ads}$ and colliding with a vacant site will adsorb, $E_{a,ads}$ is activation energy of adsorption process, P is the partial pressure of the adsorbing species, m is mass of the species, k_B is Boltzmann's constant, and T is temperature. The term $(1 - \sum\theta_i)$, where θ_i is the fractional surface coverage of species i , represents the probability that a collision occurs with an empty site. In this work, σ is assumed to be 1, and $E_{a,ads}$ is zero by assuming the adsorption is non-activated process.

For desorption, the rate is defined by⁹²

$$r_{des} = \nu L \theta_i e^{-\frac{E_{a,des}}{k_B T}} \quad (4.9)$$

where ν is the vibrational frequency assumed to be $1 \times 10^{13} \text{ s}^{-1}$, L is the site density, and $E_{a,des}$ is the activation energy for the desorption process, which is taken to be equal to the adsorption energy E_{ad} .

Interaction between adsorbed species can be important in a desorption process. For instance, with strong repulsive interaction, it is expected desorption will happen more

easily at higher surface coverage. Thus, based on QCA, a correction factor g was applied to desorption rate expression as:

$$r_{des} = \nu L \theta_i e^{-\frac{E_{a,des}}{k_B T}} \cdot g \quad (4.10)$$

Here, g is a function of nearest neighbor interaction energy w , vacant site coverage θ_* , temperature T , and number of nearest neighbored sites z .

$$g = \left[\frac{2-2(1-\theta_*)}{1+\beta-2(1-\theta_*)} \right]^z \quad (4.11)$$

where

$$\beta = \left[1 - 4\theta_*(1-\theta_*)(1 - \exp\left(\frac{-w}{k_B T}\right)) \right]^{1/2} \quad (4.12)$$

This correction keeps the desorption rates as a closed form equation. We compared the performance of MF, QCA, and Monte Carlo models for a simple adsorption/desorption process, finding that the QCA description is accurate in many regime where the MF calculations was inaccurate. Details of these calculations can be found in the Appendix 4.C.

For surface reactions, the rate was defined by Transition State Theory as⁹²

$$r_i = A \exp\left(\frac{-E_{act,i}}{k_B T}\right) \quad (4.13)$$

Here, r_i is the rate constant of step i , A is a pre-exponential factor assumed to be 10^{13} s^{-1} , $E_{act,i}$ is the activation energy of step i . Although adsorbate-adsorbate interaction can influence surface reaction rates, we treated these reactions at an MF level for simplicity.

4.3.5.3 Governing equations and solving technique

With adsorption, desorption and surface reaction rates defined, the derivative of surface coverage over time for each species was defined as:

$$\frac{d\theta_i}{dt} = (\text{rate of formation of species } i) - (\text{rate of consumption of species } i) \quad (4.14)$$

Traditional methods of solving rate equations, such as Langmuir-Hinshelwood (L-H) model or Hougen-Watson (H-W) model,⁹² involve simplifying reaction sequence to derive an analytical close-form rate expression. This often requires assuming a specific step to be the rate determining step (RDS). For example, L-H model assumes a RDS surface reaction governs the rate and all adsorption/desorption steps are quasi-equilibrated. These models are often good enough to correlate experimental data for simple reactions with a single linear sequence. However, for complex reactions, where there are reactions split into multiple linear sequences and interconnections between different sequences, a closed-form rate expression cannot readily be derived. Moreover, as the goal of this work is to determine rate and selectivity limiting steps, clearly, no assumption should be made on them prior to solving the model.

Thus, our model chose to solve the above equations numerically without imposing assumptions on reaction mechanism. Specifically, at steady state, the derivative of surface coverage over time equals to zero for each surface species, which gives N (but $N-1$ independent) equations, plus with surface site balance $\sum_1^N \theta_i = 1$. Here, N is the number of surface species including vacant site. This formulates an algebraic equation set with N equations and N unknown surface coverages. Then it can be solved numerically with Matlab fsolve function. Because the rate constant terms in the equation set could differ in several orders of magnitude, variables were properly scaled to equalize their effect on the objective and constraint functions. Also, as a nonlinear optimization problem, initial estimate of the surface coverages is needed. This estimate was obtained from time evolution of θ_i by solving $\frac{d\theta_i}{dt}$ with Matlab solver for stiff ODEs, assuming that

at $t = 0$, the surface was complete empty ($\theta_* = 1$). A mass balance was performed to confirm equations were solved correctly.

4.3.6 Results

4.3.6.1 Surface coverage

The steady state surface coverage solved from the microkinetic model under typical experimental conditions is shown below in Table 4.3. A list of coverages for all 32 species can be found in the Appendix 4.D.

Table 4.3. Steady state surface coverages at typical experimental condition (573 K, 30 bar of syngas with CO:H₂ in an 1:1 ratio).

No.	Species	Coverage
1	O*	62.3%
2	CO*	21.5%
3	CH ₂ *	3.2%
4	*	2.9%
5	CHO*	2.1%
6	CH ₃ CH ₂ O*	1.9%
7	CH ₃ *	1.8%
8	C ₂ H ₅ *	1.8%
9	CH ₃ CO*	1.8%
10-32	Other 23 species	0.7%
	Sum	100%

Under the chosen conditions (573 K, 30 bar of syngas, CO:H₂ = 1:1), oxygen was found to be the most abundant species on the surface at steady state. This is an interesting, but not entirely surprising result. There has been multiple studies reporting that a molybdenum oxycarbide phase could be formed *in-situ* over Mo₂C catalyst under syngas reaction conditions.⁹³⁻⁹⁸ Our results shows that surface oxygen originating from CO, tends to accumulate on Mo₂C catalytic surface when a steady state is reached. It is

important to note that the total surface coverage is high; less than 3% of the surface sites are unoccupied.

4.3.6.2 Selectivity

With the surface coverage at steady state, the production rates of six gas phase products were calculated. The product selectivities, defined as the percentage of specific production rate within the overall production rate, are listed in Table 4.4. In order to compare with experimental results, we reported the computed selectivity using carbon% based notation used in the experimental data of Shou et al..⁸⁰ The selectivity to product i is based on the total number of carbon atoms in the product and is therefore defined as

$$Selectivity (\%) = \frac{n_i M_i}{\sum n_i M_i} \times 100 \quad (4.15)$$

where n_i is the number of carbon atoms in product i and M_i is the percentage of product i .

Table 4.4. Comparison between computed and experimental selectivities, using experimental data from Shou et al..⁸⁰

Species	Computed Selectivity	Experimental Selectivity ⁸⁰
CO₂	47.7%	46%
Selectivity (on a CO ₂ -free basis)		
Total hydrocarbons	82.9%	89%
CH ₄	36.7%	33%
C2+ hydrocarbons	46.2%	56%
	(3.1% C ₂ H ₄ +43% C ₂ H ₆)	
Total alcohols	17.1%	11%
CH ₃ OH	0.2%	4.9%
C2+ alcohols	16.9%	6.1%

Reaction condition at 573 K, 30 bar of syngas with CO/H₂ = 1:1

As can be seen in Table 4.4, our computed selectivities are in good agreement with experimental results. As expected, besides CO₂ as a major byproduct, the unpromoted Mo₂C catalyst primarily produces hydrocarbons (80%~90% selectivity on CO₂ free basis) rather than alcohols. Most of hydrocarbons were in form of paraffin, although some olefins were also observed. It is important to emphasize that our model was not fitted in any way to the experimental data shown in Table 4.4. The consistency between the predictions of our first-principle-based model and this experimental data gives us confidence that our model can be used in a predictive sense for this complex catalytic system.

4.3.6.3 Effect of temperature and pressure on selectivity

With good agreement reached at benchmark reaction condition (573 K, 30 bar of syngas with CO/H₂ = 1:1) used in the experiment, the performance of our model was further tested under different temperature and pressure conditions, as shown in Table 4.5 and 4.6.

Table 4.5. Selectivities of total hydrocarbons and total alcohols at different temperatures (on CO₂-free basis).

Species	548 K	573 K	598 K
Total hydrocarbons	82.6%	82.9%	83.3%
Total alcohols	17.4%	17.1%	16.7%

Table 4.6. Selectivities of total hydrocarbons and total alcohols at different pressures (on CO₂-free basis).

Species	20 bar	30 bar	40 bar
Total hydrocarbons	84.5%	82.9%	81.8%
Total alcohols	15.5%	17.1%	18.2%

Our model shows that with increasing temperature, the selectivity of total hydrocarbons increases at the expense of selectivity to alcohols. This is consistent with the trend observed experimentally,⁹⁹ where it was proposed that alcohol synthesis reactions are more exothermic than Fischer-Tropsch synthesis. The trend of hydrocarbon and alcohol selectivities as a function of pressure also match the experimental results,⁹⁹ where higher syngas pressure made the catalysts more selective to alcohols. This could be explained as a surface coverage effect, where at higher pressure, more CO* enhances alcohol production through CO-insertion mechanism.

4.3.6.4 Reaction rates at steady state

Based on the comparison above with experimental results, we can be confident that our reaction network usefully describes the mechanism of syngas reactions over Mo₂C. To clearly demonstrate the reaction mechanism, we calculated the rates of all individual elementary steps in the network at steady state under the benchmark reaction condition (573 K, 30 bar with CO:H₂ = 1:1), and plotted them in Fig. 4.4. The numbers in red are the elementary step rates in units of molecule per second per site. For simplicity, steps along the same reaction route with the same rate are only be labeled once. To better visualize our results, we drew arrows to qualitatively represent these rates, where a broader arrow indicates a larger rate. As shown in Fig. 4.4, certain pathways within the overall network dominate. For instance, for water gas shift reactions, the pathway going through CO* (redox mechanism) is 10⁴ times faster than the one via COOH* (carboxyl mechanism). Similarly, for methanol production, although CO₂ hydrogenation mechanism has been reported to be dominant on Cu based catalyst,^{64,73,75,76} our results

suggest that methanol is mainly produced through a CO hydrogenation mechanism on Mo_2C .

One issue receiving growing attention recently is how adsorbed CO dissociates on catalyst surfaces. Historically, it has long been considered that CO^* directly dissociates into C^* and O^* .^{70,71,100} However, more evidence in recent years, both theoretically and experimentally,¹⁰¹⁻¹⁰³ indicates that CO^* can dissociate with the assistance of hydrogen. H-assisted CO dissociation involves a two-step process: adsorbed CO is first hydrogenated to H_xCO^* , and then dissociates to CH_x^* and O^* . Our results are an example of this phenomenon, where H-assisted CO dissociation is dominant over direct CO dissociation.

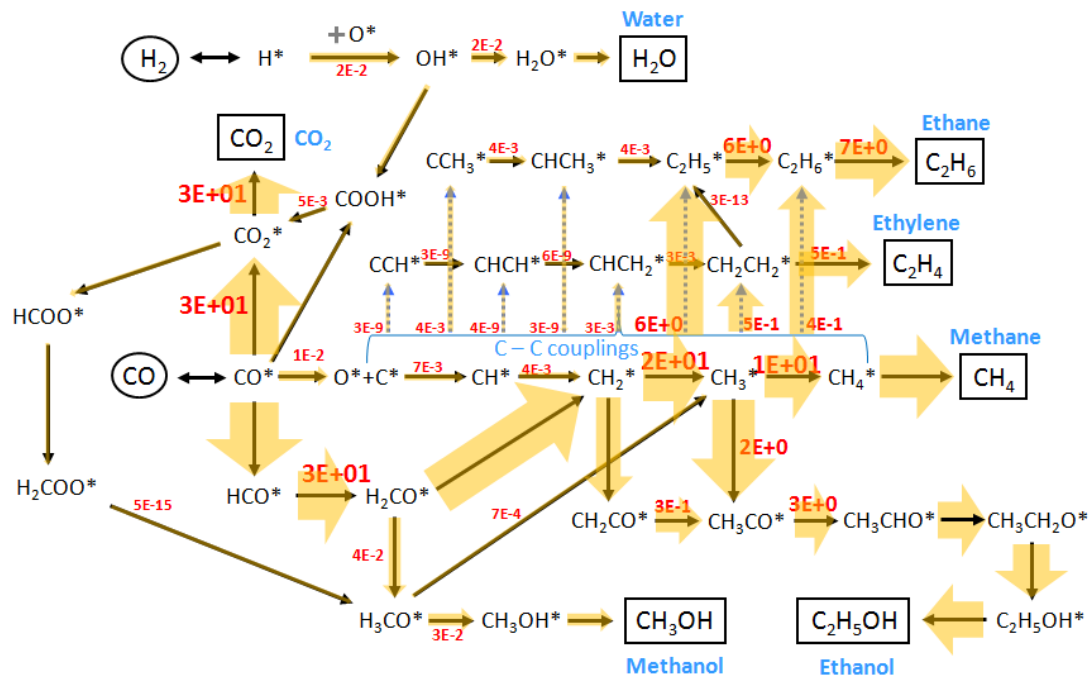


Figure 4.4. Rates of elementary steps in the reaction network at steady state. Gas phase reactants (products) are shown in circles (rectangles).

CH₂* is found to be a major intermediate produced from H-assisted CO dissociation. CH₂* can be coupled with other CH_x* intermediates to produce C₂ hydrocarbons. Our results show that C₂ hydrocarbons are mainly produced from coupling of CH₂*+CH₃* or CH₃*+CH₃*, rather than couplings of CH_x species with lower hydrogen content such as CH*+CH*. Finally, for ethanol synthesis, our results showed that CO insertion mechanism through CH₃* is the primary reaction pathway while CO insertion through CH₂* also plays an important role.

4.3.6.5 Sensitivity analysis - production rate

The previous section has qualitatively discussed the dominant reaction pathways in our network. This eliminates a large number of steps from consideration as the events that control the catalyst performance. To further determine which elementary steps in these pathways are the most kinetically rate-limiting, we performed a sensitivity analysis on our reaction network. This approach was introduced by Campbell under the name “degree of rate control” analysis.^{104,105} The basic idea is to increase/decrease the rate constant of a step by a small amount and calculate the resulting fractional change in the overall rate. The step whose increase/decrease leads to the greatest increase/decrease in the overall rate is then considered the most rate-controlling. Campbell defined the degree of rate control by

$$X_{rc,i} = \left(\frac{k_i}{r}\right)\left(\frac{\delta r}{\delta k_i}\right) \quad (4.16)$$

where, $X_{rc,i}$ is the degree of rate control of step i , k_i is the rate constant of step i ; r is the reaction rate of targeted product; δr and δk_i are the differential changes of corresponding reaction rate and rate constant.

As our model was solved by numerical methods, the disturbance introduced in sensitivity analysis δk_i , should be small enough to make a small impact on the model results, while large enough to be differentiated from numerical uncertainty in our calculations. We used $\frac{\delta k_i}{k_i} = 1\%$, 3%, 5%, 8%, and 10% and tested their performance for a small group of elementary steps. We found that 1% was too small, while 10% was too large. All results below were calculated using $\frac{\delta k_i}{k_i} = 5\%$ for the degree of rate control, as summarized in Table 4.7.

Table 4.7. Degrees of rate control for selected steps under reaction condition at 573 K, 30 bar of syngas with $\text{CO}/\text{H}_2 = 1:1$.

	CH ₄	CO ₂	C ₂ H ₆	C ₂ H ₅ OH
CH ₂ * + H* → CH ₃ * + *	0.46	0.03	-0.10	0.14
CH ₃ * + H* → CH ₄ * + *	0.59	0.05	-0.34	-0.34
CO* + H* → HCO* + *	0.24	0.02	0.38	0.97
CO* + O* → CO ₂ * + *	0.08	0.94	-0.25	-0.64
CH ₃ * + CO* → CH ₃ CO* + *	-0.15	-0.06	-0.14	0.74
CH ₂ * + CH ₃ * → CH ₂ CH ₃ * + *	-0.35	0.03	0.44	-0.32

Weak inhibiting step
(-0.7 < value < -0.4)

Weak promoting step
(0.4 < value < 0.7)

Strong promoting step
(value > 0.7)

All the other 47 elementary steps have Degree of rate control smaller in magnitude than 0.05.

By definition of the degree of rate control, steps with a positive degree of rate control indicate the targeted production rate is promoted by these steps, while a negative degree of rate control mean the targeted production rate is inhibited by these steps. Also, the larger the absolute value of the degree of rate control, the more rate-controlling the step is. Thus, by performing degree of rate control analysis, we quantitatively identified which steps are rate-controlling. In Table 4.7, we listed elementary steps having degrees of rate control larger than 0.4 for the production of CH₄, CO₂, C₂H₆ and C₂H₅OH. Of the 53 elementary steps in the network, only 6 of them are rate limiting. Specifically, for

ethanol production, hydrogenation of CO* is found to be the strongest promoting step. Oxidation of CO* is the strongest inhibiting step for ethanol production but the strongest promoting step for making CO₂. These findings suggested that reactions involving CO* as the starting point of the reaction network greatly influence the overall activity of syngas reactions. Whether adsorbed CO is hydrogenated or oxidized directly correlates with production of alcohols and CO₂ respectively. Similarly to CO*, CH₃* is another important splitting point for producing ethane and ethanol. As a promoting step for making ethane, CH₂*+CH₃* is found to be the dominant step for C-C coupling, among 8 distinct CH_x-CH_y coupling steps in the network. On the other hand, CH₃*+CO* is a strong promoting step for making ethanol. Finally, CH₃*+H* and CH₂*+H* are the strongest two promoting steps for methane production.

4.3.6.6 Sensitivity analysis - selectivity

From previous section, we successfully determined 6 elementary steps controlling production rates in syngas reactions. However, as discussed earlier, we are primarily interested in characterizing the steps that control the reaction selectivity. Therefore, we further applied sensitivity analysis to the reaction selectivity. Similar to the idea of degree of rate control used in previous section, we define the degree of selectivity control as

$$Y_{sc,i} = \left(\frac{k_i}{s}\right)\left(\frac{\delta s}{\delta k_i}\right) \quad (4.17)$$

where $Y_{sc,i}$ is the degree of selectivity control of step i , k_i is the rate constant of step i ; s is the reaction selectivity of targeted product; δs and δk_i are differential changes of corresponding reaction selectivity and rate constant. In other words, every quantity is defined in the same way as in Eqn. 4.16 except the reaction rate is replaced by the reaction selectivity.

Table 4.8. Degrees of selectivity control for selected steps under reaction condition at 573 K, 30 bar of syngas with CO/H₂ = 1:1.

	CH ₄	CO ₂	C ₂ H ₆	C ₂ H ₅ OH	
CH ₃ * + H* → CH ₄ * + *	0.56	0.02	-0.38	-0.37	Strong inhibiting step (value <-0.7)
CO* + H* → HCO* + *	-0.11	-0.33	0.03	0.62	Weak inhibiting step (-0.7<value<-0.4)
CO* + O* → CO ₂ * + *	-0.20	0.65	-0.53	-0.92	Weak promoting step (0.4<value<0.7)
CH ₃ * + CO* → CH ₃ CO* + *	-0.13	-0.04	-0.12	0.76	Strong promoting step (value > 0.7)
CH ₂ *+CH ₃ * → CH ₂ CH ₃ * + *	-0.36	0.02	0.43	-0.33	

All the other 48 elementary steps have Degree of selectivity control smaller in magnitude than 0.05.

The results of degree of selectivity control are shown in Table 4.8. Comparing to the results in Table 4.7, most of the rate determining steps are also the selectivity determining steps. However, the meanings behind selectivity determining and rate determining are not entirely the same. One elementary step may promote the production of a product while inhibit its selectivity because it promotes the production of other competing products even more. For example, as shown in Table 4.7, CO hydrogenation turned out to increase the rates of all 4 products, while in Table 4.8, it actually inhibited selectivities of methane and CO₂. The hydrogenation of CH₃* is the strongest promoting step for CH₄ selectivity while it has negative impacts on the selectivities for C₂H₆ and C₂H₅OH. This is reasonable since they share CH₃* as an important reaction intermediate, where more CH₃* going towards CH₄* will result in less of them being produced as C₂ species. Similarly, CO hydrogenation (CO*+H*) and CO oxidation (CO*+O*) are also competing steps in the reaction network. The former step promotes C₂H₅OH selectivity and inhibits CO₂ selectivity while the latter enhances CO₂ production and impedes all the other productions. These selectivity determining steps are illustrated in Fig. 4.5. As seen below, within the main reaction mechanism shown in Fig. 4.4, in general the elementary steps at the intersections are important in determining the reaction selectivity.

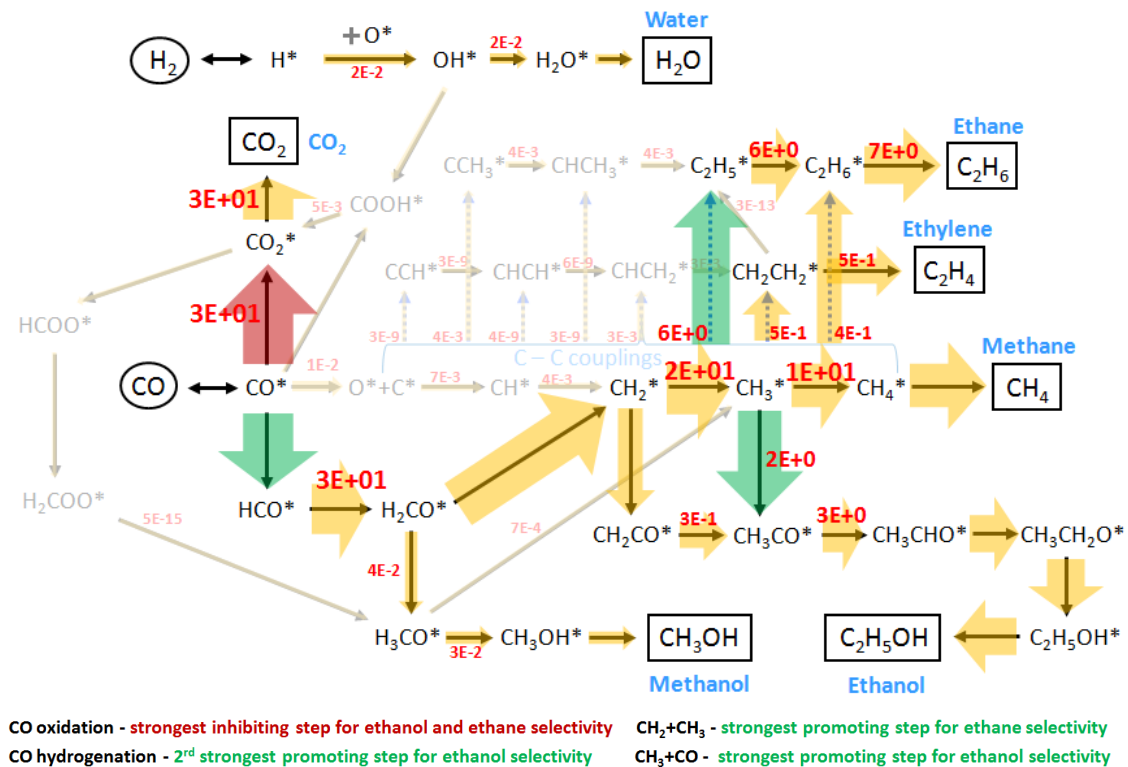


Figure 4.5. Important selectivity determining steps within the main reaction mechanism illustrated in Fig. 4.4

Another interesting finding is the selectivity controlling step of ethanol. CO insertion ($\text{CH}_3^* + \text{CO}^*$) turned out to be the strongest promoting step for ethanol selectivity, as well as the only step that promotes ethanol production while inhibits ethane production. This suggested a possible explanation for selectivity shift from hydrocarbons to alcohols on alkali promoted Mo_2C catalysts observed experimentally. Our results implied that CO insertion could be promoted by alkali promoter and thus the overall selectivity is shifted from hydrocarbons to alcohols.

4.3.6.7 Model robustness analysis over BEP relation

As mentioned earlier, our model applied a BEP relation to approximate the activation energy for all surface elementary steps. It is useful to ask how accurate the BEP relation is and whether this affects the validity of our conclusion. As the BEP

relation is by definition an approximation without considering how reactions take place at a detailed level, a certain margin of error in this approximation is expected. Since the motivation of this work is to identify rate/selectivity controlling steps in a complex network, We aimed to understand the impact of the BEP relation on these steps.

To examine the robustness of this model against error, we deliberately manipulate both slope and intercept terms of the BEP relation, and repeated all the procedures to calculate the degree of selectivity control. Specifically, we introduced errors to the slope and intercept terms in Eqn. 4.3, 4.4 and 4.5, at levels of $\pm 5\%$, $\pm 10\%$, and $\pm 15\%$, as follows:

$$E_a = \alpha \cdot (1+x) \cdot \Delta H + E_0 \cdot (1+y) \quad (4.18)$$

$x, y = \pm 5\%, \pm 10\%, \pm 15\%, |x| + |y| \ll 15\%$

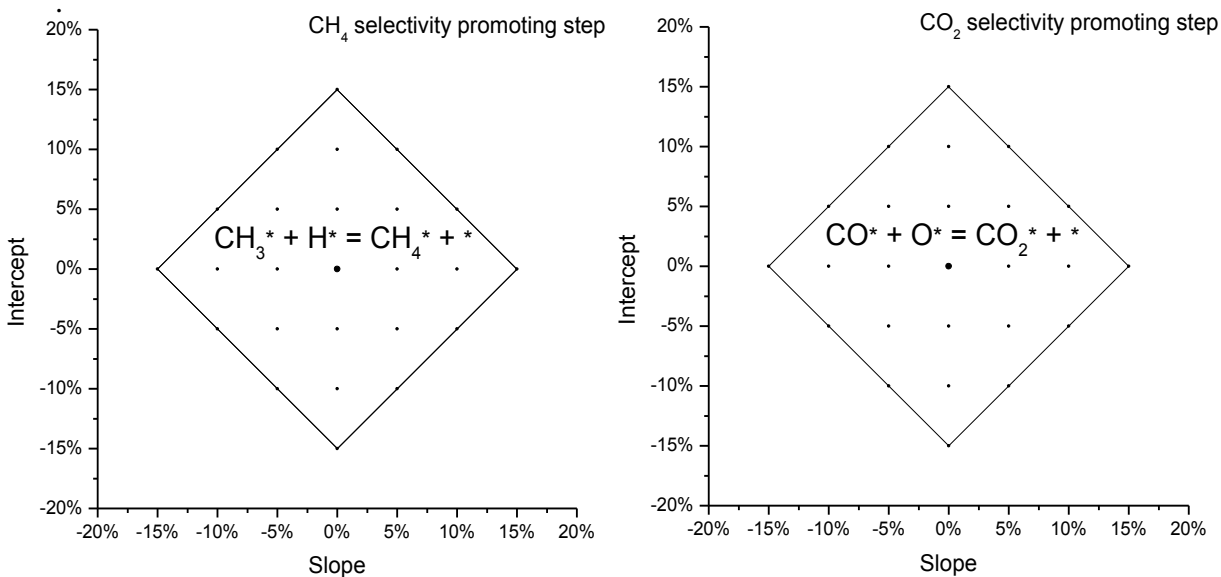


Figure 4.6. Selectivity promoting steps for CH_4 and CO_2 at different levels of error on the slope and intercept terms in the BEP relation. The solid lines indicate the range of errors analyzed.

In Fig. 4.6, the selectivity promoting step for CH₄ was shown for the range of conditions we analyzed. CH₃*+H* was found to be the only selectivity promoting step over the whole range of conditions. This is an encouraging result, suggesting that a quantitative uncertainty in a BEP relation may not influence qualitatively identifying the selectivity determining step of a reaction. Similarly, for CO₂ selectivity, CO*+O* remains to be the strongest promoting step as determined in Table 4.8. On the other hand, the selectivity determining steps for ethane and ethanol are more complicated. In Fig. 4.7, the strongest promoting and inhibiting steps for the ethane selectivity was illustrated. Although CO*+O* is still the strongest inhibiting step for all conditions we examined, with an overestimated intercept term and an underestimated slope term in the BEP relation, C₂H₅*+H* became the strongest promoting step for ethane selectivity. In other situations, CH₃*+CH₂* is the strongest promoting step. In Fig. 4.8, similar results were obtained for ethanol case, where three elementary steps: CO hydrogenation (CO*+H*), CO insertion (CO*+CH₃*) and C₂H₅O hydrogenation (C₂H₅O*+H*) could be the strongest selectivity promoting step based on the error associated with the BEP relation. These results suggest that our conclusions in previous section could be influenced by the errors in the BEP relation to some extent. Nevertheless, this analysis still narrows the list of possible selectivity determining steps to a few elementary steps.

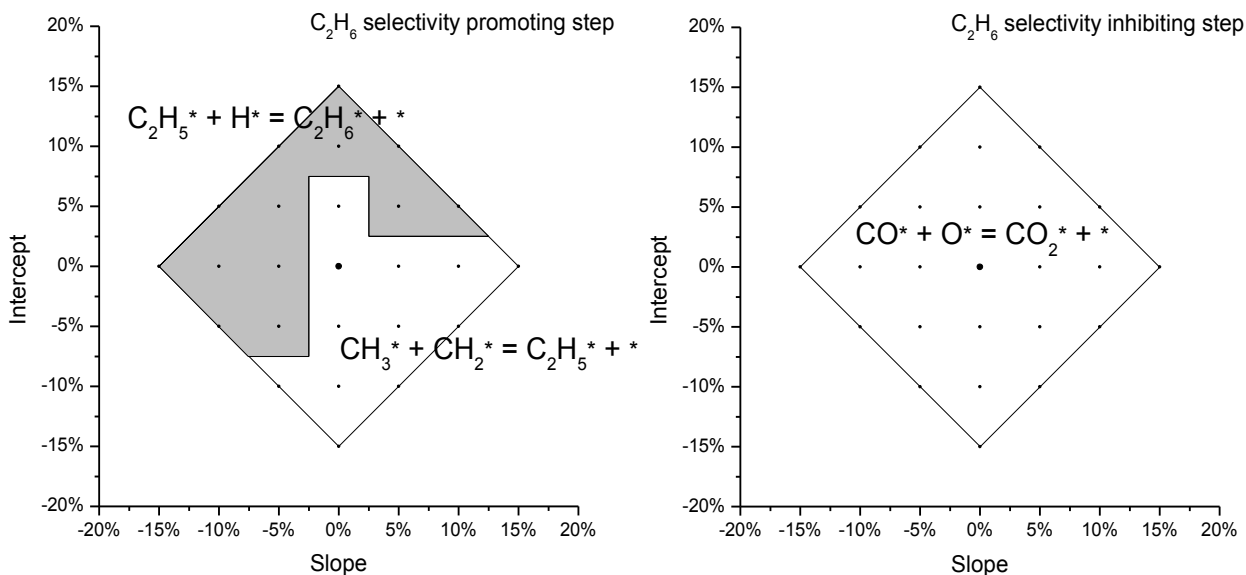


Figure 4.7. Selectivity promoting and inhibiting steps for ethane at different levels of error on the slope and intercept terms in the BEP relation. The solid lines indicate the range of errors analyzed.

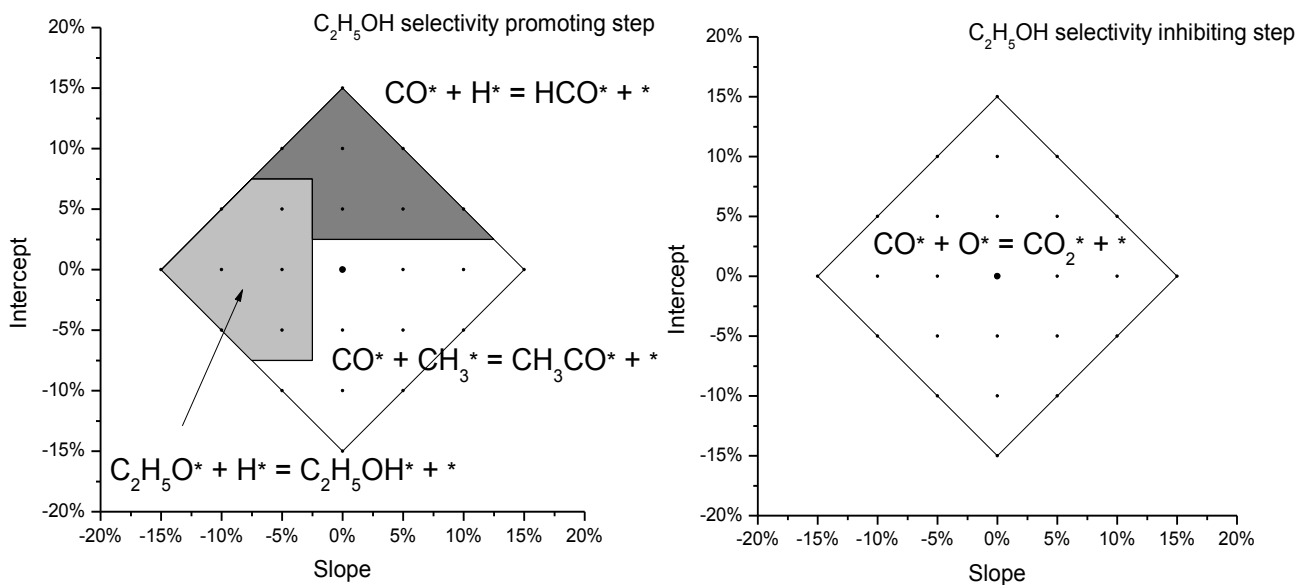


Figure 4.8. Selectivity promoting and inhibiting steps for ethanol at different levels of error on the slope and intercept terms in the BEP relation. The solid lines indicate the range of errors analyzed.

4.4 Conclusions

This chapter provides a useful example of screening selectivity-determining elementary steps in a complex reaction network for a heterogeneous catalyst. Our model mainly employs energy inputs from DFT calculations. DFT computed adsorption energy for gaseous products were corrected by TPD results. Activation energies for surface reactions were approximated from a BEP relation. To consider interactions between surface intermediates, we applied the quasi-chemical approximation to calculate contribution from nearest neighbored adsorbates while keeping the whole approximation in closed equation form. Further, kinetic theory and transition state theory were used to derive the rate equations and the whole equation set was numerically solved without imposing any assumptions on the reaction mechanism. To validate our methodology, our computed selectivities were compared with experimental selectivities at various temperatures and pressures, where excellent agreement was reached. Finally, sensitivity analysis was performed to determine individual elementary step's contribution to the overall selectivity. We are able to conclude with very few steps that are selectivity-determining. As a long term goal, these steps can be used as descriptors and could potentially help the rational design of catalysts selective to specific products.

In terms of mechanistic insights into syngas reactions on Mo₂C catalysts, our results suggested that H-assisted CO dissociation was dominant over the direct CO dissociation on Mo₂C under the experimental conditions we used. Within a reaction network including 53 elementary steps, only 5 steps are controlling the selectivities of CH₄, CO₂, C₂H₆ and C₂H₅OH. CO oxidation (CO*+O*) was found to be the strongest inhibiting step for C₂H₆ and C₂H₅OH selectivity. CO insertion (CO*+CH₃*) and CO

hydrogenation ($\text{CO}^* + \text{H}^*$) are the strongest two promoting steps for $\text{C}_2\text{H}_5\text{OH}$ selectivity, while $\text{CH}_2^* + \text{CH}_3^*$ was suggested to be the strongest selectivity promoting step for C_2H_6 production. As the only step promoting ethanol selectivity while inhibiting ethane selectivity, CO insertion could be potentially responsible for the selectivity shift from hydrocarbons to alcohols upon addition of alkali promoters observed in experiments.

Although the conclusions above are specifically drawn for a Mo_2C catalyst, some of them can be generalized and potentially helpful to understand syngas reactions on other types of catalysts. Firstly, investigating product selectivity of syngas reactions is a complex problem and it requires developing a reaction network to consider all the relevant reactions. For example, Fischer Tropsch synthesis, methanol synthesis, alcohol synthesis and water gas shift chemistry should be all included. Secondly, elementary steps controlling the production rate and selectivity are generally the slowest steps in the fastest reaction pathways. This raises the complication that sometimes an elementary step may be fast enough to create a dominant reaction pathway while too fast to be the controlling step of it. For instance, H-assisted CO hydrogenation turned out to be critical since it provided a faster pathway to break C-O bond than direct CO dissociation. However, our results suggested it is not a rate-controlling step because it is not the slowest step in the overall H-assisted CO dissociation pathway. Finally, steps where the reaction network splits into different products are important to product selectivity and thus should be closely examined. As shown in this chapter, reactions involving CO^* play an important role as whether CO^* is oxidized, hydrogenated directly influences selectivity of CO_2 and hydrocarbons. Similarly, CH_3^* is another vital reaction

intermediate since it reacts with CO^* , H^* or CH_2^* and therefore could potentially determine overall selectivities towards ethanol, methane and ethane.

4.5 References

- (1) Huber, G. W.; Iborra, S.; Corma, A. *Chemical Reviews* **2006**, *106*, 4044.
- (2) Lynd, L. R. *Annual Review of Energy and the Environment* **1996**, *21*, 403.
- (3) Iglesia, E.; Reyes, S. C.; Madon, R. J.; Soled, S. L. *Advances in Catalysis, Vol 39* **1993**, *39*, 221.
- (4) Khodakov, A. Y.; Chu, W.; Fongarland, P. *Chemical Reviews* **2007**, *107*, 1692.
- (5) Ponec, V. *Catal. Rev.-Sci. Eng.* **1978**, *18*, 151.
- (6) Spivey, J. J.; Egbebi, A. *Chem. Soc. Rev.* **2007**, *36*, 1514.
- (7) Subramani, V.; Gangwal, S. K. *Energy Fuels* **2008**, *22*, 814.
- (8) Van der Laan, G. P.; Beenackers, A. *Catal. Rev.-Sci. Eng.* **1999**, *41*, 255.
- (9) Vanderlee, G.; Ponec, V. *Catal. Rev.-Sci. Eng.* **1987**, *29*, 183.
- (10) Oshikawa, K.; Nagai, M.; Omi, S. *J. Phys. Chem. B* **2001**, *105*, 9124.
- (11) Claridge, J. B.; York, A. P. E.; Brungs, A. J.; Marquez-Alvarez, C.; Sloan, J.; Tsang, S. C.; Green, M. L. H. *Journal of Catalysis* **1998**, *180*, 85.
- (12) Barthos, R.; Solymosi, F. *Journal of Catalysis* **2007**, *249*, 289.
- (13) Kojima, I.; Miyazaki, E.; Yasumori, I. *J. Chem. Soc.-Chem. Commun.* **1980**, 573.
- (14) Oyama, S. T. *Catalysis Today* **1992**, *15*, 179.
- (15) Park, K. Y.; Seo, W. K.; Lee, J. S. *Catalysis Letters* **1991**, *11*, 349.
- (16) Vo, D. V. N.; Adesina, A. A. *Appl. Catal. A-Gen.* **2011**, *399*, 221.
- (17) Griboval-Constant, A.; Giraudon, J. M.; Leclercq, G.; Leclercq, L. *Appl. Catal. A-Gen.* **2004**, *260*, 35.
- (18) Patt, J.; Moon, D. J.; Phillips, C.; Thompson, L. *Catalysis Letters* **2000**, *65*, 193.
- (19) Moon, D. J.; Ryu, J. W. *Catalysis Letters* **2004**, *92*, 17.
- (20) Nagai, M.; Matsuda, K. *Journal of Catalysis* **2006**, *238*, 489.

- (21) Woo, H. C.; Park, K. Y.; Kim, Y. G.; Nam, I. S.; Chung, J. S.; Lee, J. S. *Applied Catalysis* **1991**, *75*, 267.
- (22) Xiang, M. L.; Li, D. B.; Li, W. H.; Zhong, B.; Sun, Y. H. *Fuel* **2006**, *85*, 2662.
- (23) Shou, H.; Davis, R. J. *Journal of Catalysis* **2011**, *282*, 83.
- (24) Shou, H.; Li, L.; Ferrari, D.; Sholl, D. S.; Davis, R. J. *Journal of Catalysis* **2013**, *299*, 150.
- (25) Kitchin, J. R.; Norskov, J. K.; Barteau, M. A.; Chen, J. G. G. *Catalysis Today* **2005**, *105*, 66.
- (26) Han, J. W.; Li, L.; Sholl, D. S. *The Journal of Physical Chemistry C* **2011**, *115*, 6870.
- (27) Pistonesi, C.; Juan, A.; Farkas, A. P.; Solymosi, F. *Surface Science* **2008**, *602*, 2206.
- (28) Ren, J.; Huo, C. F.; Wang, J. G.; Li, Y. W.; Jiao, H. J. *Surface Science* **2005**, *596*, 212.
- (29) Shi, X. R.; Wang, S. G.; Wang, H.; Deng, C. M.; Qin, Z. F.; Wang, J. G. *Surface Science* **2009**, *603*, 852.
- (30) Hugosson, H. W.; Eriksson, O.; Nordstrom, L.; Jansson, U.; Fast, L.; Delin, A.; Wills, J. M.; Johansson, B. *Journal of Applied Physics* **1999**, *86*, 3758.
- (31) Wang, T.; Liu, X. W.; Wang, S. G.; Huo, C. F.; Li, Y. W.; Wang, J. G.; Jiao, H. J. *Journal of Physical Chemistry C* **2011**, *115*, 22360.
- (32) Shi, X.-R.; Wang, J.; Hermann, K. *The Journal of Physical Chemistry C* **2010**, *114*, 13630.
- (33) Tominaga, H.; Nagai, M. *J. Phys. Chem. B* **2005**, *109*, 20415.
- (34) Tominaga, H.; Nagai, M. *Appl. Catal. A-Gen.* **2005**, *282*, 5.
- (35) Vojvodic, A. *Catalysis Letters* **2012**, *142*, 728.
- (36) Medford, A. J.; Vojvodic, A.; Studt, F.; Abild-Pedersen, F.; Norskov, J. K. *Journal of Catalysis* **2012**, *290*, 108.
- (37) Pistonesi, C.; Proncato, M. E.; Bugyi, L.; Juan, A. *Journal of Physical Chemistry C* **2012**, *116*, 24573.
- (38) Tominaga, H.; Aoki, Y.; Nagai, M. *Appl. Catal. A-Gen.* **2012**, *423*, 192.

- (39) Kresse, G.; Furthmuller, J. *Phys. Rev. B* **1996**, *54*, 11169.
- (40) Kresse, G.; Hafner, J. *Phys. Rev. B* **1993**, *47*, 558.
- (41) Kresse, G.; Hafner, J. *J. Phys.: Condens. Matter* **1994**, *6*, 8245.
- (42) Sholl, D. S.; Steckel, J. A. *Density functional theory : a practical introduction*; John Wiley & Sons, Inc.: Hoboken, NJ, 2009.
- (43) Perdew, J. P.; Burke, K.; Ernzerhof, M. *Phys. Rev. Lett.* **1996**, *77*, 3865.
- (44) Perdew, J. P.; Burke, K.; Ernzerhof, M. *Phys. Rev. Lett.* **1997**, *78*, 1396.
- (45) Blöchl, P. E. *Phys. Rev. B* **1994**, *50*, 17953.
- (46) Kresse, G.; Joubert, D. *Phys. Rev. B* **1999**, *59*, 1758.
- (47) Bengtsson, L. *Physical Review B* **1999**, *59*, 12301.
- (48) Neugebauer, J.; Scheffler, M. *Physical Review B* **1992**, *46*, 16067.
- (49) Lo, R. L.; Fukui, K.; Otani, S.; Iwasawa, Y. *Surface Science* **1999**, *440*, L857.
- (50) Lo, R. L.; Fukui, K.; Otani, S.; Oyama, S. T.; Iwasawa, Y. *Japanese Journal of Applied Physics Part 1-Regular Papers Short Notes & Review Papers* **1999**, *38*, 3813.
- (51) Newsome, D. S. *Catal. Rev.-Sci. Eng.* **1980**, *21*, 275.
- (52) Ratnasamy, C.; Wagner, J. P. *Catal. Rev.-Sci. Eng.* **2009**, *51*, 325.
- (53) Rhodes, C.; Hutchings, G. J.; Ward, A. M. *Catalysis Today* **1995**, *23*, 43.
- (54) Chinchin, G. C.; Denny, P. J.; Jennings, J. R.; Spencer, M. S.; Waugh, K. C. *Applied Catalysis* **1988**, *36*, 1.
- (55) Klier, K. *Advances in Catalysis* **1982**, *31*, 243.
- (56) Liu, X. M.; Lu, G. Q.; Yan, Z. F.; Beltramini, J. *Ind. Eng. Chem. Res.* **2003**, *42*, 6518.
- (57) Forzatti, P.; Tronconi, E.; Pasquon, I. *Catal. Rev.-Sci. Eng.* **1991**, *33*, 109.
- (58) Cheng, J.; Gong, X. Q.; Hu, P.; Lok, C. M.; Ellis, P.; French, S. *Journal of Catalysis* **2008**, *254*, 285.

- (59) Cheng, J.; Hu, P.; Ellis, P.; French, S.; Kelly, G.; Lok, C. M. *Journal of Physical Chemistry C* **2008**, *112*, 9464.
- (60) Cheng, J.; Hu, P.; Ellis, P.; French, S.; Kelly, G.; Lok, C. M. *Journal of Physical Chemistry C* **2008**, *112*, 6082.
- (61) Cheng, J.; Hu, P.; Ellis, P.; French, S.; Kelly, G.; Lok, C. M. *Journal of Catalysis* **2008**, *257*, 221.
- (62) Cheng, J.; Hu, P.; Ellis, P.; French, S.; Kelly, G.; Lok, C. M. *Top. Catal.* **2010**, *53*, 326.
- (63) Choi, Y.; Liu, P. *J. Am. Chem. Soc.* **2009**, *131*, 13054.
- (64) Grabow, L. C.; Mavrikakis, M. *ACS Catalysis* **2011**, *1*, 365.
- (65) Gokhale, A. A.; Dumesic, J. A.; Mavrikakis, M. *J. Am. Chem. Soc.* **2008**, *130*, 1402.
- (66) Madon, R. J.; Braden, D.; Kandoi, S.; Nagel, P.; Mavrikakis, M.; Dumesic, J. A. *Journal of Catalysis* **2011**, *281*, 1.
- (67) Grabow, L. C.; Gokhale, A. A.; Evans, S. T.; Dumesic, J. A.; Mavrikakis, M. *Journal of Physical Chemistry C* **2008**, *112*, 4608.
- (68) Ferrin, P.; Simonetti, D.; Kandoi, S.; Kunkes, E.; Dumesic, J. A.; Norskov, J. K.; Mavrikakis, M. *J. Am. Chem. Soc.* **2009**, *131*, 5809.
- (69) Mei, D.; Rousseau, R.; Kathmann, S. M.; Glezakou, V.-A.; Engelhard, M. H.; Jiang, W.; Wang, C.; Gerber, M. A.; White, J. F.; Stevens, D. J. *Journal of Catalysis* **2010**, *271*, 325.
- (70) Fischer, F.; Tropsch, H. *Berichte Der Deutschen Chemischen Gesellschaft* **1926**, *59*, 830.
- (71) Ponec, V. *Catalysis Today* **1992**, *12*, 227.
- (72) Orita, H.; Naito, S.; Tamaru, K. *Journal of Catalysis* **1984**, *90*, 183.
- (73) Chinchin, G. C.; Denny, P. J.; Parker, D. G.; Spencer, M. S.; Whan, D. A. *Applied Catalysis* **1987**, *30*, 333.
- (74) Waugh, K. C. *Catalysis Today* **1992**, *15*, 51.
- (75) Rasmussen, P. B.; Kazuta, M.; Chorkendorff, I. *Surface Science* **1994**, *318*, 267.

- (76) Rasmussen, P. B.; Holmblad, P. M.; Askgaard, T.; Ovesen, C. V.; Stoltze, P.; Norskov, J. K.; Chorkendorff, I. *Catalysis Letters* **1994**, *26*, 373.
- (77) Koryabkina, N. A.; Phatak, A. A.; Ruettinger, W. F.; Farrauto, R. J.; Ribeiro, F. H. *Journal of Catalysis* **2003**, *217*, 233.
- (78) Ovesen, C. V.; Clausen, B. S.; Hammershoi, B. S.; Steffensen, G.; Askgaard, T.; Chorkendorff, I.; Norskov, J. K.; Rasmussen, P. B.; Stoltze, P.; Taylor, P. *Journal of Catalysis* **1996**, *158*, 170.
- (79) Ovesen, C. V.; Stoltze, P.; Norskov, J. K.; Campbell, C. T. *Journal of Catalysis* **1992**, *134*, 445.
- (80) Shou, H.; Ferrari, D.; Barton, D. G.; Jones, C. W.; Davis, R. J. *ACS Catalysis* **2012**, *2*, 1408.
- (81) Hammer, B.; Hansen, L. B.; Norskov, J. K. *Physical Review B* **1999**, *59*, 7413.
- (82) Redhead, P. A. *Vacuum* **1962**, *12*, 203.
- (83) Bugyi, L.; Solymosi, F. *J. Phys. Chem. B* **2001**, *105*, 4337.
- (84) Michaelides, A.; Liu, Z. P.; Zhang, C. J.; Alavi, A.; King, D. A.; Hu, P. *J. Am. Chem. Soc.* **2003**, *125*, 3704.
- (85) Sutton, J. E.; Vlachos, D. G. *ACS Catalysis* **2012**, *2*, 1624.
- (86) van Santen, R. A.; Neurock, M.; Shetty, S. G. *Chemical Reviews* **2010**, *110*, 2005.
- (87) Wang, S. G.; Temel, B.; Shen, J. A.; Jones, G.; Grabow, L. C.; Studt, F.; Bligaard, T.; Abild-Pedersen, F.; Christensen, C. H.; Norskov, J. K. *Catalysis Letters* **2011**, *141*, 370.
- (88) Reuter, K.; Scheffler, M. *Physical Review B* **2006**, *73*.
- (89) Datar, A. S.; Prasad, S. D. *Langmuir* **1991**, *7*, 1310.
- (90) King, D. A.; Wells, M. G. *Proceedings of the Royal Society of London Series a-Mathematical Physical and Engineering Sciences* **1974**, *339*, 245.
- (91) Fowler, R. H.; Guggenheim, E. A. *Statistical Thermodynamics*; Cambridge University Press: London, 1965.
- (92) Vannice, M. A. *Kinetics of Catalytic Reactions*; 1st ed.; Springer: New York, 2005.

- (93) Bouchy, C.; Pham-Huu, C.; Heinrich, B.; Chaumont, C.; Ledoux, M. J. *Journal of Catalysis* **2000**, *190*, 92.
- (94) Delporte, P.; Meunier, F.; Phamhuu, C.; Vennegues, P.; Ledoux, M. J.; Guille, J. *Catalysis Today* **1995**, *23*, 251.
- (95) Edamoto, K.; Sugihara, M.; Ozawa, K.; Otani, S. *Surface Science* **2004**, *561*, 101.
- (96) Liu, P.; Rodriguez, J. A. *J. Phys. Chem. B* **2006**, *110*, 19418.
- (97) Oyama, S. T.; Delporte, P.; PhamHuu, C.; Ledoux, M. J. *Chemistry Letters* **1997**, 949.
- (98) Wu, W. C.; Wu, Z. L.; Liang, C. H.; Chen, X. W.; Ying, P. L.; Li, C. *J. Phys. Chem. B* **2003**, *107*, 7088.
- (99) Zaman, S.; Smith, K. J. *Catal. Rev.-Sci. Eng.* **2012**, *54*, 41.
- (100) Bell, A. T. *Catal. Rev.-Sci. Eng.* **1981**, *23*, 203.
- (101) Ojeda, M.; Nabar, R.; Nilekar, A. U.; Ishikawa, A.; Mavrikakis, M.; Iglesia, E. *Journal of Catalysis* **2010**, *272*, 287.
- (102) Huo, C.-F.; Ren, J.; Li, Y.-W.; Wang, J.; Jiao, H. *Journal of Catalysis* **2007**, *249*, 174.
- (103) Andersson, M. P.; Abild-Pedersen, E.; Remediakis, I. N.; Bligaard, T.; Jones, G.; Engbkw, J.; Lytken, O.; Horch, S.; Nielsen, J. H.; Sehested, J.; Rostrup-Nielsen, J. R.; Norskov, J. K.; Chorkendorff, I. *Journal of Catalysis* **2008**, *255*, 6.
- (104) Campbell, C. T. *Top. Catal.* **1994**, *1*, 353.
- (105) Campbell, C. T. *Journal of Catalysis* **2001**, *204*, 520.

APPENDIX 4.A

ADSORPTION GEOMETRY OF SYNGAS REACTION

INTERMEDIATES ON RECONSTRUCTED Mo_2C (001) SURFACE

This appendix lists the structure information for the most stable geometries of syngas reaction intermediates adsorbed on reconstructed bare Mo_2C (001) surfaces discussed in this chapter. The coordinates for each surface are defined for a single supercell of a (1×1) surface unit cell with all coordinates in Å. A table defining unit cell vectors for supercell is also listed in Å. The adsorption sites information and geometries are listed below.

Table 4.A.1: Unit cell vectors for a (1×1) surface used in this chapter. (in Å)

	x	y	z
a	5.268	3.036	0.000
b	0.000	6.072	0.000
c	0.000	0.000	22.296

Table 4.A.2: Fractional coordinates for a (1 × 1) reconstructed bare Mo₂C (001) surface.

No.	Atom	x	y	z
1	Mo	0.125397	0.187303	0.361401
2	Mo	0.196846	0.651581	0.375069
3	Mo	0.687340	0.161500	0.372538
4	Mo	0.687340	0.651165	0.372538
5	Mo	-0.008513	0.008050	0.264783
6	Mo	-0.008512	0.500460	0.264783
7	Mo	0.498880	0.000561	0.265293
8	Mo	0.481443	0.509278	0.261460
9	Mo	0.180812	0.159591	0.162283
10	Mo	0.183950	0.658022	0.162797
11	Mo	0.673698	0.162884	0.156639
12	Mo	0.673699	0.663413	0.156639
13	Mo	0.972729	0.013357	0.055492
14	Mo	0.972729	0.513904	0.055492
15	Mo	0.502734	-0.001372	0.056194
16	Mo	0.501198	0.499396	0.056033
17	C	0.520175	0.489918	0.421657
18	C	0.827817	0.836092	0.415597
19	C	0.339377	0.331324	0.319874
20	C	0.339376	0.829304	0.319873
21	C	0.829083	0.335457	0.211830
22	C	0.835798	0.832099	0.211094
23	C	0.328486	0.335579	0.104140
24	C	0.328487	0.835924	0.104139
25	C	0.837374	0.331310	0.010163
26	C	0.836798	0.831598	0.009789

Table 4.A.3: Adsorption sites of syngas reaction intermediates adsorbed on reconstructed bare Mo₂C (001) surface

No.	Species	Most stable site	Second most stable site
1	CO*	Mo top	C top
2	H*	C top	C top
3	C*	Mo-C bridge	N/A
4	O*	C top	Mo top
5	CH*	Mo-C bridge	N/A
6	CH ₂ *	C top	N/A
7	OH*	Mo top	N/A
8	CH ₃ *	C top	N/A
9	CH ₄ *	Mo top	N/A
10	HCO*	C top	N/A
11	H ₂ CO*	Mo-C bridge	N/A
12	H ₃ CO*	Mo top	N/A
13	CH ₃ OH*	Mo top	N/A
14	H ₂ O*	Mo top	N/A
15	CO ₂ *	Mo-C bridge	Mo top
16	COOH*	Mo-C bridge	N/A
17	HCOO*	Mo top	N/A
18	H ₂ COO*	Mo top	N/A
19	C ₂ H*	Mo-C bridge	N/A
20	CHCH*	Mo-C bridge	N/A
21	CCH ₃ *	Mo-C bridge	N/A
22	CH ₂ CH ₂ *	Mo-C bridge	N/A
23	C ₂ H ₅ *	C top	N/A
24	C ₂ H ₆ *	Gas phase	N/A
25	CH ₃ CO*	C top	N/A
26	CH ₃ CHO*	Gas phase	N/A
27	CH ₃ CH ₂ O*	Mo top	N/A
28	CH ₃ CH ₂ OH*	Gas phase	N/A
29	CH ₂ CO*	Mo-C bridge	N/A
30	CHCH ₂ *	Mo-C bridge	N/A
31	CHCH ₃ *	Mo-C bridge	N/A

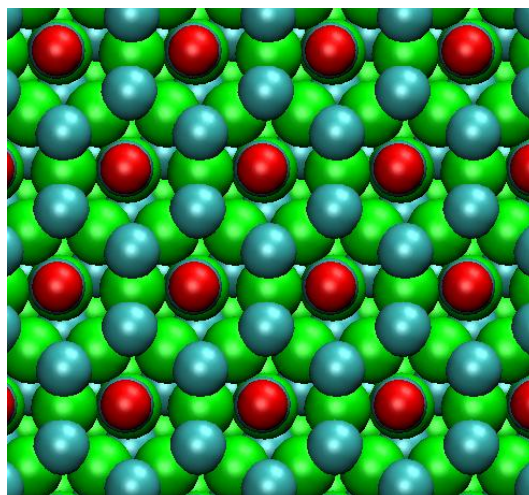


Figure 4.A.1: Adsorption geometry of CO on Mo top sites on reconstructed bare Mo₂C (001) surface. Mo, C and O atoms are depicted in green, blue and red respectively.

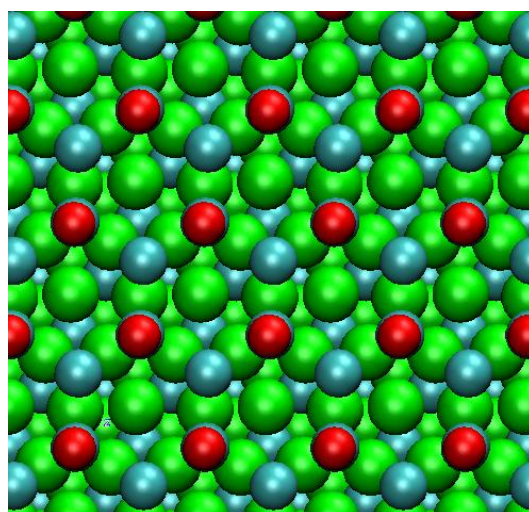


Figure 4.A.2: Adsorption geometry of CO on C top sites on reconstructed bare Mo₂C (001) surface. Mo, C and O atoms are depicted in green, blue and red respectively.

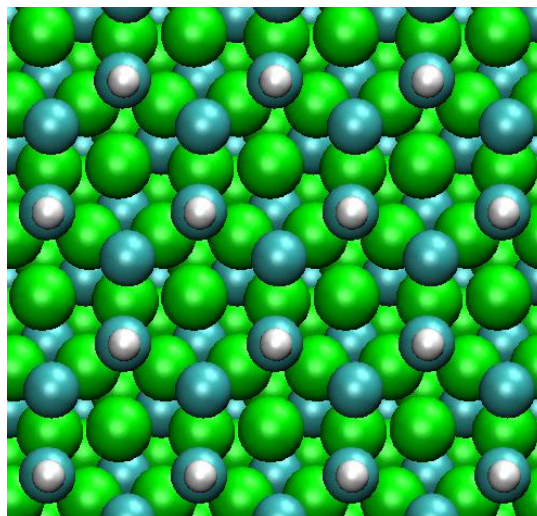


Figure 4.A.3: Adsorption geometry of H on reconstructed bare Mo₂C (001) surface. Mo, C and H atoms are depicted in green, blue and white respectively.

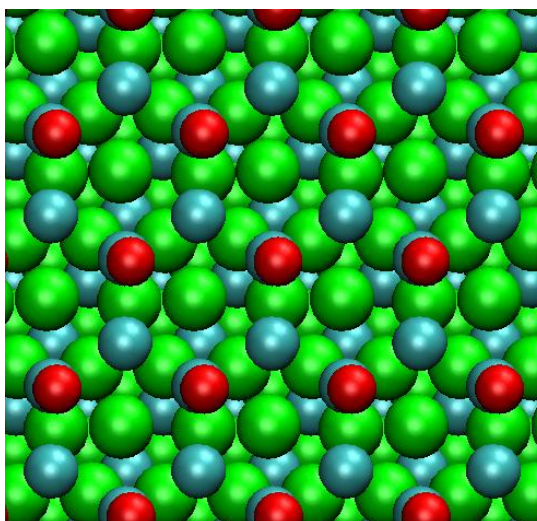


Figure 4.A.4: Adsorption geometry of O on reconstructed bare Mo₂C (001) surface. Mo, C and O atoms are depicted in green, blue and red respectively.

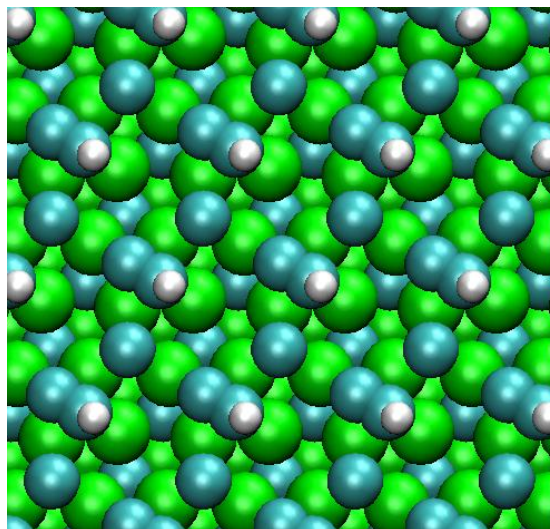


Figure 4.A.5: Adsorption geometry of CH on reconstructed bare Mo₂C (001) surface. Mo, C and H atoms are depicted in green, blue and white respectively.

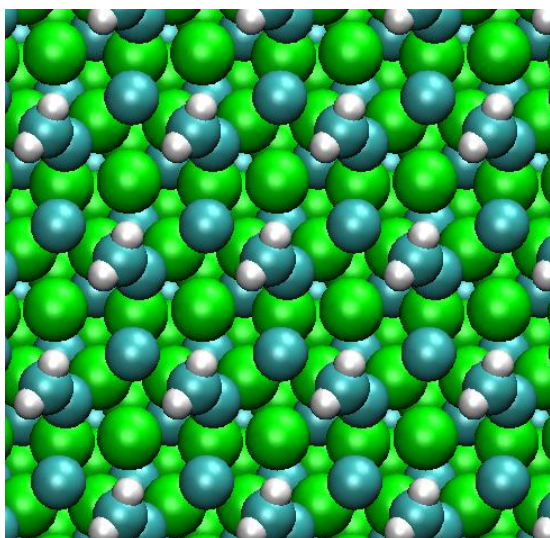


Figure 4.A.6: Adsorption geometry of CH₂ on reconstructed bare Mo₂C (001) surface. Mo, C and H atoms are depicted in green, blue and white respectively.

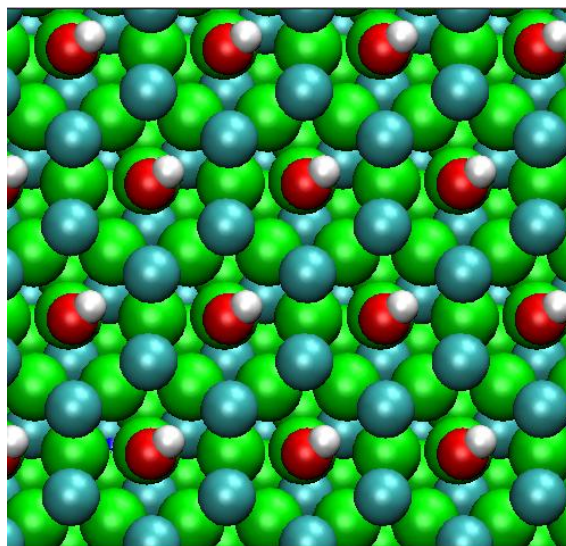


Figure 4.A.7: Adsorption geometry of OH on reconstructed bare Mo₂C (001) surface. Mo, C, O and H atoms are depicted in green, blue, red and white respectively.

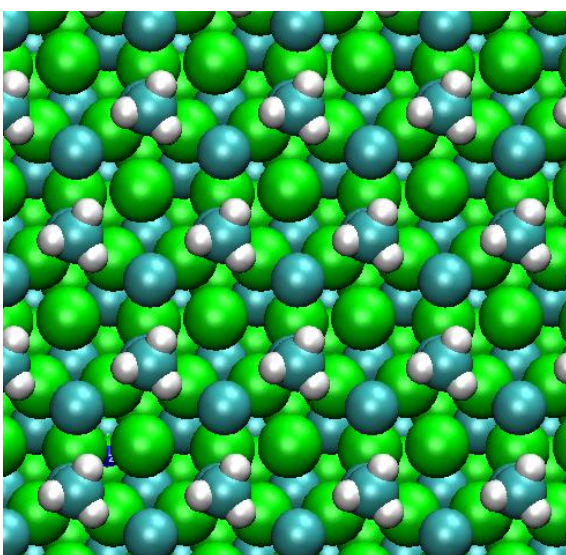


Figure 4.A.8: Adsorption geometry of CH₃ on reconstructed bare Mo₂C (001) surface. Mo, C and H atoms are depicted in green, blue and white respectively.

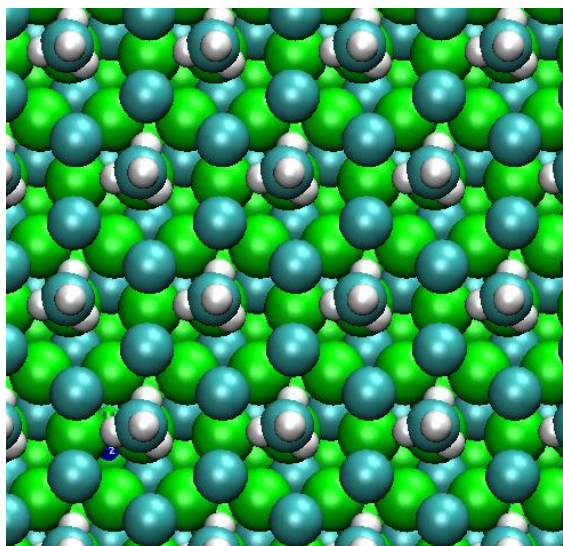


Figure 4.A.9: Adsorption geometry of CH₄ on reconstructed bare Mo₂C (001) surface. Mo, C and H atoms are depicted in green, blue and white respectively.

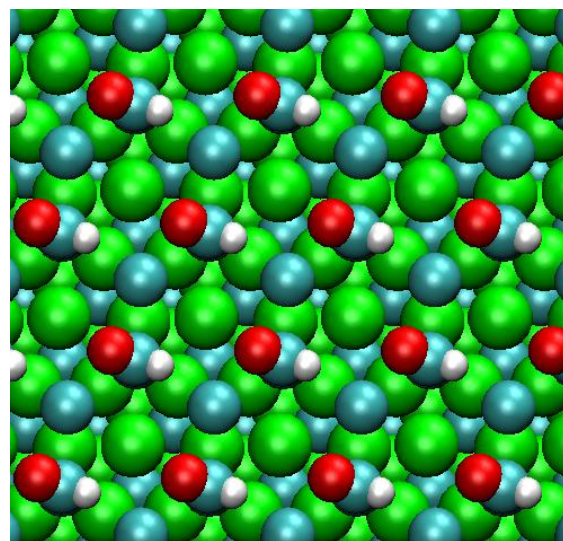


Figure 4.A.10: Adsorption geometry of HCO on reconstructed bare Mo₂C (001) surface. Mo, C, O and H atoms are depicted in green, blue, red and white respectively.

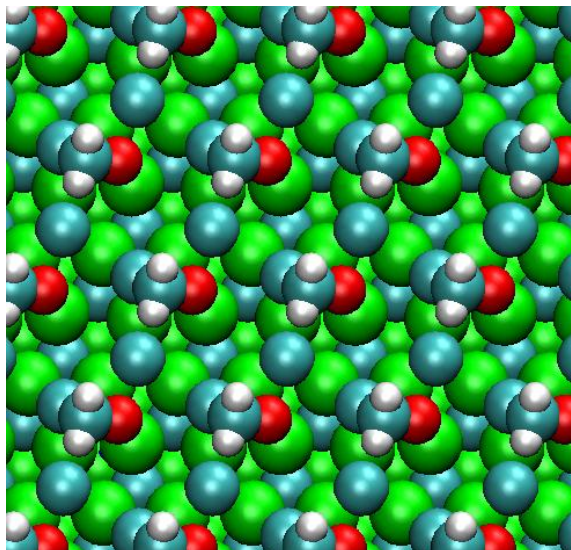


Figure 4.A.11: Adsorption geometry of H₂CO on reconstructed bare Mo₂C (001) surface. Mo, C, O and H atoms are depicted in green, blue, red and white respectively.

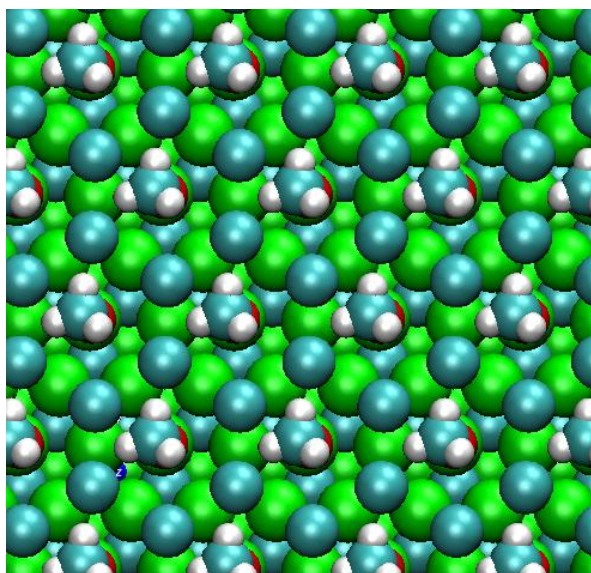


Figure 4.A.12: Adsorption geometry of H₃CO on reconstructed bare Mo₂C (001) surface. Mo, C, O and H atoms are depicted in green, blue, red and white respectively.

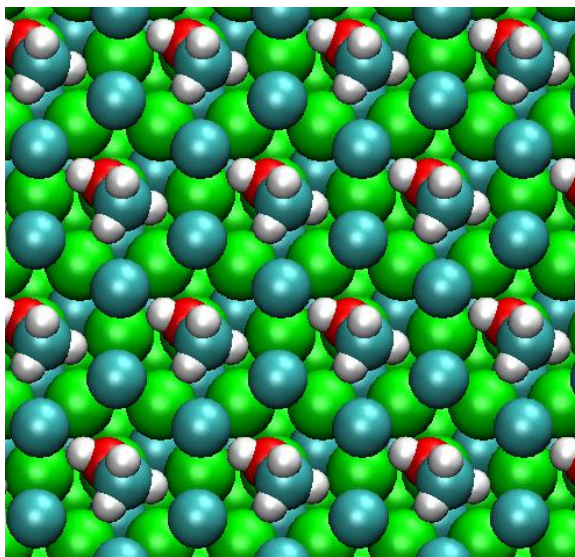


Figure 4.A.13: Adsorption geometry of CH₃OH on reconstructed bare Mo₂C (001) surface. Mo, C, O and H atoms are depicted in green, blue, red and white respectively.

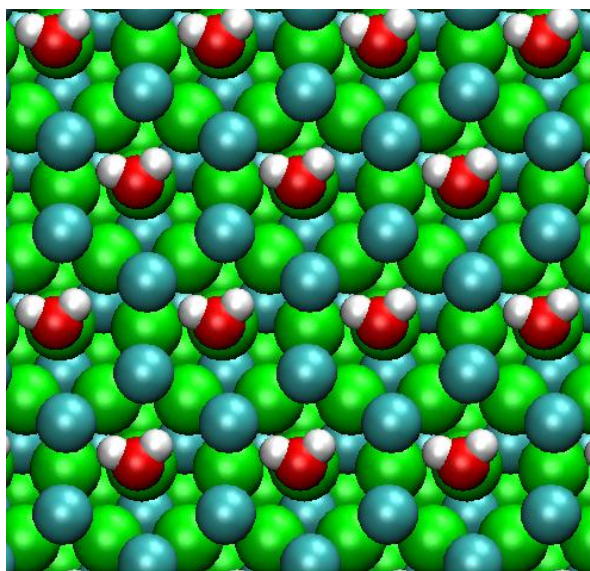


Figure 4.A.14: Adsorption geometry of H₂O on reconstructed bare Mo₂C (001) surface. Mo, C, O and H atoms are depicted in green, blue, red and white respectively.

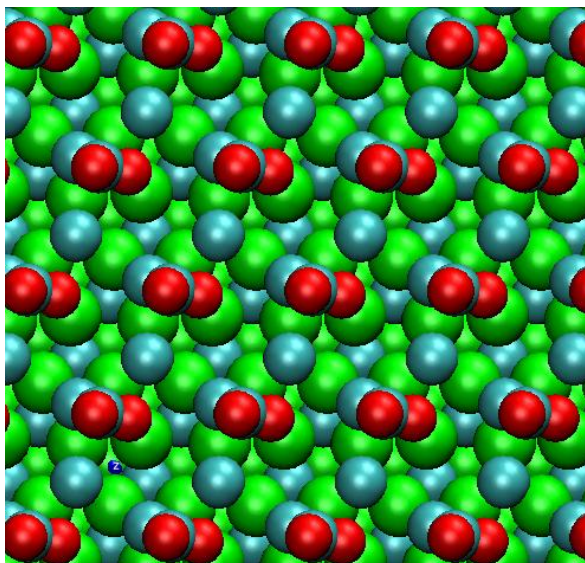


Figure 4.A.15: Adsorption geometry of CO₂ on reconstructed bare Mo₂C (001) surface. Mo, C, and O atoms are depicted in green, blue, and red respectively.

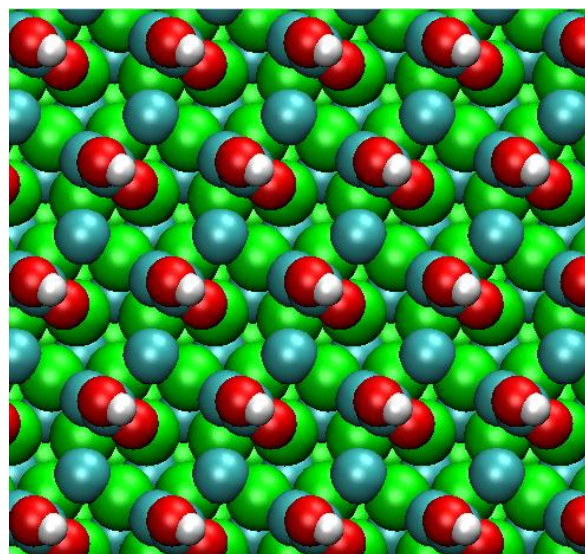


Figure 4.A.16: Adsorption geometry of COOH on reconstructed bare Mo₂C (001) surface. Mo, C, O and H atoms are depicted in green, blue, red and white respectively.

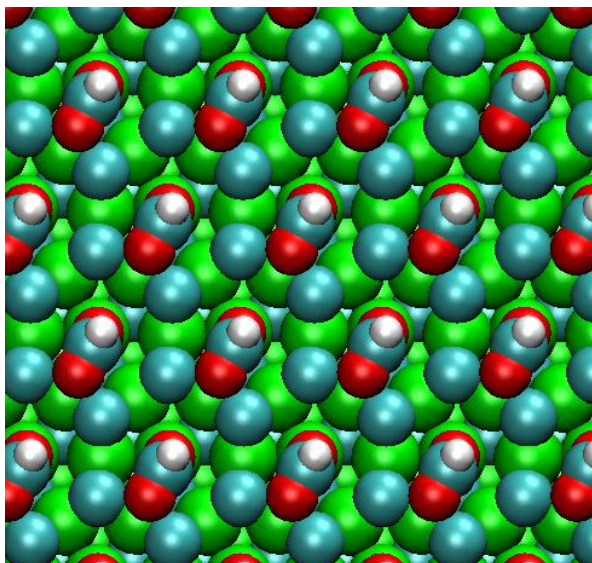


Figure 4.A.17: Adsorption geometry of HCOO on reconstructed bare Mo₂C (001) surface. Mo, C, O and H atoms are depicted in green, blue, red and white respectively.

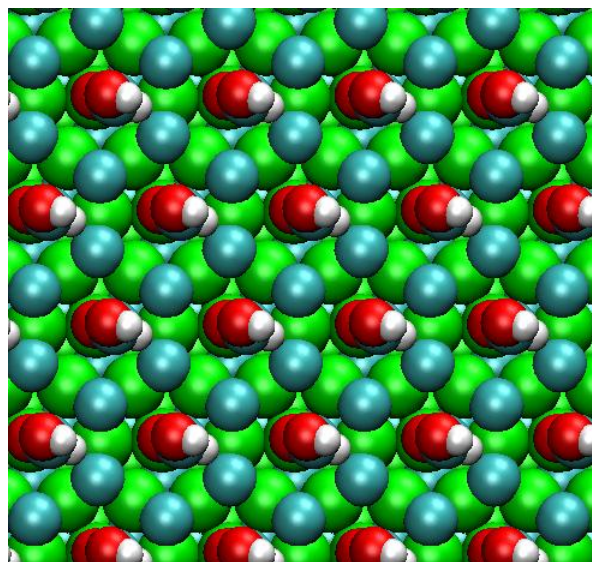


Figure 4.A.18: Adsorption geometry of H₂COO on reconstructed bare Mo₂C (001) surface. Mo, C, O and H atoms are depicted in green, blue, red and white respectively.

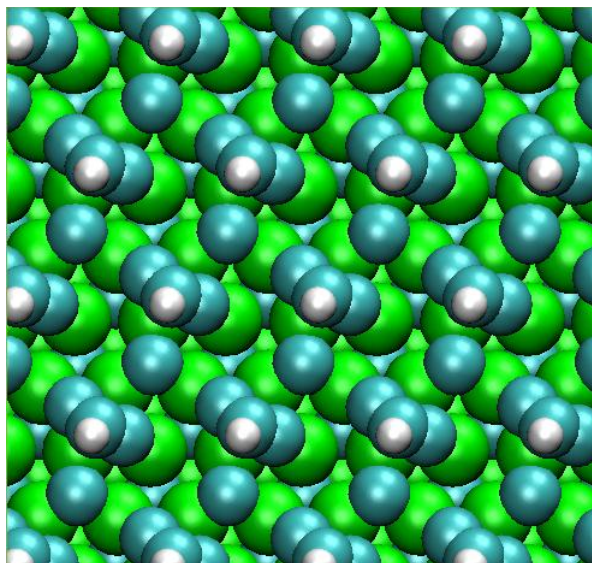


Figure 4.A.19: Adsorption geometry of C₂H on reconstructed bare Mo₂C (001) surface. Mo, C and H atoms are depicted in green, blue and white respectively.

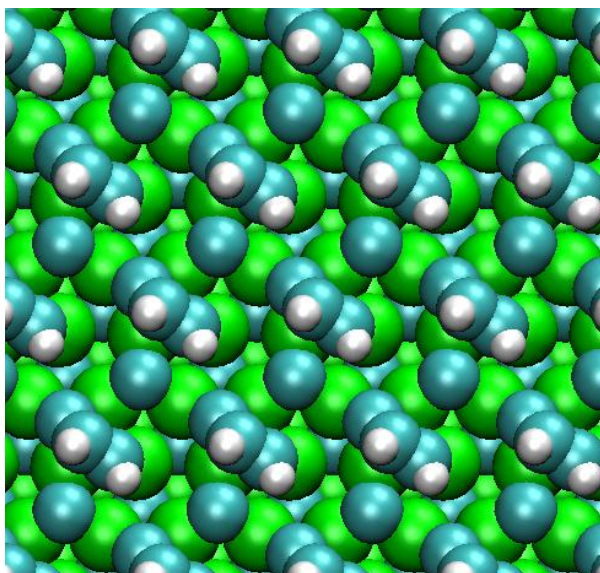


Figure 4.A.20: Adsorption geometry of CHCH on reconstructed bare Mo₂C (001) surface. Mo, C and H atoms are depicted in green, blue and white respectively.

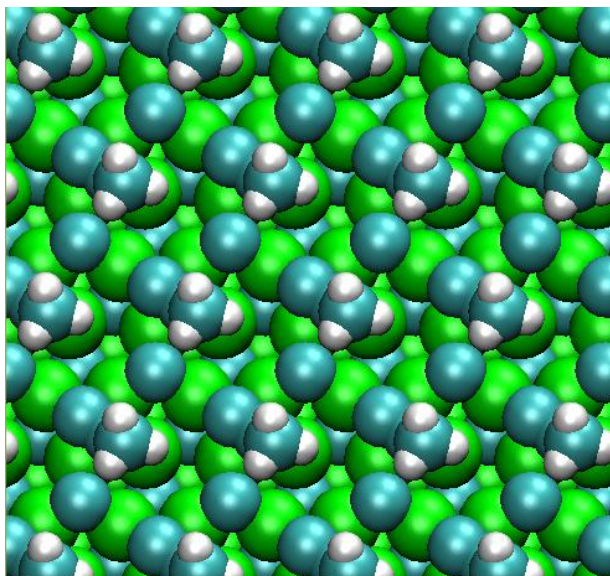


Figure 4.A.21: Adsorption geometry of CCH₃ on reconstructed bare Mo₂C (001) surface. Mo, C and H atoms are depicted in green, blue and white respectively.

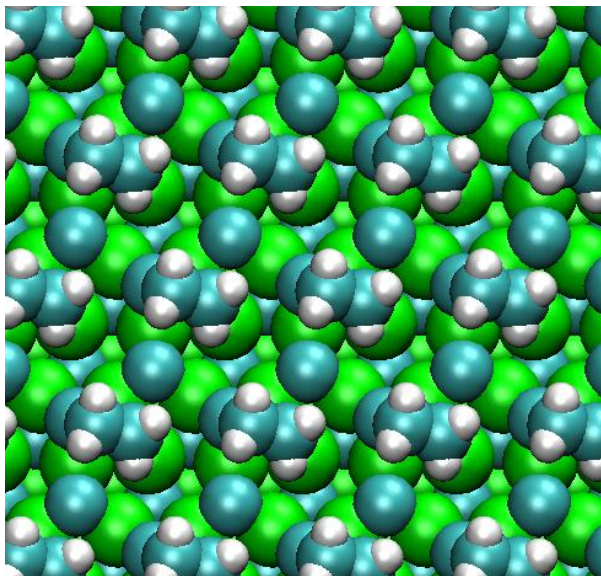


Figure 4.A.22: Adsorption geometry of CH₂CH₂ on reconstructed bare Mo₂C (001) surface. Mo, C and H atoms are depicted in green, blue and white respectively.

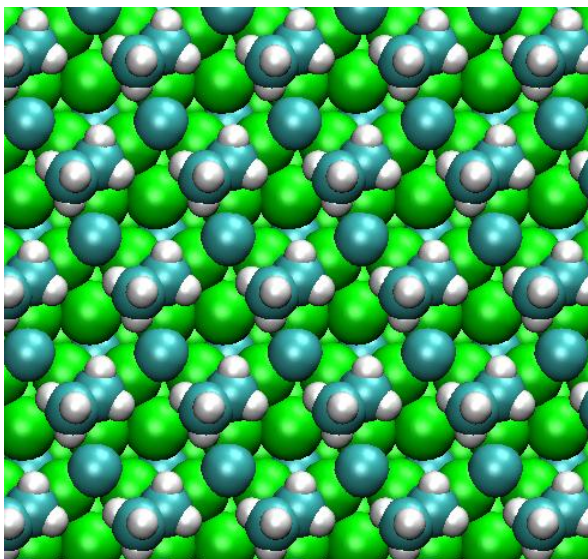


Figure 4.A.23: Adsorption geometry of C₂H₅ on reconstructed bare Mo₂C (001) surface. Mo, C and H atoms are depicted in green, blue and white respectively.

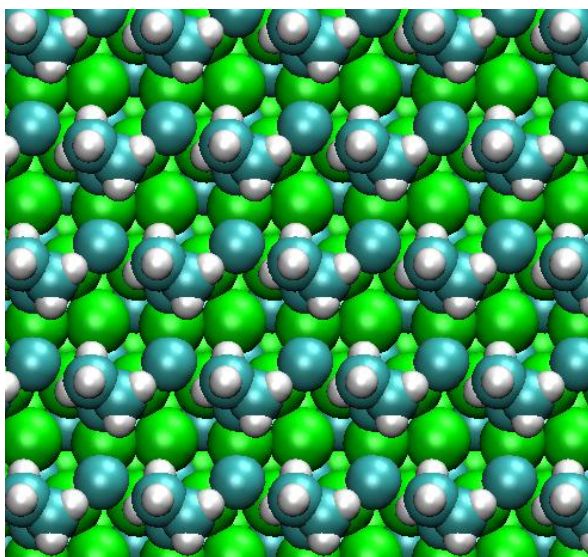


Figure 4.A.24: Adsorption geometry of C₂H₆ on reconstructed bare Mo₂C (001) surface. Mo, C and H atoms are depicted in green, blue and white respectively.

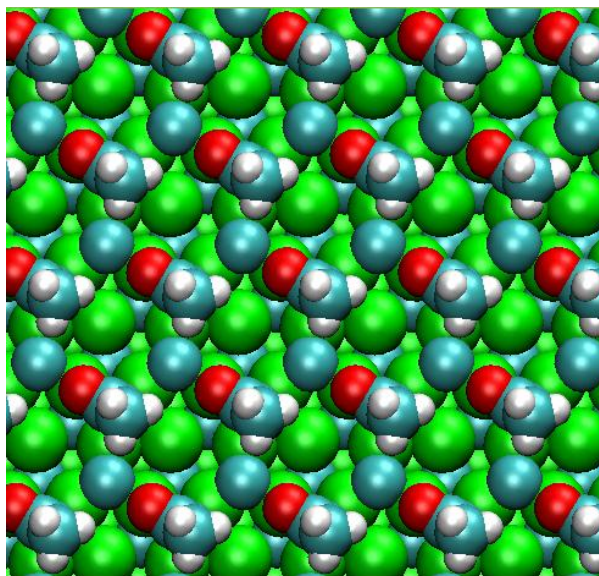


Figure 4.A.25: Adsorption geometry of CH₃CO on reconstructed bare Mo₂C (001) surface. Mo, C, O and H atoms are depicted in green, blue, red and white respectively.

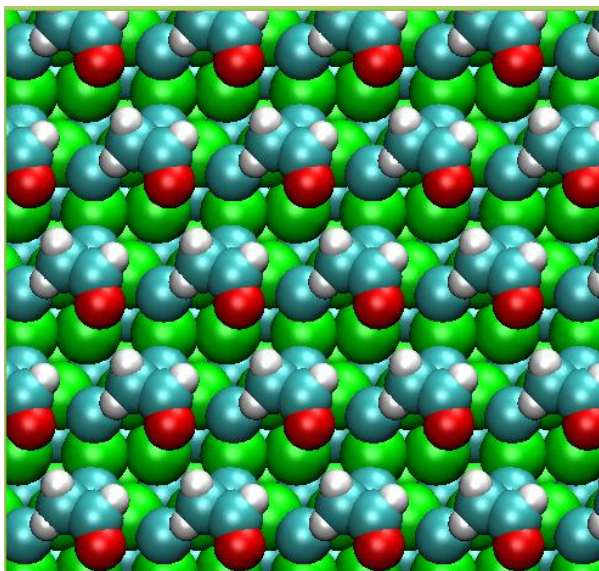


Figure 4.A.26: Adsorption geometry of CH₃CHO on reconstructed bare Mo₂C (001) surface. Mo, C, O and H atoms are depicted in green, blue, red and white respectively.

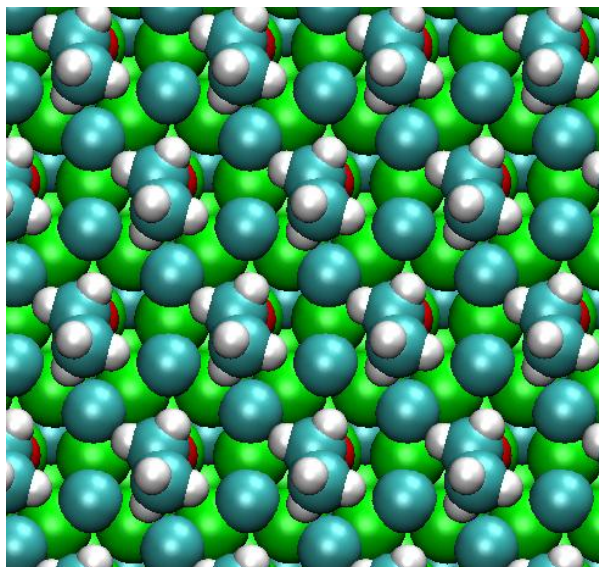


Figure 4.A.27: Adsorption geometry of CH₃CH₂O on reconstructed bare Mo₂C (001) surface. Mo, C, O and H atoms are depicted in green, blue, red and white respectively.

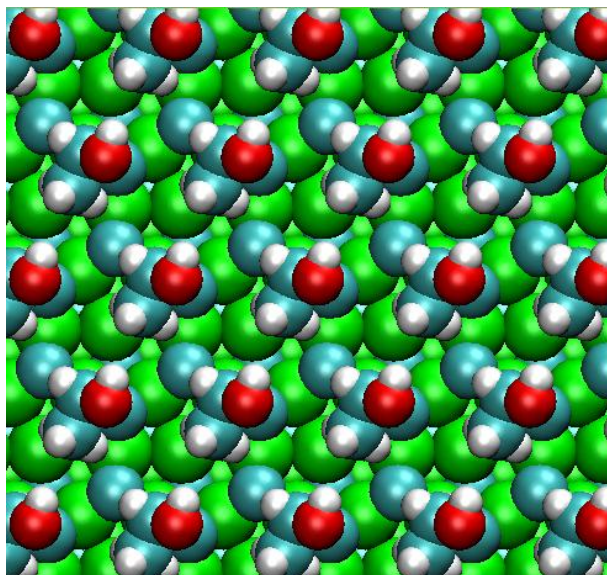


Figure 4.A.28: Adsorption geometry of CH₃CH₂OH on reconstructed bare Mo₂C (001) surface. Mo, C, O and H atoms are depicted in green, blue, red and white respectively.

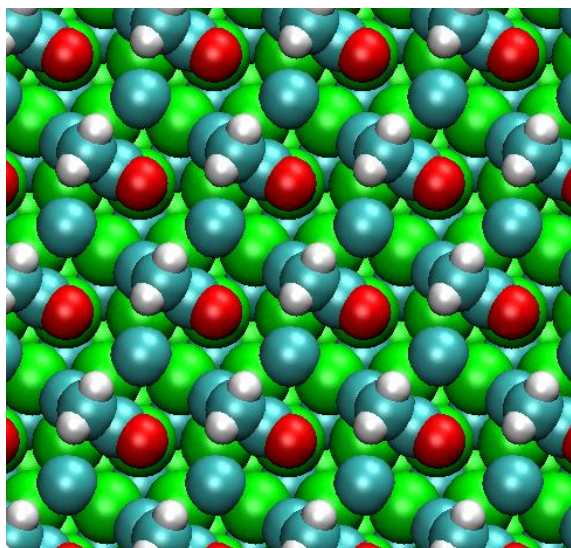


Figure 4.A.29: Adsorption geometry of CH₂CO on reconstructed bare Mo₂C (001) surface. Mo, C, O and H atoms are depicted in green, blue, red and white respectively.

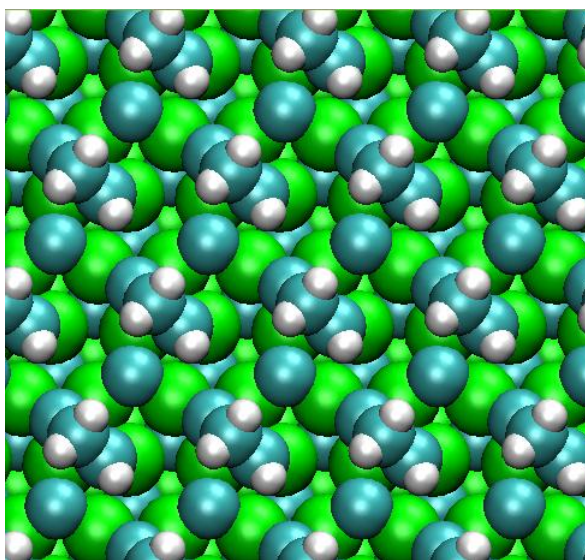


Figure 4.A.30: Adsorption geometry of CHCH₂ on reconstructed bare Mo₂C (001) surface. Mo, C, O and H atoms are depicted in green, blue, red and white respectively.

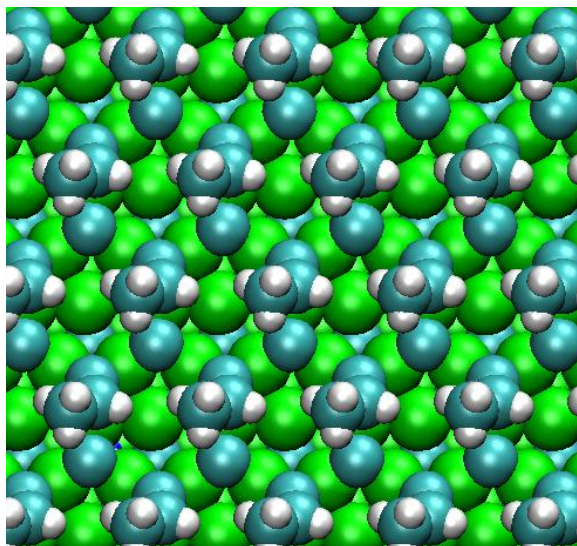


Figure 4.A.31: Adsorption geometry of CHCH₃ on reconstructed bare Mo₂C (001) surface. Mo, C, O and H atoms are depicted in green, blue, red and white respectively.

APPENDIX 4.B

REACTION ENTHALPY COMPUTED FROM DFT AND ACTIVATION ENERGY APPROXIMATED BY THE BEP RELATION IN THE REACTION NETWORK

Table 4.B.1: List of elementary steps with reaction enthalpy and activation energy in the reaction network used in this chapter.

No.	Elementary reactions	ΔH (eV)	E_{act} (eV)
1	$\text{CO(g)} + * \rightarrow \text{CO}^*$	-1.46	N/A
2	$\text{CO}^* \rightarrow \text{CO(g)} + *$	1.46	N/A
3	$\text{H}_2(\text{g}) + 2* \rightarrow 2\text{H}^*$	-1.11	N/A
4	$2\text{H}^* \rightarrow \text{H}_2(\text{g}) + 2*$	1.11	N/A
5	$\text{CO}^* + * \rightarrow \text{C}^* + \text{O}^*$	-0.25	1.45
6	$\text{C}^* + \text{H}^* \rightarrow \text{CH}^* + *$	-0.01	0.87
7	$\text{CH}^* + \text{H}^* \rightarrow \text{CH}_2^* + *$	1.13	0.96
8	$\text{CH}_2^* + \text{H}^* \rightarrow \text{CH}_3^* + *$	0.42	0.90
9	$\text{CH}_3^* + \text{H}^* \rightarrow \text{CH}_4^* + *$	0.42	0.90
10	$\text{CH}_4^* \rightarrow \text{CH}_4(\text{g}) + *$	0.11	N/A
11	$\text{CO}^* + \text{H}^* \rightarrow \text{CHO}^* + *$	1.40	0.98
12	$\text{CHO}^* + \text{H}^* \rightarrow \text{CH}_2\text{O}^* + *$	-0.02	0.87
13	$\text{CH}_2\text{O}^* + \text{H}^* \rightarrow \text{CH}_3\text{O}^* + *$	0.41	0.90
14	$\text{CH}_3\text{O}^* + \text{H}^* \rightarrow \text{CH}_3\text{OH}^* + *$	0.76	0.93
15	$\text{CH}_3\text{OH}^* \rightarrow \text{CH}_3\text{OH}(\text{g}) + *$	0.54	N/A
16	$\text{H}^* + \text{O}^* \rightarrow \text{OH}^* + *$	0.40	0.90
17	$\text{OH}^* + \text{H}^* \rightarrow \text{H}_2\text{O}^* + *$	0.51	0.91
18	$\text{H}_2\text{O}^* \rightarrow \text{H}_2\text{O}(\text{g}) + *$	0.61	N/A
19	$\text{CO}^* + \text{O}^* \rightarrow \text{CO}_2^* + *$	0.71	1.21
20	$\text{CO}_2^* \rightarrow \text{CO}_2(\text{g}) + *$	0.16	N/A
21	$\text{H}_2\text{O}^* + * \rightarrow \text{H}^* + \text{OH}^*$	-0.51	0.40
22	$\text{OH}^* + * \rightarrow \text{O}^* + \text{H}^*$	-0.40	0.50
23	$\text{OH}^* + \text{OH}^* \rightarrow \text{H}_2\text{O}^* + \text{O}^*$	0.10	0.97
24	$\text{CO}^* + \text{OH}^* \rightarrow \text{COOH}^* + *$	0.50	1.16
25	$\text{COOH}^* + * \rightarrow \text{CO}_2^* + \text{H}^*$	-0.20	0.68
26	$\text{COOH}^* + \text{OH}^* \rightarrow \text{CO}_2^* + \text{H}_2\text{O}^*$	0.31	1.15
27	$\text{CO}_2^* + \text{H}^* \rightarrow \text{HCOO}^* + *$	0.81	0.93
28	$\text{HCOO}^* + \text{H}^* \rightarrow \text{H}_2\text{COO}^* + *$	0.71	0.93
29	$\text{H}_2\text{COO}^* + \text{H}^* \rightarrow \text{H}_3\text{CO}^* + *$	-0.43	0.84
30	$\text{C}^* + \text{CH}^* \rightarrow \text{C}_2\text{H}^* + *$	1.14	1.33
31	$\text{CH}^* + \text{CH}^* \rightarrow \text{CHCH}^* + *$	1.31	1.37

32	$C^* + CH_3^* \rightarrow CCH_3^* + ^*$	-0.30	0.95
33	$CH_2^* + CH_2^* \rightarrow CH_2CH_2^* + ^*$	0.55	1.17
34	$C_2H^* + H^* \rightarrow CHCH^* + ^*$	0.16	0.88
35	$CHCH^* + H^* \rightarrow CHCH_2^* + ^*$	0.59	0.92
36	$CHCH_2^* + H^* \rightarrow CH_2CH_2^* + ^*$	0.91	0.94
37	$CH_2CH_2^* \rightarrow C_2H_4(g) + ^*$	0.55	N/A
38	$CH_2CH_2^* + H^* \rightarrow C_2H_5^* + ^*$	-0.18	0.86
39	$C_2H_5^* + H^* \rightarrow C_2H_6^* + ^*$	0.81	0.94
40	$C_2H_6^* \rightarrow C_2H_6(g) + ^*$	0.03	N/A
41	$CH_3^* + CO^* \rightarrow CH_3CO^* + ^*$	0.50	1.16
42	$CH_3CO^* + H^* \rightarrow CH_3CHO^* + ^*$	1.34	0.98
43	$CH_3CHO^* + H^* \rightarrow CH_3CH_2O^* + ^*$	-0.40	0.84
44	$CH_3CH_2O^* + H^* \rightarrow CH_3CH_2OH^* + ^*$	1.38	0.98
45	$CH_3CH_2OH^* \rightarrow CH_3CH_2OH(g) + ^*$	0.05	N/A
46	$CH_2^* + CO^* \rightarrow CH_2CO^* + ^*$	0.99	1.29
47	$CH_2CO^* + H^* \rightarrow CH_3CO^* + ^*$	-0.07	0.86
48	$CH_3CH_2O^* + ^* \rightarrow C_2H_5^* + O^*$	-0.62	1.09
49	$CCH_3^* + H^* \rightarrow CHCH_3^* + ^*$	1.12	0.96
50	$CHCH_3^* + H^* \rightarrow C_2H_5^* + ^*$	0.26	0.89
51	$H_2CO^* + ^* \rightarrow CH_2^* + O^*$	-0.51	0.65
52	$H_3CO^* + ^* \rightarrow CH_3^* + O^*$	-0.50	1.20
53	$CH^* + CH_2^* \rightarrow CHCH_2^* + ^*$	0.12	1.06
54	$CH^* + CH_3^* \rightarrow CHCH_3^* + ^*$	1.26	1.36
55	$CH_2^* + CH_3^* \rightarrow CH_2CH_3^* + ^*$	-0.05	1.02
56	$CH_3^* + CH_3^* \rightarrow C_2H_6^* + ^*$	0.35	1.12

APPENDIX 4.C

COMPARISON OF MF, QCA, AND MC FOR A SIMPLE ADSORPTION/DESORPTION CASE

This appendix describes our calculations in comparing Mean Field (MF) approximation, Quasi-chemical approximation (QCA) and Monte Carlo (MC) for a simple adsorption/desorption process on a 2-D square lattice. The interaction energy between two nearest adsorbates are defined as a variable to examine the performance of these methods with different types (attractive, repulsive) and magnitudes (strong, weak) of interactions. We have studied cases of repulsive interaction of 0.2 eV, attractive interaction of 0.2 eV, repulsive interaction of 0.05 eV, and repulsive interaction of 0.0001 eV. For each case, the average interaction energy per particle was plotted as a function of surface coverage. For MF, since the interactions do not influence the configurations of surface adsorbates. The coverage of the nearest adsorbate pair A-A is $\theta_A \cdot \theta_A$. For QCA, the coverage of the nearest adsorbate pair, θ_{AA} is calculated by:

$$\theta_{**} = 1 - \theta_* - \frac{2\theta_*(1 - \theta_*)}{1 + \beta}$$

where

$$\beta = \left[1 - 4\theta_*(1 - \theta_*)(1 - \exp\left(\frac{-w}{k_B T}\right)) \right]^{1/2}$$

$$\theta_{A*} = 2(1 - \theta_*) - 2\theta_{**}$$

$$\theta_{AA} = 1 - \theta_{**} - \theta_{A*}$$

For Monte Carlo simulation, the canonical ensemble was employed, where the number of adsorbates, the number of adsorption sites on the 2D lattice and temperature are kept as

constants for each MC run. Adsorbates at a certain coverage were placed randomly on the lattice. For each step, the adsorbates were allowed to move to one randomly picked adjacent site, with the possibility of acceptance defined by the Metropolis method. After one million steps, which the surface redistribution reached equilibrium. The average interaction energy per adsorbate was computed. The results are shown below.

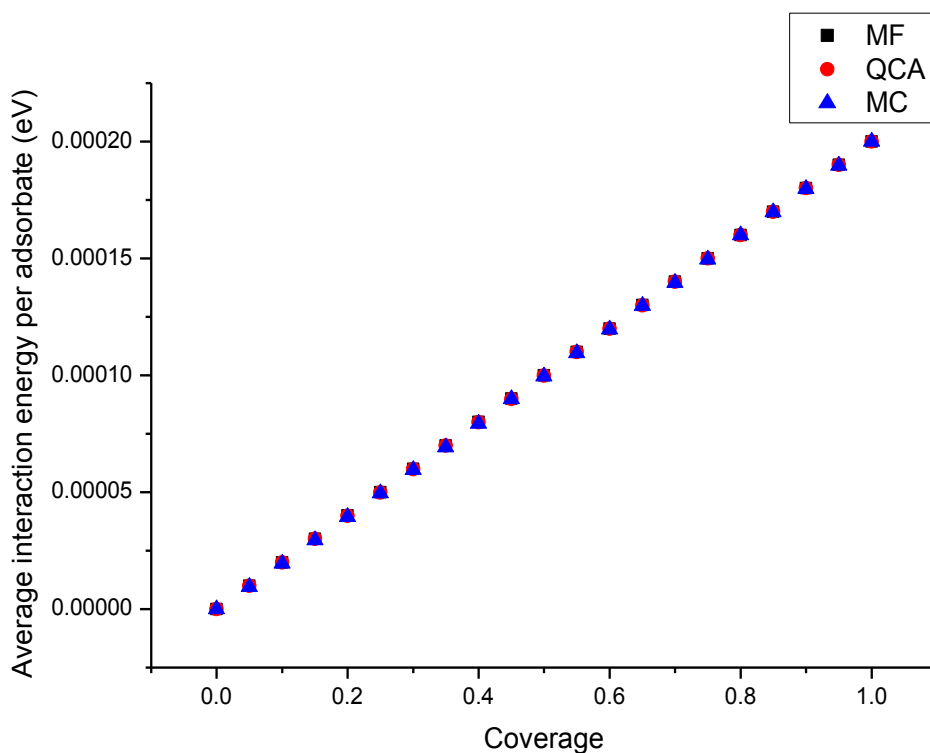


Figure 4.C.1: Comparison of MF, QCA and MC for interaction energy = 0.0001 eV (repulsive) at 573 K.

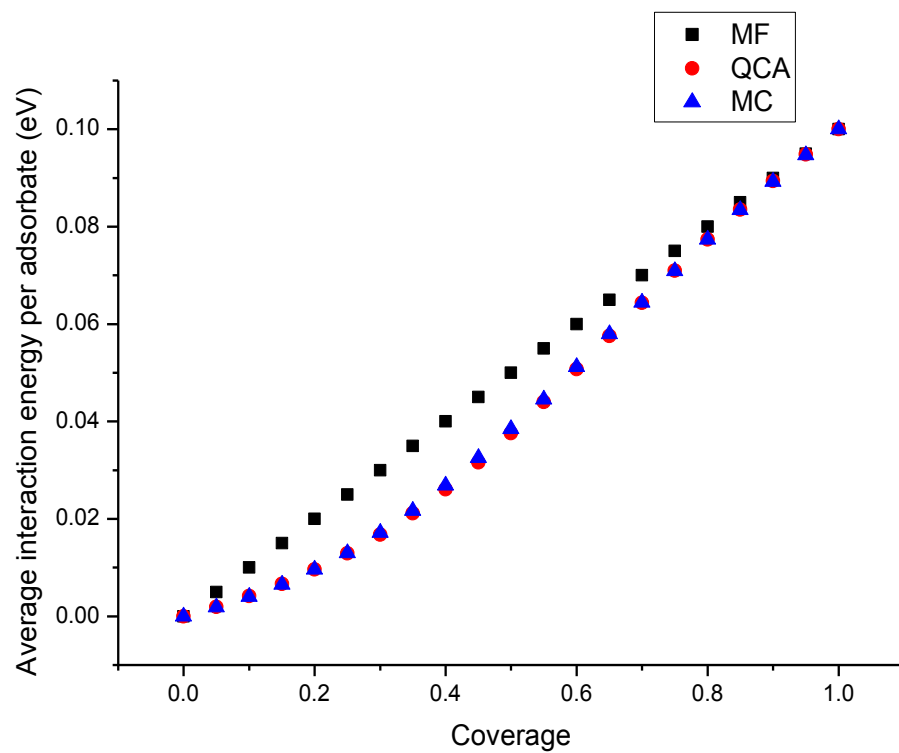


Figure 4.C.2: Comparison of MF, QCA and MC for interaction energy = 0.05 eV (repulsive) at 573 K.

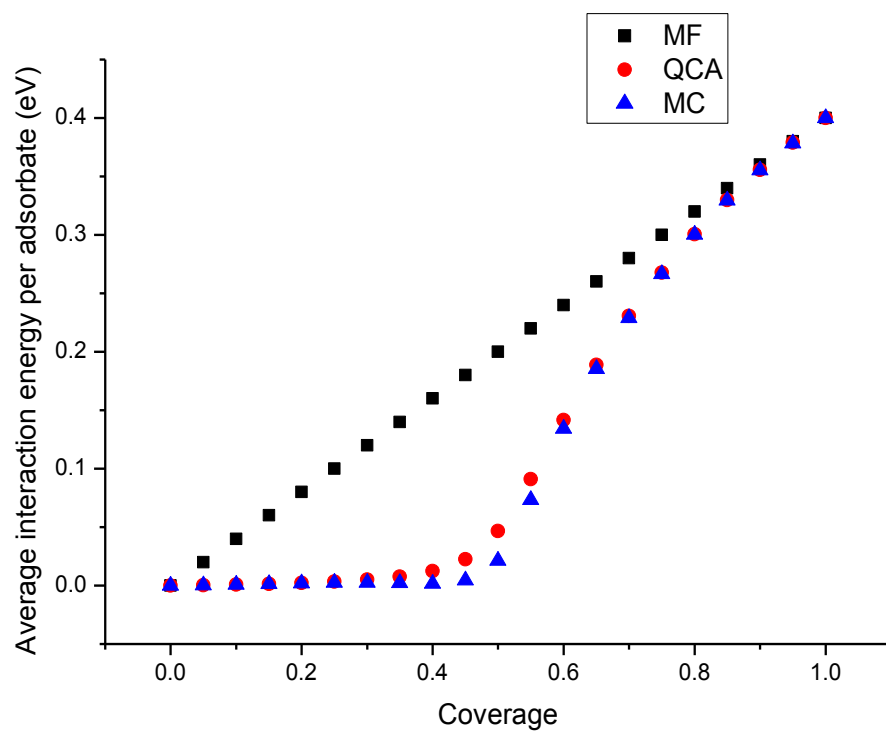


Figure 4.C.3: Comparison of MF, QCA and MC for interaction energy = 0.2 eV (repulsive) at 573 K.

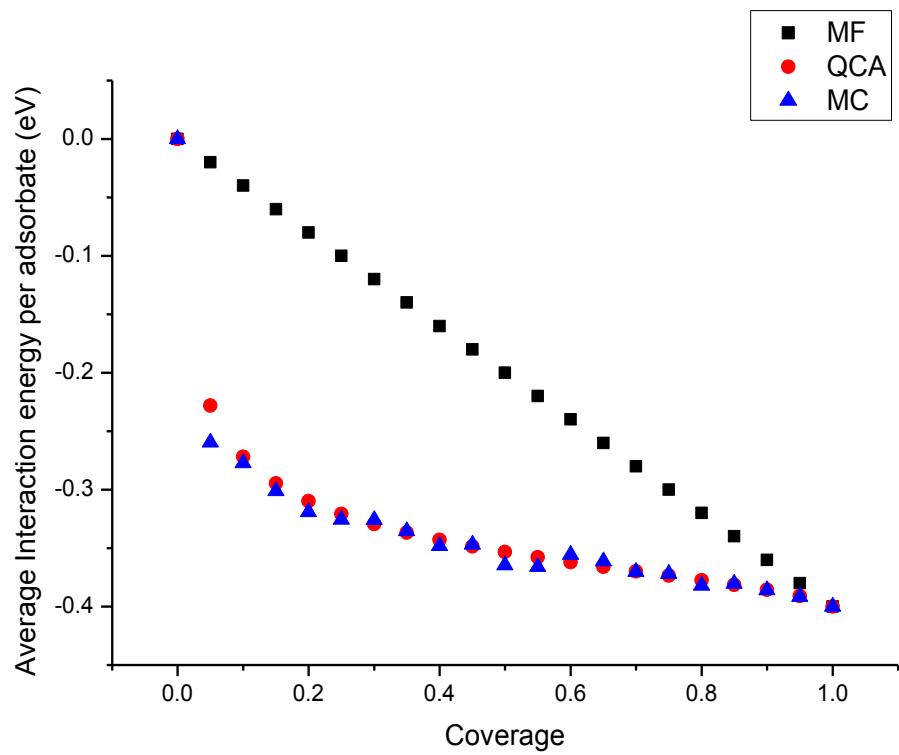


Figure 4.C.4: Comparison of MF, QCA and MC for interaction energy = -0.2 eV (attractive) at 573 K.

APPENDIX 4.D

STEADY STATE COVERAGE SOLVED FROM MICROKINETIC

MODEL UNDER EXPERIMENTAL CONDITION USED

Table 4.D.1: Steady state coverage solved from microkinetic model at 573 K, 30 bar of syngas with CO/H₂ in an 1:1 ratio.

No.	Species	Coverage	Percentage coverage
1	CO*	2.1474E-01	21.47%
2	H*	5.7788E-03	0.58%
3	C*	5.5417E-06	0.00%
4	O*	6.2262E-01	62.26%
5	CH*	2.0639E-05	0.00%
6	CH ₂ *	3.1849E-02	3.18%
7	OH*	3.4844E-05	0.00%
8	CH ₃ *	1.7531E-02	1.75%
9	CH ₄ *	2.6094E-18	0.00%
10	CHO*	2.1429E-02	2.14%
11	CH ₂ O*	5.2780E-05	0.01%
12	OCH ₃ *	9.2396E-05	0.01%
13	CH ₃ OH*	8.7436E-18	0.00%
14	H ₂ O*	1.5142E-17	0.00%
15	CO ₂ *	1.4658E-17	0.00%
16	COOH*	1.6319E-08	0.00%
17	HCOO*	9.5778E-28	0.00%
18	H ₂ COO*	3.3682E-23	0.00%
19	C ₂ H*	2.5642E-12	0.00%
20	CHCH*	1.2701E-11	0.00%
21	CCH ₃ *	1.9919E-05	0.00%
22	CH ₂ CH ₂ *	1.5680E-16	0.00%
23	C ₂ H ₅ *	1.8275E-02	1.83%
24	C ₂ H ₆ *	4.5063E-19	0.00%
25	CH ₃ CO*	1.8031E-02	1.80%
26	CH ₃ CHO*	1.0672E-03	0.11%
27	CH ₃ CH ₂ O*	1.9158E-02	1.92%
28	CH ₃ CH ₂ OH*	2.3667E-19	0.00%
29	*	2.9060E-02	2.91%
30	CH ₂ CO*	2.2732E-04	0.02%
31	CHCH ₂ *	1.0197E-05	0.00%
32	CHCH ₃ *	4.9392E-06	0.00%
Total		1.000000E+00	100.00%

CHAPTER 5

INVESTIGATION OF ALKALI PROMOTER FORMATION ON MO₂C CATALYSTS FOR ALCOHOL SYNTHESIS REACTIONS - A JOINT STUDY OF INFRARED SPECTROSCOPY AND DFT

5.1 Introduction

Fischer-Tropsch synthesis (FTS) of hydrocarbons has received growing attention as a source of low-sulfur diesel fuel because of the uncertainty of crude oil prices. However, higher alcohol (C₂₊ alcohols) synthesis from synthesis gas, as a source of chemical feedstocks, might be more commercially attractive. For example, Celanese Corporation reported an expected ethanol price of \$1.4/gallon with their new coal-to-ethanol technology via acetic acid,¹ and E. I. du Pont de Nemours and Company and BP have a stated goal for a butanol price of \$1/gallon with their bio-based process currently under development.² Considering that methanol is currently produced from natural-gas based syngas at the world scale, it is reasonable to expect a comparably low price for higher alcohols produced by a similar catalytic process, assuming production and selectivity achievements are realized.

An effective catalyst for the production of higher alcohols from syngas is necessarily multifunctional since CO activation, hydrogenation, carbon chain growth, and potentially alcohol coupling processes are all important steps in the reaction. Thus, no single-component transition metal catalyst has been discovered to effectively catalyze higher alcohol synthesis.

Exploratory research on higher alcohol synthesis has discovered some promising candidates.³⁻⁷ Rh-based catalysts are effective for the formation of ethanol and other C₂-oxygenates from syngas,⁸⁻¹⁰ but the very high cost of Rh likely prohibits its large-scale utilization. Several non-precious metal catalysts for higher alcohol synthesis have thus been evaluated and include, for example, Cu–Co, Cu–Zn–Al and Zn–Cr–K,⁴ but improvements in the overall catalytic activity, alcohol selectivity, and long-term stability of these catalytic materials for higher alcohol synthesis are still needed.

Molybdenum-based catalysts have been widely used in many hydro-treating processes because of their high activities in desulfurization and denitrogenation with H₂. When promoted by alkali metals, Mo-based catalysts also show encouraging properties for higher alcohol synthesis from CO hydrogenation. Both supported and unsupported MoS₂-based catalysts have been heavily investigated for higher alcohol synthesis¹¹⁻¹⁴ since it was firstly developed by The Dow Chemical Company in the 1980's.¹⁵⁻¹⁹ However, trace amounts of H₂S in the feed were required to sustain the performance of the MoS₂-based catalysts.¹⁶ Moreover, small amounts of sulfur may enter the carbon skeleton of the products, which is problematic as the world moves toward the use of very-low-sulfur fuels. Thus, there is a need for a non-sulfided alternative to MoS₂-based catalysts in this process, among which molybdenum carbide has demonstrated some promise when properly promoted.²⁰⁻²⁴ Early transition metal carbides are also recognized as potential substitutes to precious metal catalysts because of their similar surface electronic properties.²⁵⁻²⁷

The selectivity towards alcohols over alkali-metal-promoted MoS₂-based and Mo₂C-based catalysts in the syngas reaction was reported to be low initially but increased

significantly with time on-stream over a period of several hours to several days.^{22,28-30} Lee et al. suggested that the promotional effect of alkali metal species on MoS_2 ¹² and Mo_2C ³¹ catalysts for alcohol formation during CO hydrogenation was mostly the result of the surface sites being blocked from adsorbing reactants. By using diffuse reflectance infrared Fourier-transform spectroscopy (DRIFTS), Koizumi et al. claimed that syngas adsorption on a $\text{MoS}_2/\text{Al}_2\text{O}_3$ catalyst for CO hydrogenation was significantly suppressed by K species and the K-promoted Mo species were likely more oxidized than those on K-free MoS_2 .³² Muramatsu et al. also studied the role of a K promoter on a Mo oxide catalyst for alcohol production from syngas and concluded that K inhibits both dehydration of alcohols to alkenes and the hydrogenation of alkenes to alkanes.³³ For supported MoS_2 -based catalysts, interactions between K promoters and Mo begins with the oxidized catalyst precursors^{11,28,34,35} and that some K–Mo–S and/or K–Mo–S–O species are formed after sulfidation. However, it is still unclear whether the promoters enhance the activity of the catalysts for higher alcohol synthesis. Although CO adsorption has been used to probe the surfaces of MoS_2 -based³⁶⁻⁴¹ and Mo_2C -based⁴²⁻⁴⁵ catalysts, few of these studies addressed the promotional influence of the alkali metals on higher alcohol synthesis. X-ray absorption spectroscopy of Rb-promoted $\text{Mo}_2\text{C}/\text{MgO}$ catalysts demonstrated that the local environment around the Rb_2CO_3 promoter was structurally-modified during reaction,²² but the actual structural form of the working promoter is not yet known.

The present chapter uses diffuse reflectance infrared Fourier transform spectroscopy (DRIFTS) of adsorbed CO combined with density functional theory (DFT) to investigate the interactions between CO and Rb promoter on supported- Mo_2C

particles. A hypothesis on alkali promoter formation mechanism consistent with experimental and computational results is further proposed. The experimental work described in this chapter was performed by Dr. Heng Shou and Prof. Robert Davis at the University of Virginia.

5.2 Methods

5.2.1 Catalyst synthesis

Incorporation of Mo onto an alumina support (Mager Scientific, >99.98%, predominantly γ -phase, $S_{\text{BET}} = 76 \text{ m}^2 \text{ g}^{-1}$) was accomplished by incipient wetness impregnation of an aqueous solution of $(\text{NH}_4)_6\text{Mo}_7\text{O}_{24} \cdot 4\text{H}_2\text{O}$ (99.98%, Aldrich) followed by drying in air for 12 h at 400 K and calcining in flowing air for 5 h at 773 K to produce a supported molybdenum oxide, denoted here as $\text{MoO}_3/\text{Al}_2\text{O}_3$. Carburization of $\text{MoO}_3/\text{Al}_2\text{O}_3$ was performed in a quartz tube by heating at a rate of 5 K min^{-1} from room temperature to 573 K and at a rate of 1 K min^{-1} from 573 K to 1033 K in 20 vol.% CH_4 (GTS-Welco, 99.997%) and 80 vol.% H_2 (GTS-Welco, 99.999%) at a total gas flow rate of $75 \text{ cm}^3 \text{ min}^{-1}$ (STP). After ramping to 1033 K in CH_4/H_2 , the temperature was maintained at 1033 K for 1 h. The catalyst was subsequently cooled to 673 K in flowing He (GTS-Welco, 99.999%, additionally purified by a Sigma-Aldrich OMI-2 purifier) and held at 673 K for 5 h in flowing purified H_2 at a flow rate of $60 \text{ cm}^3 \text{ (STP) min}^{-1}$. The catalyst was then cooled to room temperature in flowing purified He before passivation in a $20 \text{ cm}^3 \text{ min}^{-1}$ (STP) stream of 1.04 vol.% O_2/N_2 mixture (GTS-Welco) at room temperature for 12 h. The alkali-metal-promoted $\text{Mo}_2\text{C}/\text{Al}_2\text{O}_3$ samples were prepared by grinding Rb_2CO_3 (99.975%, Alfa Aesar) together with passivated $\text{Mo}_2\text{C}/\text{Al}_2\text{O}_3$ in a mortar and pestle.

5.2.2 Diffuse reflectance Infrared Fourier transform spectroscopy

A Bio-Rad FTIR (FTS-60A) spectrometer outfitted with an MCT detector and an *in situ* reactor cell for DRIFTS (Harrick) was used for the CO adsorption studies. To obtain the spectra, 100 scans were co-added at resolution of 4 cm^{-1} . Samples of 2 wt.% $\text{Mo}_2\text{C}/\text{Al}_2\text{O}_3$ catalysts with Rb loading varying from 0–10 wt.% were examined by DRIFTS according to the following procedure. A catalyst sample of 30 mg was diluted in 90 mg of KBr powder (Varian Inc.) before being loaded into the DRIFTS cell.

The loaded cell was then purged with He (GTS-Welco, 99.999%, additionally purified by Sigma-Aldrich OMI-2) at a flow rate of $50\text{ cm}^3\text{min}^{-1}$ (STP) at room temperature for 10 min before being pressurized with equal flow rates of H_2 (GTS-Welco, 99.999%, additionally purified by Alltech All-Pure) and purified CO (GTS-Welco, 99.997%) to 30 bar. The purification system for CO was comprised of a CRS Model 1000 O_2 trap, a homemade carbonyl trap (silica gel in a copper tube immersed in a dry ice/acetone cold bath), a homemade CO_2 trap (Ascarite II CO_2 absorbent in a copper tube) and a homemade moisture trap (Fluka molecular sieves 3 \AA loaded in a copper tube). Subsequently, the cell was heated to 573 K at a rate of 10 K min^{-1} and held at 573 K for 12 h in 30 bar flowing syngas ($\text{H}_2/\text{CO} = 1$) with a total flow rate of $4\text{ cm}^3\text{ min}^{-1}$ (STP). The cell was depressurized after 12 h treatment at reaction conditions and purged with $50\text{ cm}^3\text{ min}^{-1}$ (STP) H_2 at 573 K, ambient pressure, for an additional 1 h before cooling to room temperature in flowing He. After recording a background spectrum of the sample, flowing He was replaced with purified CO flowing at a rate of 50 mLmin^{-1} for 15 min. The sample was finally purged with flowing purified He at 50 mLmin^{-1} for 15 min before recording a spectrum of adsorbed CO at 300 K.

In another series of studies on representative samples, water was introduced to the catalyst by flowing He to the DRIFTS cell through a saturator with liquid water at 300 K. The samples were sequentially treated with the following conditions: 1 bar H₂O/He (50 cm³min⁻¹, STP) at 300 K for 2 h and 1 bar He (50 cm³min⁻¹, STP) at 423 K for 1 h; 1 bar H₂ (50 cm³min⁻¹, STP) at 573 K for 12 h; 30 bar syngas (H₂/CO=1, total flow rate at STP of 4 cm³min⁻¹) for 12 h and in 1 bar H₂ (50 cm³min⁻¹, STP) for 1 h; 1 bar H₂ (50 cm³min⁻¹, STP) at 573 K for 12 h. After each step of the pretreatment sequence, the sample was cooled to 300 K in flowing purified He (50 cm³min⁻¹, STP). The background spectra were subsequently recorded at 300 K in flowing He before introducing purified CO (50 cm³min⁻¹, STP) for 15 min. After purging with flowing purified He at 50 cm³min⁻¹ for 15 min, the IR spectra of adsorbed CO were recorded at 300 K. In control experiments without water, the samples were pretreated with 50 cm³ min⁻¹ (STP) purified H₂ at 573 K for 12 h and purged in purified He before introducing purified CO at 300 K.

5.2.3 Computational methods

Plane wave DFT calculations were performed with the Vienna *ab initio* simulation package (VASP). We employed the revised Perdew-Burke-Ernzerhof (rPBE) generalized gradient functional^{46,47} along with the projector augmented wave (PAW)^{48,49} method to describe ionic cores. A plane wave expansion with a cutoff of 400 eV was used for all calculations. Geometries were relaxed using a conjugate gradient algorithm until the forces on all unconstrained atoms were less than 0.03 eV/Å.

The surface structure of the molybdenum carbide catalyst modeled is based on the reconstructed C-terminated hexagonal α -Mo₂C(001) surface discussed in Chapter 3, which is illustrated in Fig. 5.1. In Chapter 3, by comparing the surface free energy and

the adsorption energy of alkali metal (K and Rb) atoms for different low-Miller-index surfaces of Mo_2C , the $\text{Mo}_2\text{C}(001)$ surface was found to be one of the major surfaces in predicted Mo_2C particles as well as have the greatest affinity and dipole moment for Rb atoms. This surface is also known to favor a reconstruction in the absence of adsorbates,⁵⁰⁻⁵² which results in both Mo-top and C-top sites for CO adsorption. Moreover, in spite of the potential support effect, the behavior of bulk Mo_2C catalysts and Mo_2C catalysts^{20,21} and Mo_2C catalysts on various supports (MgO ,²² $\alpha\text{-Al}_2\text{O}_3$ ²⁴ and mixed-phase Al_2O_3) is similar, which suggests that the actual sites on various Mo_2C catalysts for CO hydrogenation would have a similar configuration. Given all the factors mentioned above, $\text{Mo}_2\text{C}(001)$ was chosen as a representative surface for modeling.

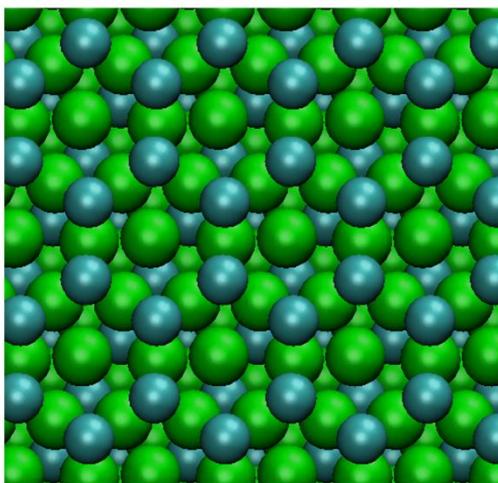


Figure 5.1: Top view of reconstructed hexagonal $\alpha\text{-Mo}_2\text{C}(001)$ surface. Mo (C) atoms are shown as green (blue) spheres.

A $6\times 6\times 1$ Monkhorst-Pack k-point mesh was used for (1×1) surface unit cell, which was sufficient to give well-converged results. For calculations on a (2×2) surface unit cell, the number of k-points in the Monkhorst-Pack meshes was reduced to $3\times 3\times 1$.

Geometries and energies for gas phase species were calculated using supercells equivalent to those for the largest slab calculations. When examining adsorption, molecules were placed on only one side of the slab. Dipole corrections were therefore applied in computing all of the energies reported below.^{53,54} The adsorption energy, $E_{\text{adsorption}}$, of an atom or molecule was defined by

$$E_{\text{adsorption}} = (E_{\text{surface}} + E_{\text{adsorbate}}) - E_{\text{total}}, \quad (5.1)$$

where E_{total} is the total energy of the system containing the adsorbed species, E_{surface} is the total energy for the optimized bare surface, and $E_{\text{adsorbate}}$ is the total energy for the adsorbate in the gas phase. With this definition, positive adsorption energies correspond to energetically favored states. Adsorbate coverages were defined by considering a surface with an adsorbed species on every surface molybdenum atom to have a coverage of 1 monolayer (ML). This means that placing one adsorbate in a 1×1 unit cell gives a coverage of 0.25 ML.

Vibrational frequency calculations were performed with the VASP package where the Hessian Matrix was calculated by finite difference approximation with step size of 0.03 \AA . Only the adsorbate plus the surface atom to which it directly bonds were allowed to move. In order to compare with IR experiments, the calculated frequencies for the CO adsorbates are scaled by a factor of 1.009, which reflects the difference between the calculated (2124 cm^{-1}) and observed (2143 cm^{-1}) vibrational frequencies of gas phase CO.

5.3 Results and Discussion

5.3.1 Infrared spectroscopy results and DFT calculation of CO adsorption on bare Mo₂C catalysts

The formation of products during the syngas pretreatment (573 K, 30 bar syngas, H₂/CO = 1, 12 h reaction in syngas) in the DRIFTS experiments was verified by monitoring the IR spectrum during syngas reaction over a 5 wt.% Rb–2 wt.% Mo₂C/Al₂O₃ catalyst, which is shown in Fig. 5.2. The IR spectrum at reaction conditions was obtained after removal of a background spectrum that was recorded after the sample was purged at 573 K for 1 h in H₂ at ambient pressure. During the reaction, the bands associated with CH₄, CO₂, H₂O, CH₃CH₂OH and CH₃OH, which appear at 3015, 2360, 1650, 1062 and 1030cm⁻¹, respectively, were observed during reaction over 5 wt.% Rb–2 wt.% Mo₂C/Al₂O₃ catalysts (Fig. 5.2).

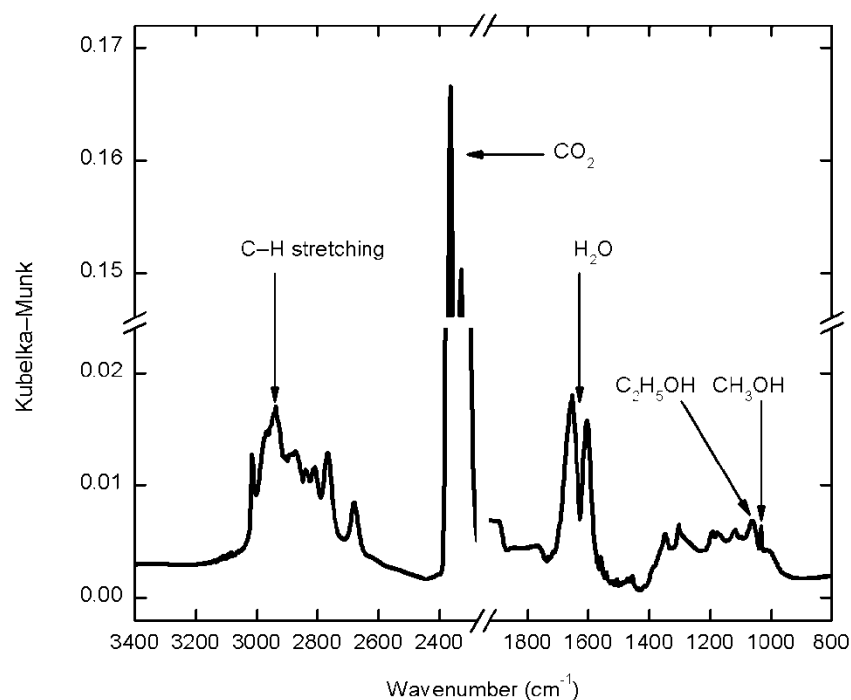


Figure 5.2: IR spectroscopy of gaseous species in CO hydrogenation at 573 K, 30 bar syngas over 5 wt.% Rb-2 wt.% Mo₂C/Al₂O₃.

The IR spectrum of adsorbed CO on unpromoted 2 wt.% Mo₂C/Al₂O₃ at room temperature after being treated at 573 K, in 30 bar syngas (H₂/CO=1) for 12 h and in 1 bar H₂ for 1 h, is shown in Fig. 5.3. The spectrum of adsorbed CO on the unpromoted Mo₂C/Al₂O₃ catalyst, which was very low in intensity, revealed two bands at 2105 and 2014 cm⁻¹, and very small features at 2173 cm⁻¹ and 1946 cm⁻¹. A sample of “carburized” Al₂O₃ pretreated with the same condition showed no feature in the IR spectrum attributed to adsorbed CO.

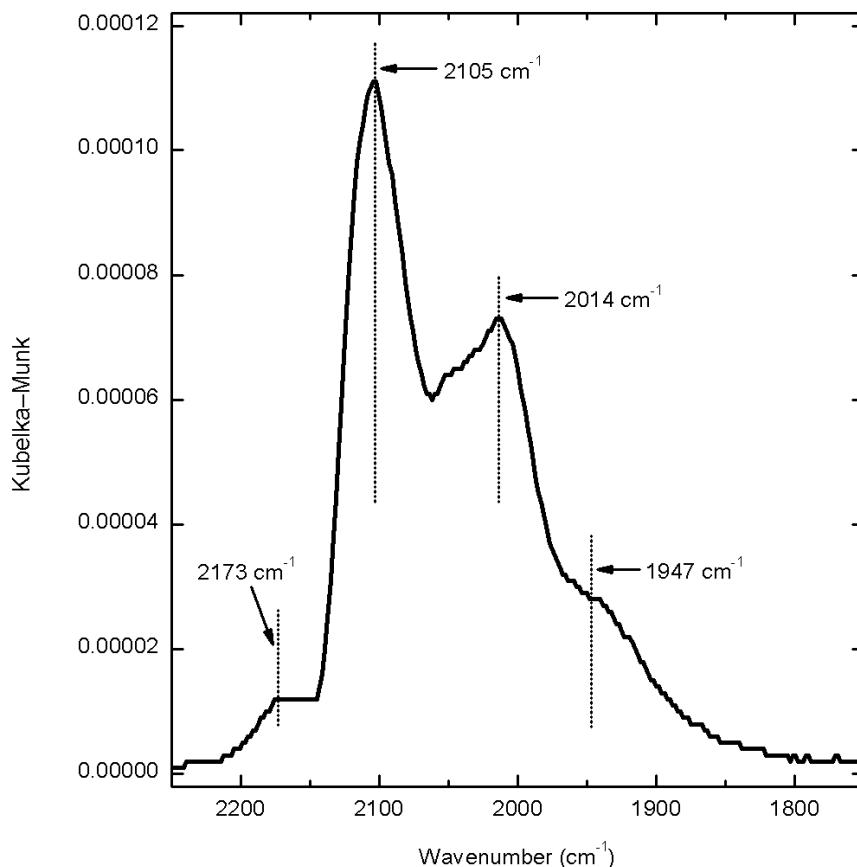


Figure 5.3: Diffuse reflectance Fourier transform spectra of adsorbed CO on 2 wt.% Mo₂C/Al₂O₃ at room temperature after being pretreated at 573 K, in 30 bar syngas (H₂/CO=1) for 12 h and in 1 bar H₂ for 1h.

The corresponding vibrational frequencies derived from DFT calculations of CO adsorbed on a reconstructed hexagonal Mo₂C(001) surface (Fig. 5.4) are shown in Table 5.1. With a low CO coverage of 0.0625 monolayer (ML), the vibrational frequency of adsorbed CO appears at 2121 cm⁻¹ and 1989 cm⁻¹ on C-top sites (Fig. 5.4b) and on Mo-top sites (Fig. 5.4c), respectively, with Mo-top sites providing a stronger binding energy (1.62 eV) than C-top sites (1.55 eV). High CO coverages typically cause a blue shift of the vibrational frequency of adsorbed CO,⁵⁵ as a result of the dipole-dipole coupling of adsorbed CO molecules.⁵⁶ The DFT calculation results also show that on the unmodified Mo₂C surface with a CO coverage of 0.25 monolayer (ML), the vibrational

frequencies of adsorbed CO on both C-top sites and on Mo-top sites were shifted to higher frequency by 20 cm^{-1} . Similar shifts in the CO band were also observed on a $\text{W}_2\text{C}(0001)$ surface by Aizawa and Otani,⁵⁷ who claimed the features belong to surface ketylidene (CCO) species formed by adsorbed CO on carbidic carbon. Nevertheless, the assignment of bands associated with CO adsorbed on Mo_2C is not straightforward, as discussed below.

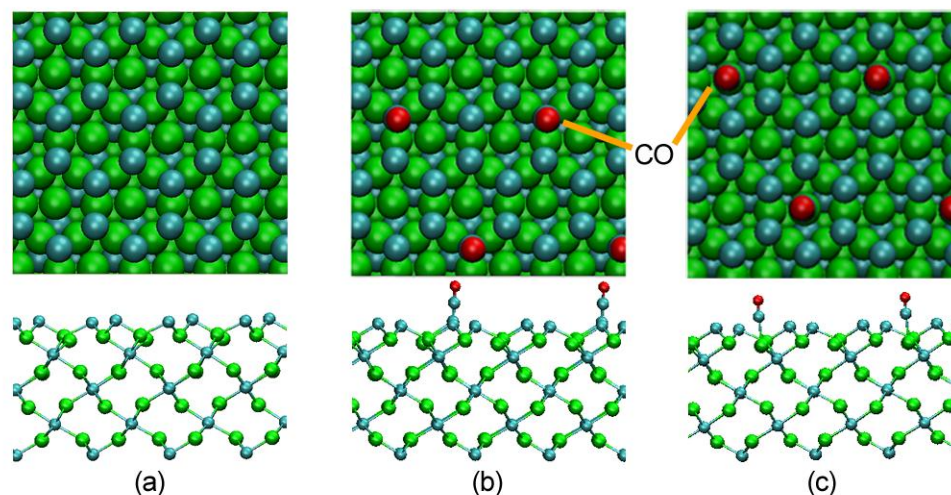


Figure 5.4: Top and side view of CO adsorption on reconstructed hexagonal Mo_2C (001) surface: (a) CO-free; (b) CO adsorbed on C top sites; (c) CO adsorbed on Mo top sites.

Table 5.1: DFT calculated CO adsorption energy and vibrational frequency on the reconstructed Mo_2C (001) surface.

CO coverage (ML)	C-top site		Mo-top site	
	Frequency (cm^{-1})	Adsorption energy (eV)	Frequency (cm^{-1})	Adsorption energy (eV)
0.0625	2121	1.55	1989	1.62
0.250	2141	1.26	2009	1.56

Aegerter et al. attributed a feature of 2178 cm^{-1} to CO adsorption on coordinatively unsaturated Mo(IV) on a passivated $\text{Mo}_2\text{C}/\text{Al}_2\text{O}_3$ catalyst after activation

in H₂.⁴⁴ Peri has also reported that CO adsorbed on Mo(IV) appears near 2190 cm⁻¹.⁵⁸ Based on these prior assignments, we attribute the minor peak at 2173 cm⁻¹ in Fig. 5.4 to CO adsorbed on oxidized molybdenum species or to the residual gaseous CO in the IR cell.

The features in the range of 2071-2054 cm⁻¹ have been assigned to linearly adsorbed CO on a clean hexagonal Mo₂C foil,⁵⁹ on carbidic Mo sites present on Mo₂C/Al₂O₃ catalysts,⁴²⁻⁴⁴ and on modeled surfaces of hexagonal Mo₂C described by DFT.^{60,61} A shoulder CO band at 2125 cm⁻¹ has also been reported when Mo₂C foil was pre-exposed to O₂.⁵⁹ Bands for linearly adsorbed CO (2015 cm⁻¹) and bridge-bonded CO (1850 cm⁻¹) were also seen by high-resolution electron energy loss spectroscopy (HREELS) on a Mo (110) single crystal with a surface carbide layer.⁶² Consistent with the XANES of bulk Mo₂C,^{22,24} the close packed structure of Mo in Mo₂C, and the similar electronegativity values of C (2.55) and Mo (2.16),⁶³ Mo in Mo₂C should be close to the metallic state so that adsorbed CO on metallic Mo would have similar vibrational frequencies to those on carbidic Mo. In fact, bands for linearly adsorbed CO on metallic Mo have been reported at 2055-2015 cm⁻¹,^{58,64} whereas the features of bridged-bonded CO are in the range of 1975–1920 cm⁻¹.⁶⁴ The asymmetric C–O stretching frequencies of ketylidene (CCO) species varied from 2130 to 2100 cm⁻¹ depending on the groups attached to the CCO structure.⁶⁵ Ketylidene has been shown to be the most stable configuration of adsorbed CO on a C-terminated Mo₂C surface by DFT.⁶⁶ Ketylidene also formed when CO was adsorbed on a W₂C surface that possessed a similar structure to Mo₂C, giving C–O stretching frequencies varying from 1954 cm⁻¹ to 2041 cm⁻¹ with increasing CO coverage.⁵⁷ Interestingly, DFT calculations suggest that ketylidene may

be involved in the initiation of the carbon chain growth process in Fisher–Tropsch synthesis over iron carbide.⁶⁷

Müller et al. studied CO adsorption on a MoS₂/Al₂O₃ catalyst, which demonstrates very similar catalytic behavior in CO hydrogenation to Mo₂C, and reported a major IR feature at 2105 cm⁻¹ for CO on Mo²⁺ along the edge of the crystallites with a shoulder at 2060 cm⁻¹ attributed to CO on less coordinated corner sites.³⁸

Since the XANES of supported Mo₂C catalysts^{22,24} suggest that the supported Mo₂C catalysts are actually oxycarbides even after syngas reaction, the 2105 cm⁻¹ peak in Fig. 5.3 may result from CO on oxycarbide Mo sites, and the secondary peak at 2014 cm⁻¹ could be attributed to CO on the Mo sites with lower valence. However, the difference between them may be also caused by different coordinative environments of Mo, such as corner vs. edge sites as described above for MoS₂ catalysts. Moreover, it is possible that the 2105 cm⁻¹ peak is from the ketenylidene-like species with CO linearly adsorbed on C-top sites over the reconstructed hexagonal Mo₂C (001) surface (Fig. 5.4), as suggested by the DFT calculation (Table 5.1).

5.3.2 Infrared spectroscopy results and DFT calculation of CO adsorption on Rb-promoted Mo₂C catalysts

Figure 5.5 summarizes the IR spectra of CO adsorbed on Mo₂C/Al₂O₃, as the weight loading of Rb increased from 0% to 10%. Upon addition of promoter, the IR band of CO at 2105 cm⁻¹ diminished and the entire band associated with CO red shifted according to the amount of Rb added. On a 10 wt.% Rb–2 wt.% Mo₂C/Al₂O₃ catalyst (Fig. 5.5e), a very weak CO band appeared at 1900 cm⁻¹. A physical mixture of Rb₂CO₃

and “carburized” Al₂O₃ (ground with mortar and pestle) showed no feature of adsorbed CO after the same pretreatment conditions.

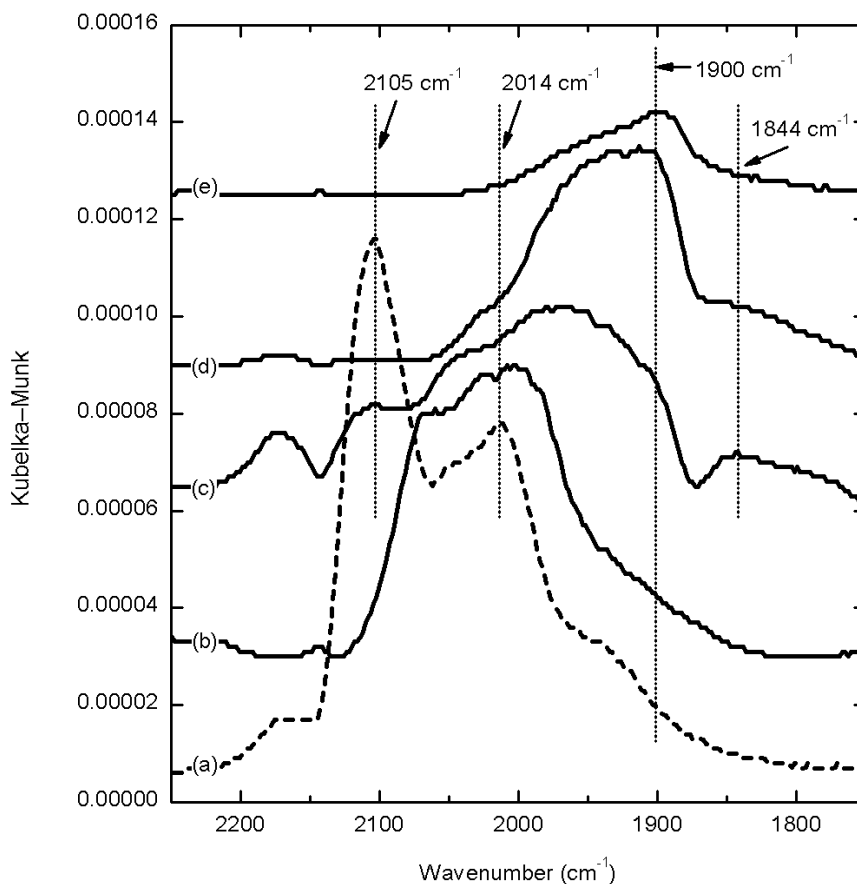


Figure 5.5: Diffuse reflectance Fourier transform spectra of adsorbed CO on samples at room temperature after being pretreated at 573 K, in 30 bar syngas (H₂/CO=1) for 12 h and in 1 bar H₂ for 1 h: (a) 2 wt.% Mo₂C/Al₂O₃; (b) 2 wt.% Rb-2 wt.% Mo₂C/Al₂O₃; (c) 5 wt.% Rb-2 wt.% Mo₂C/Al₂O₃; (d) 7.5 wt.% Rb-2 wt.% Mo₂C/Al₂O₃; (e) 10 wt.% Rb-2 wt.% Mo₂C/Al₂O₃. Spectra are offset for clarity.

In an effort to interpret the DRIFTS results, Rb and RbO were added to the reconstructed hexagonal Mo₂C(001) surface previously described by DFT (Fig. 5.1 and Fig. 5.4) and vibrational frequencies of adsorbed CO on this promoted surface were calculated. Figure 5.6 provides illustrations of Rb- and RbO-modified Mo₂C surfaces, with and without added CO. The corresponding vibrational frequencies of adsorbed CO on the Rb-modified surfaces are listed in Table 5.2. At a fixed CO coverage of

0.0625 ML, the vibrational frequencies of adsorbed CO were observed to red shift by about 34 cm^{-1} on the C-top sites (Fig. 5.6b and 10e) and by 47 cm^{-1} on the Mo-top sites (Fig. 5.6c and 5.6f) after the surface modification with either Rb or RbO. The calculated red shifts are in good agreement with the IR observations of CO adsorption on the $\text{Mo}_2\text{C}/\text{Al}_2\text{O}_3$ catalysts with increasing Rb loading (Fig. 5.5b-e). It is also instructive to compare the binding energy of CO on the promoted and unpromoted surfaces. For instance, the binding energy of CO on C-top sites (1.53 eV, Table 5.2) was almost unchanged from the unpromoted C-top sites (1.55 eV, Table 5.1) at a coverage of 0.0625 ML on the RbO-modified Mo_2C surface. However, the binding energy of CO on the Mo-top sites increased by 0.1 eV as a result of the added RbO, which might explain the decrease and eventual disappearance of the CO peak at about 2100 cm^{-1} over the Rb-promoted $\text{Mo}_2\text{C}/\text{Al}_2\text{O}_3$ (Fig. 5.5b-e). It is possible that the presence of the Rb species shifts the preferred binding from C-top to Mo-top. It should be noted that the calculations presented here are specific to one type of Mo_2C surface, and that the size, composition and morphology of the supported “ Mo_2C ” nanoparticles are more complex than the defect-free surface with long range order used for modeling.

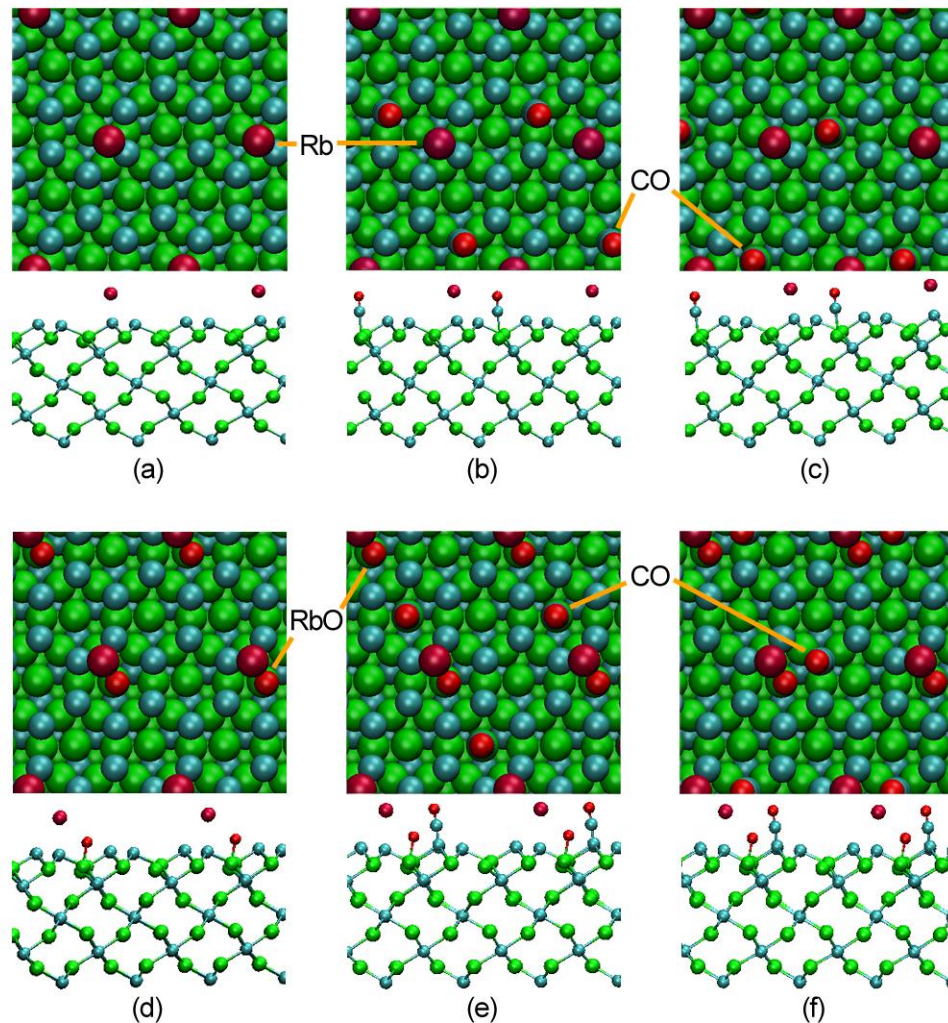


Figure 5.6: Top and side view of CO adsorption on Rb-modified reconstructed hexagonal Mo_2C (001) surface: (a) no adsorbed CO; (b) CO adsorbed on C top sites; (c) CO adsorbed on Mo top sites; and CO adsorption on RbO-modified reconstructed hexagonal Mo_2C (001) surface: (d) no adsorbed CO; (e) CO adsorbed on C top sites; (f) CO adsorbed on Mo top sites. Mo, C, O and Rb atoms are shown as green, blue, red and purple spheres, respectively.

Table 5.2: DFT calculated CO adsorption energy and vibrational frequency on the modified reconstructed Mo_2C (001) surface.

Surface	CO coverage (ML)	C-top site		Mo-top site	
		Frequency (cm^{-1})	Adsorption energy (eV)	Frequency (cm^{-1})	Adsorption energy (eV)
Rb-modified	0.0625	2088	1.41	1942	1.70
RbO-modified	0.0625	2086	1.53	1942	1.72

Bugyi and Solymosi studied the interaction of CO with clean and K-covered Mo₂C/Mo(100) surfaces by HREELS.⁶⁸ They found that CO adsorbed molecularly on the clean Mo₂C/Mo(100) surface at 140 K, giving an energy loss at 2100 cm⁻¹. Pre-adsorbed K atoms at intermediate coverages (0.5-0.8 monolayer) at 140 K led to an HREELS feature for CO at 1320–1375 cm⁻¹, attributed to a short-range interaction, while the development of features at 1670–1685 and 1860 cm⁻¹ was attributed to long-range interaction in the K–CO co-adsorbed layer.⁶⁹ They also suggested that K atoms were stabilized mainly by O atoms arising from the decomposition of CO.

Given the high oxophilicity of both Mo₂C and atomic Rb, neither bare Rb atoms nor oxygen-free Mo₂C surface can likely exist in syngas reaction conditions. Comparing the observed vibrational frequencies of CO adsorbed on Rb-promoted Mo₂C/Al₂O₃ at the surface science results for CO adsorbed on K-modified molybdenum carbide surfaces⁶⁸ at relatively low CO coverages, a similar trend is found in the shifts of peaks caused by the addition of alkali metal species. However, the shift in position is about –200 cm⁻¹ from Rb-free Mo₂C/Al₂O₃ to 10 wt.% Rb-promoted Mo₂C/Al₂O₃, which is much less than the approximately –700 cm⁻¹ shift observed on a K-modified Mo₂C/Mo(100) surface from a corresponding K-free surface.⁶⁸ This implies that the interaction of CO with cluster of molybdenum carbide was much less influenced by promoter compared to that of the extended surface in ultra high vacuum.

In summary, the shifts in CO band position in Fig. 5.5 may indicate a change of preferred binding site for CO molecules from C-top to Mo-top, as suggested by DFT calculations (Table 5.1 and 5.2), or a coverage-dependent asymmetric C–O stretching frequency of CCO species formed on the carbide surface.⁵⁷ Additionally, the shift could

also result from CO moving from a linearly adsorbed configuration to a bridge-bonded one.⁶⁴ The low frequency tail of the CO band on unpromoted Mo₂C/Al₂O₃ (Fig. 5.3, 5.5a) extends to the region around 1900 cm⁻¹, which is the position of CO on the highly promoted Mo₂C/Al₂O₃. Therefore, addition of the Rb promoter may simply deactivate the sites for CO adsorption at wavenumbers higher than 2000 cm⁻¹, leaving behind only sites with the lower characteristic frequencies. Unfortunately, at this point in time a more definitive explanation of the observed shifts in the spectrum of adsorbed CO cannot be provided.

5.3.3 Rb promoter formation mechanism on Mo₂C catalysts

Based on the experimental and computational study discussed above, a hypothesis of Rb promoter formation mechanism on the surface of Mo₂C catalysts for CO hydrogenation is proposed and sketched in Fig. 5.7. In this description, the carbide surface is first covered by oxygen atoms after surface passivation. Water in the ambient air and formed in situ during syngas reaction can dissociate on the carbide surface to form acidic hydroxyl groups, which are detrimental to alcohol selectivity. Rb atoms can replace hydrogen atoms of hydroxyl groups through a simple ion exchange reaction, forming RbO groups. Addition of Rb₂CO₃ is also needed to both neutralize surface acidity on Mo₂C and Al₂O₃ and inhibit hydrocarbon formation on Mo₂C. However, water that is added to the catalyst or generated in situ during CO hydrogenation is needed to distribute the Rb promoter across the catalyst surface. Exposure of the passivated catalysts to the syngas environment partially reduces the passivated carbide to create an active catalyst. The highly promoted catalyst has Rb on the carbide phase, which

perturbed the adsorption mode of CO on the surface and shifted product selectivity from hydrocarbons to alcohols.

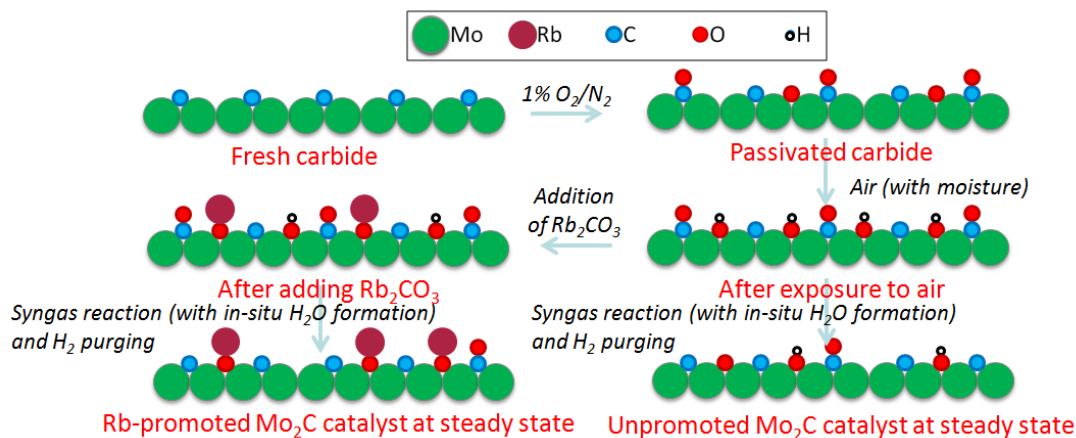


Figure 5.7: Hypothesis of Rb promoter formation mechanism on Mo_2C catalyst for alcohol synthesis.

5.4 Conclusions

the IR spectrum of CO adsorbed on the unpromoted carbide catalyst revealed features at 2105 cm^{-1} and 2014 cm^{-1} . The addition of Rb promoter to Mo_2C/Al_2O_3 gradually shifted the selectivity of the syngas reaction toward alcohols, primarily by inhibiting hydrocarbon and ether formation. The IR features of adsorbed CO on Mo_2C nanoclusters shifted substantially to lower frequencies upon addition of Rb promoter ($\sim 200\text{ cm}^{-1}$ shift from an unpromoted sample to a 10 wt.% Rb-promoted sample). Results from DFT qualitatively reproduced the trends observed by IR spectroscopy and were used to interpret the various features. Results from IR spectroscopy and DFT were used to propose a hypothesis on Rb promoter formation mechanism on Mo_2C catalyst evolution during synthesis, pretreatment and reaction. The RbO group was proposed to be the active form of Rb promoter and will be further investigated in following chapters.

5.5 References

- (1) Johnston, V. J., Chen, L., Kimmich, B. F., Chapman, J. T., Zink, J. H.; Office, U. S. P., Ed.; Celanese Corporation: U. S. , 2011.
- (2) Hess, G. *Chemical & Engineering News* **2006**, *84*, 9.
- (3) Forzatti, P.; Tronconi, E.; Pasquon, I. *Catal. Rev.-Sci. Eng.* **1991**, *33*, 109.
- (4) Wender, I. *Fuel Processing Technology* **1996**, *48*, 189.
- (5) Herman, R. G. *Catalysis Today* **2000**, *55*, 233.
- (6) Fang, K. G.; Li, D. B.; Lin, M. G.; Xiang, M. L.; Wei, W.; Sun, Y. H. *Catalysis Today* **2009**, *147*, 133.
- (7) Zaman, S.; Smith, K. J. *Catal. Rev.-Sci. Eng.* **2012**, *54*, 41.
- (8) Spivey, J. J.; Egbebi, A. *Chem. Soc. Rev.* **2007**, *36*, 1514.
- (9) Subramani, V.; Gangwal, S. K. *Energy Fuels* **2008**, *22*, 814.
- (10) Haider, M. A.; Gogate, M. R.; Davis, R. J. *Journal of Catalysis* **2009**, *261*, 9.
- (11) Avila, Y.; Kappenstein, C.; Pronier, S.; Barrault, J. *Appl. Catal. A-Gen.* **1995**, *132*, 97.
- (12) Lee, J. S.; Kim, S.; Lee, K. H.; Nam, I. S.; Chung, J. S.; Kim, Y. G.; Woo, H. C. *Appl. Catal. A-Gen.* **1994**, *110*, 11.
- (13) Christensen, J. M.; Mortensen, P. M.; Trane, R.; Jensen, P. A.; Jensen, A. D. *Appl. Catal. A-Gen.* **2009**, *366*, 29.
- (14) Surisetty, V. R.; Tavasoli, A.; Dalai, A. K. *Appl. Catal. A-Gen.* **2009**, *365*, 243.
- (15) Quarderer, G. J., Cochran, G. A.; Office, E. P., Ed.; The Dow Chemical Company: 1984.
- (16) Conway, M. M., Murchison, C. B., Stevens, R. R.; Office, U. S. P., Ed.; The Dow Chemical Company: U. S. , 1987.
- (17) Quarderer, G. J., Cochran, G. A.; Office, U. S. P., Ed.; The Dow Chemical Company: U. S., 1988.
- (18) Stevens, R. R.; Office, U. S. P., Ed.; The Dow Chemical Company: U. S., 1988.

- (19) Stevens, R. R.; Office, U. S. P., Ed.; The Dow Chemical Company: U. S., 1989.
- (20) Woo, H. C.; Park, K. Y.; Kim, Y. G.; Nam, I. S.; Chung, J. S.; Lee, J. S. *Applied Catalysis* **1991**, *75*, 267.
- (21) Xiang, M. L.; Li, D. B.; Li, W. H.; Zhong, B.; Sun, Y. H. *Fuel* **2006**, *85*, 2662.
- (22) Shou, H.; Davis, R. J. *Journal of Catalysis* **2011**, *282*, 83.
- (23) Christensen, J. M.; Duchstein, L. D. L.; Wagner, J. B.; Jensen, P. A.; Temel, B.; Jensen, A. D. *Ind. Eng. Chem. Res.* **2012**, *51*, 4161.
- (24) Shou, H.; Ferrari, D.; Barton, D. G.; Jones, C. W.; Davis, R. J. *ACS Catalysis* **2012**, *2*, 1408.
- (25) Levy, R. B.; Boudart, M. *Science* **1973**, *181*, 547.
- (26) Chen, J. G. G. *Chemical Reviews* **1996**, *96*, 1477.
- (27) Hwu, H. H.; Chen, J. G. G. *Chemical Reviews* **2005**, *105*, 185.
- (28) Jiang, M.; Bian, G. Z.; Fu, Y. L. *Journal of Catalysis* **1994**, *146*, 144.
- (29) Bian, G. Z.; Fu, Y. L.; Yamada, M. *Appl. Catal. A-Gen.* **1996**, *144*, 79.
- (30) Woo, H. C.; Kim, J. C.; Nam, I. S.; Lee, J. S.; Chung, J. S.; Kim, Y. G. *Appl. Catal. A-Gen.* **1993**, *104*, 199.
- (31) Lee, J. S.; Kim, S.; Kim, Y. G. *Top. Catal.* **1995**, *2*, 127.
- (32) Koizumi, N.; Bian, G.; Murai, K.; Ozaki, T.; Yamada, M. *J. Mol. Catal. A-Chem.* **2004**, *207*, 173.
- (33) Muramatsu, A.; Tatsumi, T.; Tominaga, H. *Bulletin of the Chemical Society of Japan* **1987**, *60*, 3157.
- (34) Verbruggen, N. F. D.; Mestl, G.; Vonhippel, L. M. J.; Lengeler, B.; Knozinger, H. *Langmuir* **1994**, *10*, 3063.
- (35) Verbruggen, N. F. D.; Vonhippel, L. M. J.; Mestl, G.; Lengeler, B.; Knozinger, H. *Langmuir* **1994**, *10*, 3073.
- (36) Fu, Y. L.; Zhao, F. G. *Catalysis Letters* **1992**, *12*, 117.
- (37) Mauge, F.; Lavalley, J. C. *Journal of Catalysis* **1992**, *137*, 69.

- (38) Muller, B.; Vanlangeveld, A. D.; Moulijn, J. A.; Knozinger, H. *Journal of Physical Chemistry* **1993**, *97*, 9028.
- (39) Travert, A.; Dujardin, C.; Mauge, F.; Cristol, S.; Paul, J. F.; Payen, E.; Bougeard, D. *Catalysis Today* **2001**, *70*, 255.
- (40) Tsyganenko, A. A.; Can, F.; Travert, A.; Mauge, F. *Appl. Catal. A-Gen.* **2004**, *268*, 189.
- (41) Travert, A.; Dujardin, C.; Mauge, F.; Veilly, E.; Cristol, S.; Paul, J. F.; Payen, E. *J. Phys. Chem. B* **2006**, *110*, 1261.
- (42) Wu, W. C.; Wu, Z. L.; Liang, C. H.; Chen, X. W.; Ying, P. L.; Li, C. *J. Phys. Chem. B* **2003**, *107*, 7088.
- (43) Wu, W. C.; Wu, Z. L.; Liang, C. H.; Ying, P. L.; Feng, Z. C.; Li, C. *Physical Chemistry Chemical Physics* **2004**, *6*, 5603.
- (44) Aegerter, P. A.; Quigley, W. W. C.; Simpson, G. J.; Ziegler, D. D.; Logan, J. W.; McCrea, K. R.; Glazier, S.; Bussell, M. E. *Journal of Catalysis* **1996**, *164*, 109.
- (45) Rasko, J.; Kiss, J. *Appl. Catal. A-Gen.* **2003**, *253*, 427.
- (46) Perdew, J. P.; Burke, K.; Ernzerhof, M. *Physical Review Letters* **1996**, *77*, 3865.
- (47) Perdew, J. P.; Burke, K.; Ernzerhof, M. *Physical Review Letters* **1997**, *78*, 1396.
- (48) Blochl, P. E. *Physical Review B* **1994**, *50*, 17953.
- (49) Kresse, G.; Joubert, D. *Physical Review B* **1999**, *59*, 1758.
- (50) Lo, R. L.; Fukui, K.; Otani, S.; Iwasawa, Y. *Surface Science* **1999**, *440*, L857.
- (51) Lo, R. L.; Fukui, K.; Otani, S.; Oyama, S. T.; Iwasawa, Y. *Japanese Journal of Applied Physics Part 1-Regular Papers Short Notes & Review Papers* **1999**, *38*, 3813.
- (52) Aizawa, T.; Hishita, S.; Tanaka, T.; Otani, S. *Journal of Physics-Condensed Matter* **2011**, *23*.
- (53) Neugebauer, J.; Scheffler, M. *Physical Review B* **1992**, *46*, 16067.
- (54) Bengtsson, L. *Physical Review B* **1999**, *59*, 12301.
- (55) Wang, J.; Castonguay, M.; Deng, J.; McBreen, P. H. *Surface Science* **1997**, *374*, 197.

- (56) Crossley, A.; King, D. A. *Surface Science* **1977**, *68*, 528.
- (57) Aizawa, T.; Otani, S. *Journal of Chemical Physics* **2011**, *135*.
- (58) Peri, J. B. *Journal of Physical Chemistry* **1982**, *86*, 1615.
- (59) Wang, J., Castonguay, M., McBreen, P. H., Ramanathan, S., Oyama, S. T. *The Chemistry of Transition Metal Carbides and Nitrides*; Springer, 1996.
- (60) Tominaga, H.; Nagai, M. *J. Phys. Chem. B* **2005**, *109*, 20415.
- (61) Shi, X.-R.; Wang, J.; Hermann, K. *The Journal of Physical Chemistry C* **2010**, *114*, 13630.
- (62) Fruhberger, B.; Chen, J. G. *Surface Science* **1995**, *342*, 38.
- (63) Haynes, W. M. *CRC Handbook of Chemistry and Physics*; Taylor & Francis, 2011.
- (64) Colaianni, M. L.; Chen, J. G.; Weinberg, W. H.; Yates, J. T. *J. Am. Chem. Soc.* **1992**, *114*, 3735.
- (65) Wagner, B. D.; Arnold, B. R.; Brown, G. S.; Lusztyk, J. *J. Am. Chem. Soc.* **1998**, *120*, 1827.
- (66) Ren, J.; Huo, C. F.; Wang, J. G.; Li, Y. W.; Jiao, H. J. *Surface Science* **2005**, *596*, 212.
- (67) Deng, L. J.; Huo, C. F.; Liu, X. W.; Zhao, X. H.; Li, Y. W.; Wang, J. G.; Jiao, H. J. *Journal of Physical Chemistry C* **2010**, *114*, 21585.
- (68) Bugyi, L.; Solymosi, F. *J. Phys. Chem. B* **2001**, *105*, 4337.
- (69) Uram, K. J.; Ng, L.; Yates, J. T. *Surface Science* **1986**, *177*, 253.

APPENDIX 5.A

STRUCTURE INFORMATION FOR RbO ADSORPTION IN THE MOST STABLE STATES ON RECONSTRUCTED MO_2C (001) SURFACE

This appendix lists the coordinates for the most stable structures of RbO adsorption on reconstructed Mo_2C (001) surface discussed in this chapter. The coordinates for the adsorbate are defined for a single supercell of a supercell of a (2×2) surface unit cell with all coordinates in Å. The shaded section of the table give the coordinates of the adsorbate; all other coordinates define the portion of the surface atoms.

Table 5.A.1: Unit cell vectors for a (2×2) surface. (in Å)

	x	y	z
a	10.536	6.072	0.000
b	0.000	12.143	0.000
c	0.000	0.000	22.296

Table 5.A.2: Fractional coordinates for RbO adsorbed on a (2×2) reconstructed Mo₂C (001) surface.

No.	Atom	x	y	z	No.	Atom	x	y	z
1	Mo	0.063089	0.090217	0.365798	54	Mo	0.495797	0.746880	0.269005
2	Mo	0.100008	0.322264	0.378958	55	Mo	0.748861	0.497545	0.269252
3	Mo	0.342899	0.076614	0.374335	56	Mo	0.739744	0.753115	0.265563
4	Mo	0.342352	0.325216	0.373295	57	Mo	0.589950	0.576846	0.166835
5	Mo	0.994632	0.001541	0.269633	58	Mo	0.591881	0.825923	0.167003
6	Mo	0.995733	0.247102	0.268674	59	Mo	0.835041	0.579365	0.161095
7	Mo	0.248655	0.997372	0.269341	60	Mo	0.836184	0.829400	0.161220
8	Mo	0.239398	0.251902	0.264994	61	Mo	0.985647	0.503486	0.059694
9	Mo	0.089984	0.076646	0.166880	62	Mo	0.485726	0.754232	0.059300
10	Mo	0.091627	0.325986	0.167335	63	Mo	0.749616	0.497060	0.060467
11	Mo	0.335845	0.079792	0.161343	64	Mo	0.749492	0.747527	0.060514
12	Mo	0.335727	0.327987	0.161349	65	C	0.264725	0.240740	0.424225
13	Mo	0.485357	0.004167	0.060367	66	C	0.415900	0.411033	0.419864
14	Mo	0.985655	0.254557	0.059731	67	C	0.168060	0.163214	0.323876
15	Mo	0.250149	0.997048	0.060805	68	C	0.167485	0.412766	0.323237
16	Mo	0.249133	0.247196	0.060524	69	C	0.415238	0.164162	0.217516
17	Mo	0.574619	0.084602	0.379322	70	C	0.417809	0.412100	0.215802
18	Mo	0.598694	0.327248	0.379249	71	C	0.163272	0.164953	0.108705
19	Mo	0.844105	0.078349	0.376573	72	C	0.163295	0.415360	0.108597
20	Mo	0.844583	0.323142	0.376968	73	C	0.417958	0.162838	0.014829
21	Mo	0.495410	0.999337	0.269313	74	C	0.417627	0.413063	0.014181
22	Mo	0.495648	0.248848	0.269200	75	C	0.761633	0.243660	0.425910
23	Mo	0.747601	0.998048	0.272218	76	C	0.916502	0.413494	0.420417
24	Mo	0.739670	0.250756	0.265513	77	C	0.665608	0.163662	0.326689
25	Mo	0.589919	0.076835	0.167041	78	C	0.670969	0.411177	0.322908
26	Mo	0.591915	0.325968	0.166980	79	C	0.913599	0.164857	0.216206
27	Mo	0.836308	0.078158	0.161224	80	C	0.917103	0.413258	0.215013
28	Mo	0.835055	0.329256	0.161188	81	C	0.663583	0.164608	0.108643
29	Mo	0.984544	0.004695	0.060312	82	C	0.663287	0.415182	0.108456
30	Mo	0.485404	0.254044	0.060392	83	C	0.917683	0.163419	0.014553
31	Mo	0.750525	0.996608	0.060605	84	C	0.916566	0.413524	0.014021
32	Mo	0.749574	0.246627	0.060519	85	C	0.263011	0.739776	0.425867
33	Mo	0.063136	0.590482	0.365579	86	C	0.415676	0.915684	0.419015
34	Mo	0.099266	0.822104	0.379119	87	C	0.169948	0.662301	0.324083
35	Mo	0.344396	0.577340	0.376680	88	C	0.169782	0.911571	0.324241
36	Mo	0.344729	0.821325	0.376266	89	C	0.414248	0.664724	0.215707
37	Mo	0.995409	0.501097	0.268547	90	C	0.417817	0.913779	0.215931
38	Mo	0.994576	0.747547	0.269550	91	C	0.162845	0.665099	0.108251
39	Mo	0.248396	0.498031	0.269015	92	C	0.162862	0.915672	0.108234
40	Mo	0.241752	0.750986	0.266267	93	C	0.417919	0.662880	0.013812
41	Mo	0.089832	0.577006	0.166745	94	C	0.417458	0.912982	0.014178
42	Mo	0.089119	0.827294	0.166754	95	C	0.762584	0.738156	0.425713
43	Mo	0.335301	0.578882	0.161295	96	C	0.918783	0.912665	0.418667
44	Mo	0.335202	0.829640	0.161373	97	C	0.670766	0.661776	0.323129
45	Mo	0.485782	0.503713	0.059258	98	C	0.665713	0.914327	0.326640
46	Mo	0.984584	0.754391	0.060236	99	C	0.913418	0.665413	0.216079
47	Mo	0.250228	0.496461	0.060774	100	C	0.915436	0.914175	0.216553
48	Mo	0.252030	0.745795	0.061359	101	C	0.663183	0.665307	0.108478
49	Mo	0.564139	0.589610	0.365819	102	C	0.663536	0.915537	0.108599
50	Mo	0.598743	0.818115	0.379368	103	C	0.917573	0.662632	0.014513
51	Mo	0.844604	0.576054	0.376924	104	C	0.918085	0.912794	0.014175
52	Mo	0.844232	0.821369	0.376494	105	O	0.605458	0.071379	0.457099
53	Mo	0.495841	0.500904	0.268975	106	Rb	0.427130	0.241772	0.537305

CHAPTER 6

INVESTIGATION OF ALKALI PROMOTER'S EFFECT ON CO INSERTION ON MO₂C CATALYSTS

6.1 Introduction

Industrial applied catalysts are often complex materials consisting of catalysts, supports and promoters. Among them, catalyst promoters play important roles in optimizing the catalyst performance of reactions in terms of either activity or selectivity. Although they have been widely used for a long time, the mechanism of their impacts on catalytic reactions are still not well understood. This is partly due to the complexity of the catalyst system, where promoters are often applied in low concentrations, making them very difficult to be observed experimentally. Also, catalyst promoters may only influence a few intermediate steps in a multi-step reaction.

In general, catalyst promoters can be divided into structural promoters and electronic promoters. Structural promoters enhance catalytic performance by stabilizing the active phase of the catalyst. For example, small amounts of oxides like CaO and Al₂O₃ are used in iron based ammonia synthesis catalysts to stabilize high surface area of iron catalysts.¹ On the other hand, electronic promoters are often suggested to modify the catalyst structure by transferring electrons to or from a catalyst surface. The most widely used electronic promoters are alkalis such as K or Cs. Generally, when these promoters adsorb on a catalyst surface they become strongly polarized and therefore create a dipole on the surface, which can interact with reaction intermediates on the surface and potential

influence the catalyst reactivity. One example of an electronic promoter is the K promoter used in ammonia synthesis. It was suggested that the opposite dipole moments between a K promoter and the transition state structure of N_2 increased the reaction activity since it lowers the activation energy of N_2 dissociation.²

For alcohol synthesis from syngas, as shown in previous chapters, we have found RbO as the active form of an alkali promoter and also found that CO insertion is the selectivity determining step responsible for the selectivity for hydrocarbons relative to alcohols. Therefore, in this chapter, we investigate the effect of RbO on CO insertion on a representative Mo_2C surface. We perform DFT calculations to locate the transition state of CO insertion by the Nudged Elastic Band method. Charge assignment on all the relevant structures in CO insertion, including CO, CH_3 , CH_3CO , the $[CH_3-CO]$ transition state and RbO are made by the Density Derived Electrostatic and Chemical (DDEC) charge method. It is found that RbO generated an opposite dipole field to the transition state $[CH_3-CO]$ structure on Mo_2C surface. This could effectively lower the activation energy of CO insertion and therefore shift the overall reaction selectivity from hydrocarbons to alcohols.

6.2 Computational methods

Plane wave DFT calculations were performed with the Vienna *ab initio* simulation package (VASP). We employed the revised Perdew-Burke-Ernzerhof (rPBE) generalized gradient functional^{3,4} along with the projector augmented wave (PAW)^{5,6} method to describe ionic cores. A plane wave expansion with a cutoff of 400 eV was used for all calculations. Geometries were relaxed using a conjugate gradient algorithm until the forces on all unconstrained atoms were less than 0.03 eV/Å.

The surface structure of the molybdenum carbide catalyst modeled is based on the reconstructed C-terminated hexagonal α -Mo₂C(001) surface discussed in Chapter 3, which is illustrated in Fig. 6.1. In Chapter 3, by comparing the surface free energy and the adsorption energy of alkali metal (K and Rb) atoms for different low-Miller-index surfaces of Mo₂C, the Mo₂C(001) surface was found to be one of the major surfaces of Mo₂C particles as well as have the greatest affinity and dipole moment for Rb atoms. This surface is also known to favor a reconstruction in the absence of adsorbates,⁷⁻⁹ which results in both Mo-top and C-top sites for CO adsorption. In spite of potential support effects, the behavior of bulk Mo₂C catalysts and Mo₂C catalysts^{10,11} and Mo₂C catalysts on various supports (MgO,¹² α -Al₂O₃,¹³ and mixed-phase Al₂O₃) is similar, which suggests that the actual sites on various Mo₂C catalysts for CO hydrogenation would have a similar configuration. Given all the factors mentioned above, Mo₂C (001) was chosen as a representative surface for modeling.

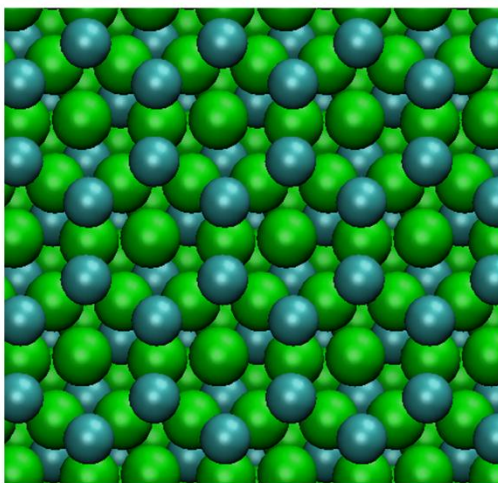


Figure 6.1: Top view of reconstructed hexagonal α -Mo₂C (001) surface. Mo (C) atoms are shown as green (blue) spheres.

A $6 \times 6 \times 1$ Monkhorst-Pack k-point mesh was used for (1×1) surface unit cell, which was sufficient to give well-converged results. For calculations on a (2×2) surface unit cell, the number of k-points in the Monkhorst-Pack meshes was reduced to $3 \times 3 \times 1$.

Geometries and energies for gas phase species were calculated using supercells equivalent to those for the largest slab calculations. When examining adsorption, molecules were placed on only one side of the slab. Dipole corrections were therefore applied in computing all of the energies reported below.^{14,15} The adsorption energy, $E_{\text{adsorption}}$, of an atom or molecule was defined by

$$E_{\text{adsorption}} = (E_{\text{surface}} + E_{\text{adsorbate}}) - E_{\text{total}}, \quad (6.1)$$

where E_{total} is the total energy of the system containing the adsorbed species, E_{surface} is the total energy for the optimized bare surface, and $E_{\text{adsorbate}}$ is the total energy for the adsorbate in the gas phase. With this definition, positive adsorption energies correspond to energetically favored states. Adsorbate coverages were defined by considering a surface with an adsorbed species on every surface molybdenum atom to have a coverage of 1 monolayer (ML). This means that placing one adsorbate in a 1×1 unit cell gives a coverage of 0.25 ML.

DDEC charges were computed using the codes available at ddec.sourceforge.net as described by Manz and Sholl using the DDEC/c3 method.^{16,17}

6.3 Results and Discussion

6.3.1 Adsorption of RbO promoter and CO insertion reaction intermediates on Mo₂C (001) surface

The adsorption of the RbO promoter and reaction intermediates CO, CH₃, and CH₃CO have been investigated in Chapter 4 and Chapter 5 previously. The most stable adsorption geometries are shown in Figs. 6.2-6.5.

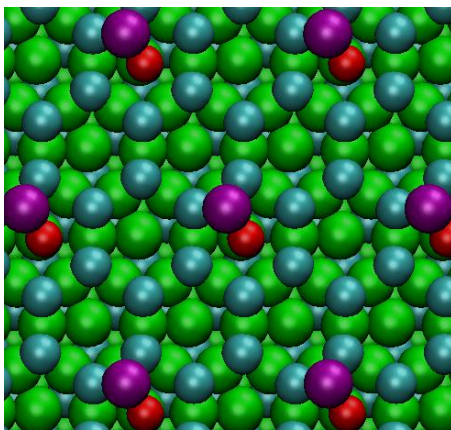


Figure 6.2: Top view of RbO adsorbed on (2x2) Mo₂C (001) surface. Mo, C, O and Rb atoms are shown as green, blue, red and purple spheres, respectively.

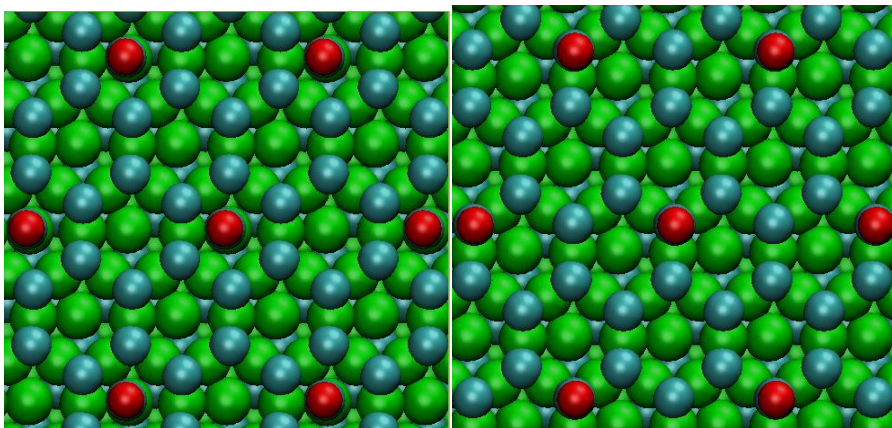


Figure 6.3: Top view of CO adsorbed on Mo top (left) and C top (right) on (2x2) Mo₂C (001) surface. Mo, C, O atoms are shown as green, blue, red spheres, respectively.

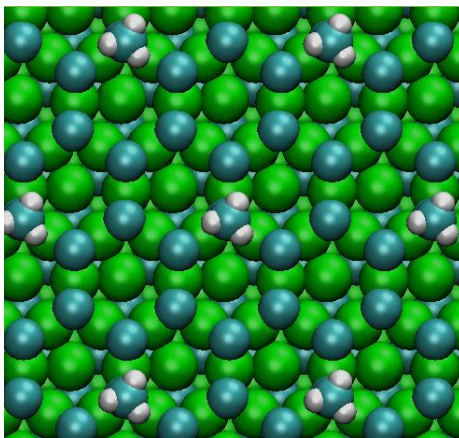


Figure 6.4: Top view of CH_3 adsorbed on (2×2) Mo_2C (001) surface. Mo, C, H atoms are shown as green, blue, white spheres, respectively.

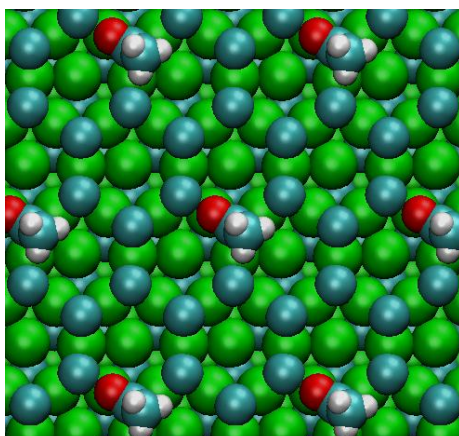


Figure 6.5: Topview of CH_3CO adsorbed on (2×2) Mo_2C (001) surface. Mo, C, O and H atoms are shown as green, blue, red and white spheres, respectively.

As shown in these figures, RbO adsorbs on in a way that the O atom prefers a Mo top site and the Rb atom favors the three-fold site among two surface carbon and one surface Mo. CO adsorbs most stably on a Mo top site, although its adsorption on a C top site is only slightly unfavorable. In general, CO adopts an O-top-C-down geometry on both Mo top and C top sites. Finally, both CH_3 and CH_3CO prefer a C top site, as shown in Fig. 6.5. To examine the effect of RbO on the adsorptions of CO, CH_3 , and CH_3CO ,

the cases of RbO co-adsorbed with these three intermediates were investigated by DFT calculations. The most stable adsorption geometries for these co-adsorbed state are shown below in Figs. 6.6-6.8.

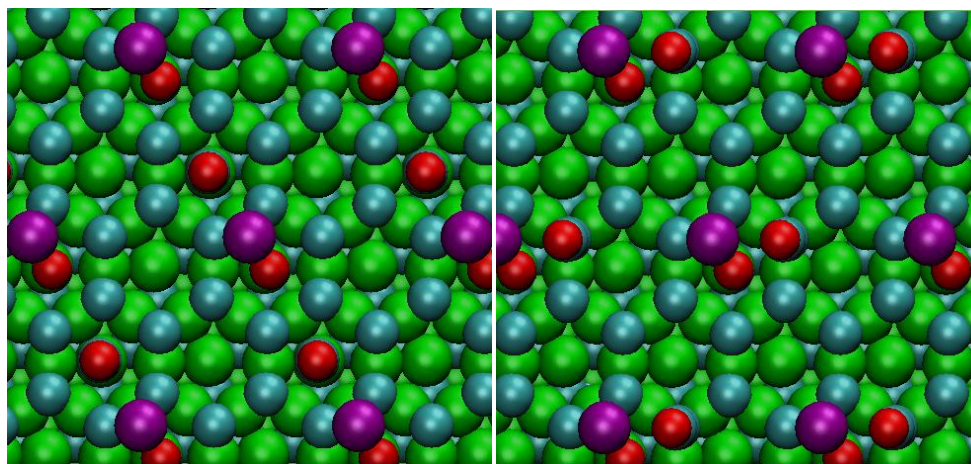


Figure 6.6: Top view of RbO co-adsorbed with CO on Mo top (left) and C top (right) sites on (2x2) Mo₂C (001) surface. Mo, C, O and Rb atoms are shown as green, blue, red and purple spheres, respectively.

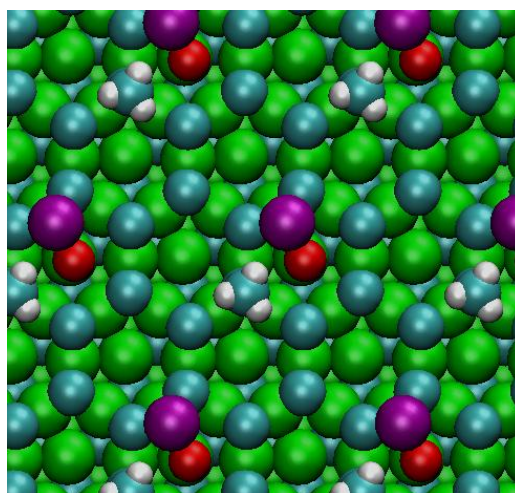


Figure 6.7: Top view of RbO co-adsorbed with CH₃ on (2x2) Mo₂C (001) surface. Mo, C, O, H and Rb atoms are shown as green, blue, red, white and purple spheres, respectively.

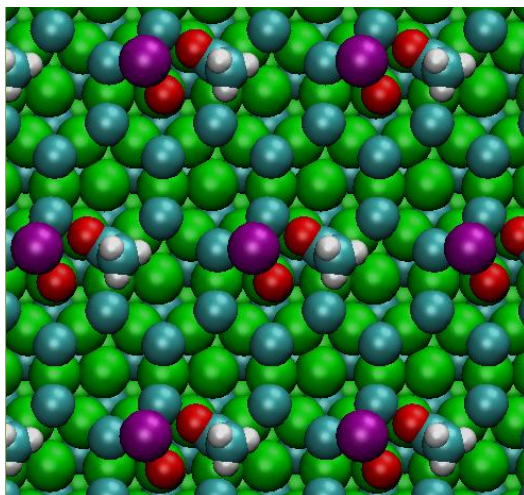


Figure 6.8: Top view of RbO co-adsorbed with CH₃CO on (2x2) Mo₂C (001) surface. Mo, C, O, H and Rb atoms are shown as green, blue, red, white and purple spheres, respectively.

As shown in these figures, co-adsorbing RbO with CO, CH₃ and CH₃CO does not change their adsorption geometries significantly. This is consistent with the concept mentioned in section 6.1 that the interactions between alkali promoters and other adsorbates are most likely from the dipole fields they created rather than forming direct chemical bonds. We have calculated the changes of CO's adsorption energy upon RbO addition in Chapter 5, and found that RbO promotes CO adsorption on both Mo top and C top sites, with increased adsorption energy of 0.14 eV/molecule (Mo top) and 0.03 eV/molecule (C top). To further test this hypothesis, we performed charge assignments on the adsorption of RbO and these intermediates shown in the above figures.

6.3.2 Charge analysis of RbO promoter and CO insertion reaction intermediates on Mo₂C (001) surface

As mentioned in section 6.2, we used the Density Derived Electrostatic and Chemical (DDEC) charge method to assign the charges in this chapter.¹⁶ Compared to the conventional charge assignment methods, like Bader analysis, DDEC is an alternative

approach developed recently and has shown to perform well for a wide range of materials including isolated molecules, porous solids and solid surfaces. We will show in Chapter 7 that DDEC performs better than Bader analysis for several Mo-containing materials used in XANES experiments. Therefore, the charge analysis on the adsorption cases was performed by the DDEC method, as shown below in Table 6.1.

Table 6.1: DDEC charges of RbO promoter and CO insertion reaction intermediates on Mo₂C (001) surface.

Adsorbate	Atoms	DDEC Charge
RbO	Rb	0.94
	O	-0.58
	Net	0.36
CO on Mo top	C	0.21
	O	-0.14
	Net	0.07
CO on C top	C	0.72
	O	-0.28
	Net	0.44
CH ₃	C	-0.16
	H	0.12
	H	0.11
	H	0.11
	Net	0.18
CH ₃ CO	C	0.69
	O	-0.52
	C(methyl)	-0.49
	H	0.16
	H	0.17
	H	0.14
	Net	0.15

RbO is found to donate electrons to the catalyst surface as indicated by a net charge of 0.36. As expected, Rb atom carries a charge of 0.94, as the alkali atom can

easily lost its outmost valence electron to the O atom beneath, which has a charge of -0.58. CO adsorbed on either Mo top and C top sites carries a positive charge on carbon, a negative charge on oxygen, and contributes electrons to the Mo_2C surface. As mentioned earlier, RbO is found to enhance the adsorption of CO on both sites. This can be explained qualitatively by the opposite dipole field created by $\text{C}(+)\text{O}(-)$ and $\text{Rb}(+)\text{O}(-)$, as depicted in Fig. 6.9.

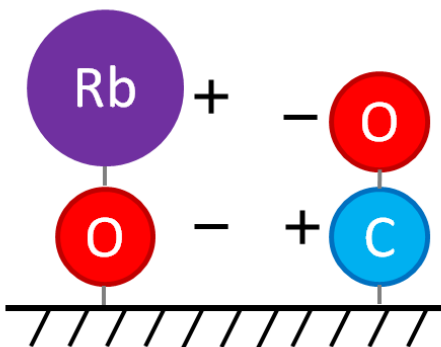


Figure 6.9: Schematic of RbO co-adsorbed with CO on Mo_2C surface. C, O and Rb atoms are shown as blue, red and purple spheres, respectively.

For CH_3 and CH_3CO , similar analysis was made. The carbon atom in the methyl group was found to have a negative charge while hydrogen atoms are positively charged. CO group in CH_3CO has a similar charge configuration as the adsorbed CO, where carbon carries a positive charge and oxygen carries a negative charge. This charge analysis suggests that RbO will destabilize the CH_3 adsorption due to dipole-dipole repulsion. On the other hand, with opposite dipole field, CH_3CO will be stabilized by RbO. Schematics of the charge configurations are shown in Fig. 6.10 and 6.11.

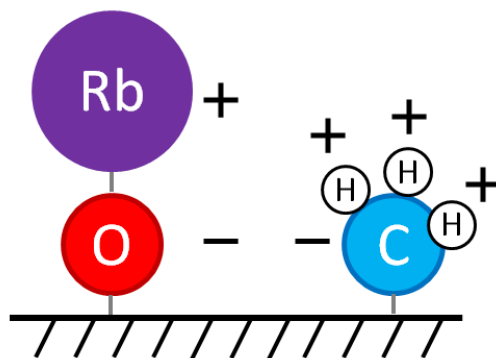


Figure 6.10: Schematic of RbO co-adsorbed with CH₃ on Mo₂C surface. C, O, H and Rb atoms are shown as blue, red, white and purple spheres, respectively.

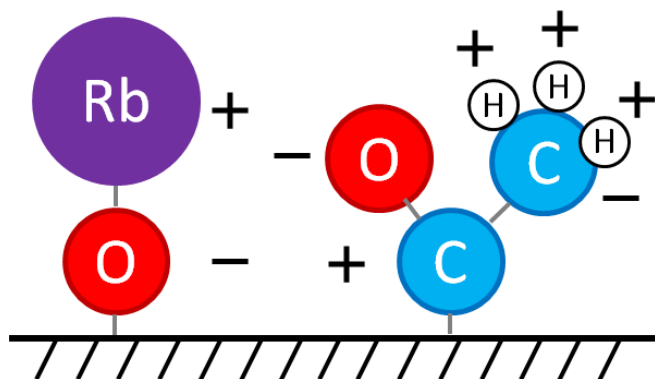


Figure 6.11: Schematic of RbO co-adsorbed with CH₃CO on Mo₂C surface. C, O, H and Rb atoms are shown as blue, red, white and purple spheres, respectively.

6.3.3 Investigation of the effect of RbO on the transition state of CO insertion

reaction on Mo₂C (001) surface

In order to analyze the effect of RbO on CO insertion, the transition state of the CO insertion reaction needs to be located. This can be achieved by a Nudged Elastic Band (NEB) calculation. Since the NEB method requires the optimized structures of the initial and final states of a reaction route, we first examined the adsorption geometry of

CO co-adsorbed with CH₃ as the initial state and CH₃CO as the final state. Based on the most stable adsorption geometry of these three molecules determined in section 6.3.1, where CO adsorbed on both Mo and C top sites, CH₃ adsorbed C top site and CH₃CO adsorbed on C top site, a plausible reaction route has both CO and CH₃ starting from adjacent C top sites, CH₃ moving towards CO, creating a bond between their carbon atoms, and finally forming CH₃CO on the C top site. The initial and final state are shown below in Figs. 6.12 and 6.13.

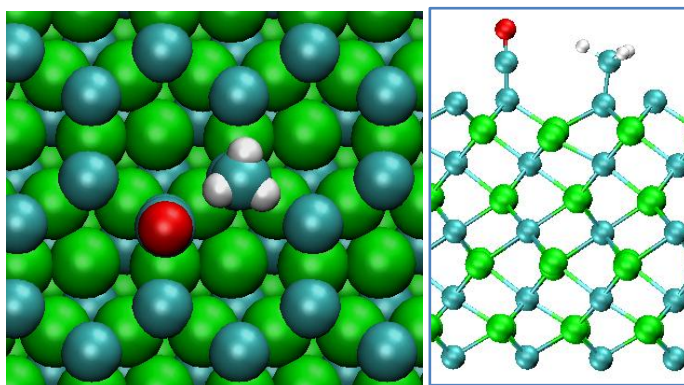


Figure 6.12: Top and side view of CO co-adsorbed with CH₃ on two adjacent C top site on Mo₂C (001) surface as the initial state of CO insertion reaction route. Mo, C, O and H atoms are shown as green, blue, red and white spheres, respectively.

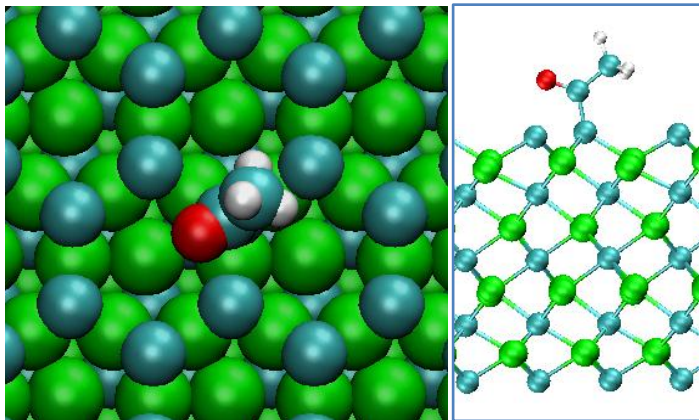


Figure 6.13: Top and side view of CH_3CO on C top site on Mo_2C (001) surface as the final state of CO insertion reaction route. Mo, C, O and H atoms are shown as green, blue, red and white spheres, respectively.

Based on the structures of the starting and ending states, an NEB calculation was performed. The potential energy along the reaction coordinates was computed and shown in Fig. 6.14. The transition state found in the calculations is shown in the figure above the energy curve with an activation energy of 1.41 eV, which is in reasonable agreement with the approximate value (1.16 eV) from the BEP relation used in Chapter 4. We further assigned charges to this transition state $[\text{CH}_3\text{CO}]$ structure, as shown in Table 6.2.

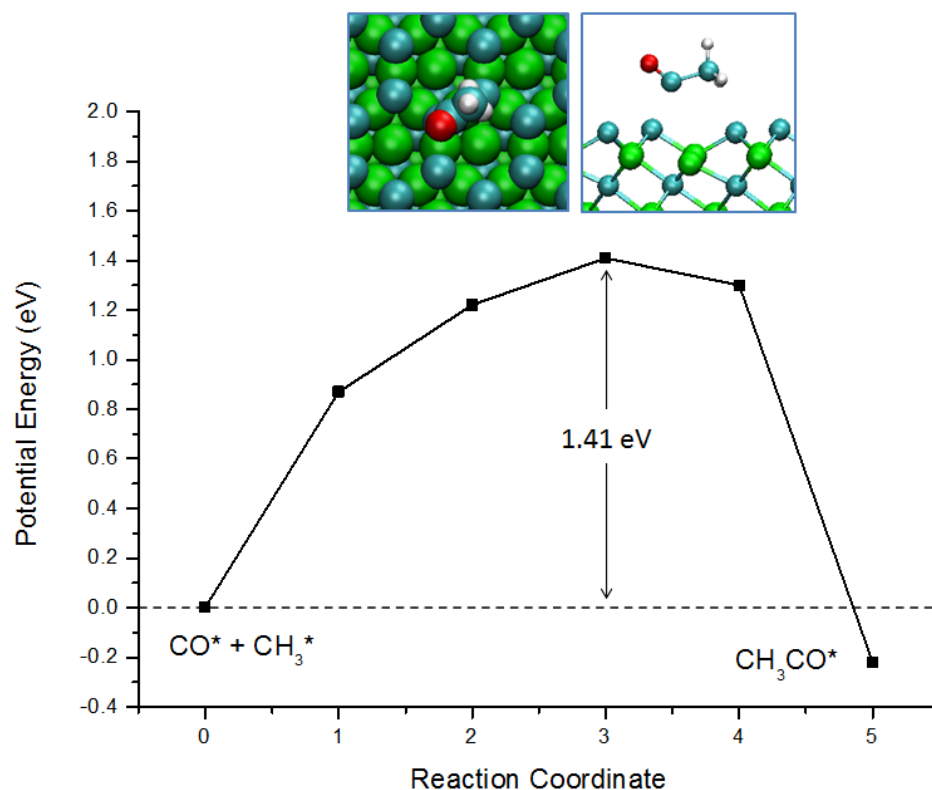


Figure 6.14: Potential energy along the reaction coordinates of CO insertion on Mo₂C (001) surface with the top and side view of the transition state [CH₃CO] structure. Mo, C, O and H atoms are shown as green, blue, red and white spheres, respectively.

Table 6.2: DDEC charges of the transition state [CH₃CO] structure of the CO insertion on Mo₂C (001) surface

Adsorbate	Atoms	DDEC Charge
Transition state [CH ₃ CO]	C	0.53
	O	-0.28
	C(methyl)	-0.43
	H	0.16
	H	0.20
	H	0.19
	Net	0.37

Similar to the adsorbed CH₃CO, the transition state [CH₃CO] structure also carries positive charges on carbon atom of CO group and hydrogen atoms of methyl

group and negative charges on oxygen atom of CO group and carbon atom of methyl group. The dipole field it created has an opposite direction to the dipole field of RbO promoter, as shown in Fig. 6.15. It is expected RbO will stabilize the transition state $[\text{CH}_3\text{CO}]$ structure, enhance the CO insertion on Mo_2C catalyst, and therefore shift the syngas reaction selectivity from hydrocarbons to alcohols.

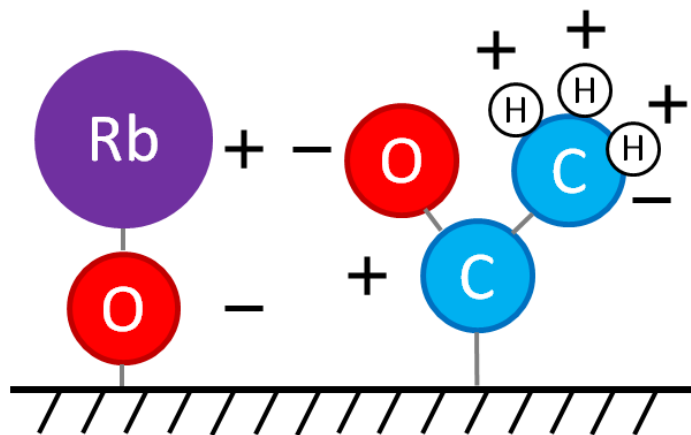


Figure 6.15: Schematic of RbO co-adsorbed with the transition state $[\text{CH}_3\text{CO}]$ structure on Mo_2C surface. C, O, H and Rb atoms are shown as blue, red, white and purple spheres, respectively.

6.4 Conclusions

In this chapter, we investigated the CO insertion on Mo_2C at a detailed level with the NEB calculation. The transition state of the CO insertion is located with an activation energy of 1.41 eV, close to the approximated value from the BEP relation used previously. We performed charge assignments on RbO promoter, reaction intermediates and the transition state of the CO insertion, and found that RbO promoter carries an opposite dipole field to the transition state of CO insertion. Therefore, it is suggested that RbO promoter can accelerate the CO insertion mechanism on Mo_2C catalyst and shift the syngas reaction selectivity from hydrocarbons to alcohols.

6.5 References

- (1) Chorkendorff, I., Niemantsverdriet, J. W. *Concepts of Modern Catalysis and Kinetics*; WILEY-VCH: Weinheim, 2003.
- (2) Mortensen, J. J.; Hansen, L. B.; Hammer, B.; Norskov, J. K. *Journal of Catalysis* **1999**, *182*, 479.
- (3) Perdew, J. P.; Burke, K.; Ernzerhof, M. *Physical Review Letters* **1996**, *77*, 3865.
- (4) Perdew, J. P.; Burke, K.; Ernzerhof, M. *Physical Review Letters* **1997**, *78*, 1396.
- (5) Blochl, P. E. *Physical Review B* **1994**, *50*, 17953.
- (6) Kresse, G.; Joubert, D. *Physical Review B* **1999**, *59*, 1758.
- (7) Lo, R. L.; Fukui, K.; Otani, S.; Iwasawa, Y. *Surface Science* **1999**, *440*, L857.
- (8) Lo, R. L.; Fukui, K.; Otani, S.; Oyama, S. T.; Iwasawa, Y. *Japanese Journal of Applied Physics Part 1-Regular Papers Short Notes & Review Papers* **1999**, *38*, 3813.
- (9) Aizawa, T.; Hishita, S.; Tanaka, T.; Otani, S. *Journal of Physics-Condensed Matter* **2011**, *23*.
- (10) Woo, H. C.; Park, K. Y.; Kim, Y. G.; Nam, I. S.; Chung, J. S.; Lee, J. S. *Applied Catalysis* **1991**, *75*, 267.
- (11) Xiang, M. L.; Li, D. B.; Li, W. H.; Zhong, B.; Sun, Y. H. *Fuel* **2006**, *85*, 2662.
- (12) Shou, H.; Davis, R. J. *Journal of Catalysis* **2011**, *282*, 83.
- (13) Shou, H.; Ferrari, D.; Barton, D. G.; Jones, C. W.; Davis, R. J. *ACS Catalysis* **2012**, *2*, 1408.
- (14) Neugebauer, J.; Scheffler, M. *Physical Review B* **1992**, *46*, 16067.
- (15) Bengtsson, L. *Physical Review B* **1999**, *59*, 12301.
- (16) Manz, T. A.; Sholl, D. S. *Journal of Chemical Theory and Computation* **2010**, *6*, 2455.
- (17) Manz, T. A.; Sholl, D. S. *Journal of Chemical Theory and Computation* **2012**.

CHAPTER 7

ON THE RELATIONSHIP BETWEEN MO K EDGE ENERGIES AND DFT COMPUTED PARTIAL CHARGES

7.1 Introduction

Partial charges in solid materials form due to the asymmetrical distribution of electrons between bonded atoms. Although the concept of a partial charge is not a fundamental property, it often serves as a simple quantity to represent the tendency of electrons among nearby nuclei and thus can provide important information to understand the chemical reactivity of materials. Experimentally, the distribution of partial charges in solid materials can be inferred by several spectroscopic methods, including X-ray Photoelectron Spectroscopy (XPS) and X-ray Absorption Near-Edge Spectroscopy (XANES). While XANES can be used to characterize the structure or coordination of compounds, it is most often employed to quantify and compare absorption edge energies of similar materials.¹⁻¹⁰ Specifically, absorption edge energies, as found using XANES, can be correlated with partial charge distributions in solids.^{5,11-14}

Partial charges can be also determined from quantum chemistry calculations. However, no unique solution to the task of assigning partial charges to atoms exists because the net electron density of a material can be assigned to individual atoms in a number of ways. Although a wide variety of charge assignment methods exist for molecular systems (Mulliken charges, Hirshfeld charges etc.), only a small number of these methods are suitable for application to dense solids.¹⁵ Perhaps the most widely used

charge assignment method for dense solids is Bader charges. Bader analysis, which was first proposed in the 1980s, assigns the electron density in well-defined volumes around each atom to the atom.^{16,17} Efficient implementations of this approach exist for use with plane wave DFT calculations.¹⁸⁻²¹ A disadvantage of the Bader approach is that the resulting charges do not accurately reproduce the electrostatic potential outside the electron distribution.¹⁵ An alternative approach termed Density Derived Electrostatic and Chemical (DDEC) charges has recently been developed and shown to perform well for a wide range of solid materials as well as for isolated molecules, porous solids, and solid surfaces.^{15,22-25}

In this chapter, we examine the empirical correlation between partial charges assigned using the DDEC and Bader approaches with XANES measurements of the Mo K-edge for a series of reference materials. Both quantum chemistry approaches correlate considerably better with the experimental data than formal oxidation states, so our data provide a clear example where the use of formal oxidation states in characterizing solids is problematic. The charges determined with the DDEC approach show a closer correlation with the experimental data than Bader charges. Our results suggest that application of DDEC charges gives a useful method for assigning the point charges on atoms in dense solids from quantum chemistry calculations. In addition, our data indicate that XANES edge energy measurements can aid in determining the partial charges on atoms in a solid by comparison with a series of reference compounds.

7.2 Computational and experimental methods

XANES data were collected at beamlines X-18B at the National Synchrotron Light Source, Brookhaven National Laboratory. The photon ring was operated at 2.8 GeV and 300 mA. Data were obtained in transmission mode at the Mo *K* edge (20 keV) with a spot size of 0.5 mm by 3 mm. MoS₂ (98.5%, Acros), Mo₂C (99.5%, Aldrich), MoO₂ (99%, Aldrich), MoO₃ (99.99%, Aldrich), and Rb₂MoO₄ (Alfa Aesar) samples were ground into fine powders and spread over Kapton tape. The sample-covered tapes were layered and placed in the path of the beam until an absorption thickness of approximately 1 was reached. Three scans from 19700 eV to 21220 eV were collected for each sample. Each dataset was collected simultaneously with a Mo foil (0.015 mm, 99.9%, Goodfellow) reference, and all datasets were later aligned according to that reference.

Plane wave DFT calculations were performed with the Vienna *ab initio* simulation package (VASP).^{19,26-28} We employed the revised Perdew-Burke-Ernzerhof (rPBE) generalized gradient functional^{29,30} along with the projector augmented wave (PAW)^{31,32} method to describe ionic cores. A plane wave expansion with a cutoff of 400 eV was used for all calculations. A 6×6×6 Monkhorst-Pack *k*-point mesh was used for all structures, which was sufficient to give well converged results.

Point charges were calculated from DFT calculations using the atomic spacings and crystal structures obtained from the Inorganic Crystal Structure Database (ICSD).^{33,34} DDEC charges were computed using the codes available at ddec.sourceforge.net as described by Manz and Sholl using the DDEC/c3 method.^{15,35} Bader charges were computed using the software developed by Henkelman and co-workers.^{18,20,21}

7.3 Results and Discussion

A series of molybdenum-containing materials was chosen for this study to establish the relationship between partial charge and formal oxidation state. Ordered from most reduced to most oxidized, based on formal oxidation states, the samples were: Mo foil (Mo^0), Mo_2C (Mo^{2+}), MoS_2 (Mo^{4+}), MoO_2 (Mo^{4+}), Rb_2MoO_4 (Mo^{6+}) MoO_3 (Mo^{6+}). These materials are also listed in Table 7.1. Several of these molybdenum materials are commonly used as catalysts or catalyst precursors.³⁶⁻⁴²

DFT calculations were performed for each material with the atomic geometries obtained from the Inorganic Crystal Structure Database (ICSD). For species that have entries from multiple space groups (MoS_2 and MoO_3), all space group representations were considered. The lattice parameters for these calculations are summarized in Table 7.1. To test the effect of structural relaxation on the computational results, we calculated and compared the charges of MoO_2 for both unrelaxed and relaxed structures. After structural relaxation, the DFT optimized MoO_2 had lattice parameters $a = 5.5962 \text{ \AA}$, $b = 4.9080 \text{ \AA}$, $c = 5.6598 \text{ \AA}$. The computed DDEC charge of Mo in the unrelaxed (relaxed) MoO_2 was 1.78 (1.86). This suggests that the Mo charges in these dense materials (MoO_2 , MoO_3 , Mo_2C , Rb_2MoO_4) are insensitive to lattice optimization by DFT. However, for MoS_2 , a layered structure where van der Waals interaction is involved, DFT methods without dispersion corrections such as the functional we have used in this work are not suitable for geometry optimization. On this basis, all the charge results below were calculated with unrelaxed structures using experimentally-observed crystal structures. This example also illustrates that Mo atoms do not precisely follow the pattern expected based on formal charges, which would predict the presence of Mo^{4+} in MoO_2 .

Table 7.1: Structural information and DFT computed charges for Mo containing materials. Charges are given in unit of e.

Species	ISCD code	Space Group	Lattice parameters (Å)			Computed Charges	
			A	b	c	DDEC	Bader
Mo ₂ C	43322 ⁴³	Pbcn	4.724	6.004	5.199	0.57	0.66
MoS ₂	644257 ⁴⁴	R3mH	3.163	3.163	18.370	0.23	1.09
	95570 ⁴⁵	P63/mmc	3.168	3.168	12.322	0.21	1.09
MoO ₂	152316 ⁴⁶	P121/c1	5.6060	4.8566	5.6238	1.78	1.88
MoO ₃	151751 ⁴⁷	Pbma	13.8649	3.6976	3.9629	2.38	2.36
	152312 ⁴⁶	Pbnm	3.9614	13.8621	3.6970	2.36	2.29
Rb ₂ MoO ₄	24904 ⁴⁸	C12/m1	12.821	6.253	7.842	2.12	2.13

We also used MoO₂ to probe the influence of the exchange-correlation functional used in DFT on the resulting point charges. For MoO₂, the computed Mo charge with the rPBE (PW91) GGA functional was 1.78 (1.80). This is consistent with the observation of Manz and Sholl for small molecules that DDEC charges changed little in calculations that used GGA-DFT, DFT with a hybrid functional (B3LYP), and higher level quantum chemistry calculations (CCSD and CAS).¹⁵ All of the results below are based on DDEC point charges assigned based on DFT calculations with the rPBE functional.

The DDEC charges and Bader charges for Mo in each compound are summarized in Table 7.1. For the species having multiple space group representations (MoS₂ and MoO₃), we obtained very similar charges from the different representations. We therefore use charges averaged over these representations in the following sections.

The results from the DFT computed charges and XANES experiments are summarized in Table 7.2. For comparison, the formal oxidation states of Mo in these compounds are also listed. It is clear that the DDEC charges are poorly correlated with the formal oxidation states. The two materials that nominally contain Mo⁴⁺, MoS₂ and MoO₂, have DDEC Mo charges that differ by a factor of ~8. The Bader charges show a trend that is more similar to the formal oxidation states, with Mo in MoS₂ being assigned

a charge significantly larger than that in Mo₂C. Although the Bader charges have a trend that is similar to the formal oxidation states, all of the Bader charges are considerably smaller than the formal oxidation states.

Table 7.2: Results from DFT computations and XANES experiments. The DFT results were averaged charges from results for different space groups in Table 7.1. The edge energies from XANES are determined from the position at half step height.

Species	DDEC Mo Charge	Bader Mo Charge	Formal Oxidation State	Mo <i>K</i> -edge Energy (eV)
Mo	0.00	0.00	0	20005.3
MoS ₂	0.22	1.09	+4	20006.5
Mo ₂ C	0.57	0.66	+2	20006.9
MoO ₂	1.78	1.88	+4	20011.0
MoO ₃	2.37	2.32	+6	20013.7
Rb ₂ MoO ₄	2.12	2.13	+6	20013.5

The experimental XANES results are shown in Fig. 7.1. The edge spectra generally show a blue shift in edge energy for the more highly oxidized species. Notably, MoS₂ is significantly more reduced than MoO₂, whereas MoO₃ and Rb₂MoO₄ have the highest edge energies. As expected, the Mo foil has the lowest absorption edge. The *K*-edge energies reported in Table 7.2 were assigned as the energy at half step height. Although some researchers prefer to assign the first inflection point in the absorption edge as the edge position, that methodology is not appropriate in this case. The various compounds in this study (metal, sulfide, oxide) exhibit significantly different line shapes at the edge, which complicates the assignment of the edge position. In Figure 7.1, a pre-edge feature exists in the spectra of highly oxidized Mo species that does not appear in the other samples. In addition, the entire absorption edge is very broad, spanning nearly 20 eV. The edge energy was therefore assigned as the

energy at half step height to remove the contribution of the pre-edge feature and average the broad range of energies throughout the edge. When assigned in this manner, the Mo foil had the lowest edge energy while the most oxidized species, MoO_3 and Rb_2MoO_4 , had the highest edge energies, which is consistent with what is generally observed in families of metal/metal oxides analyzed via XANES.⁴⁹⁻⁵³

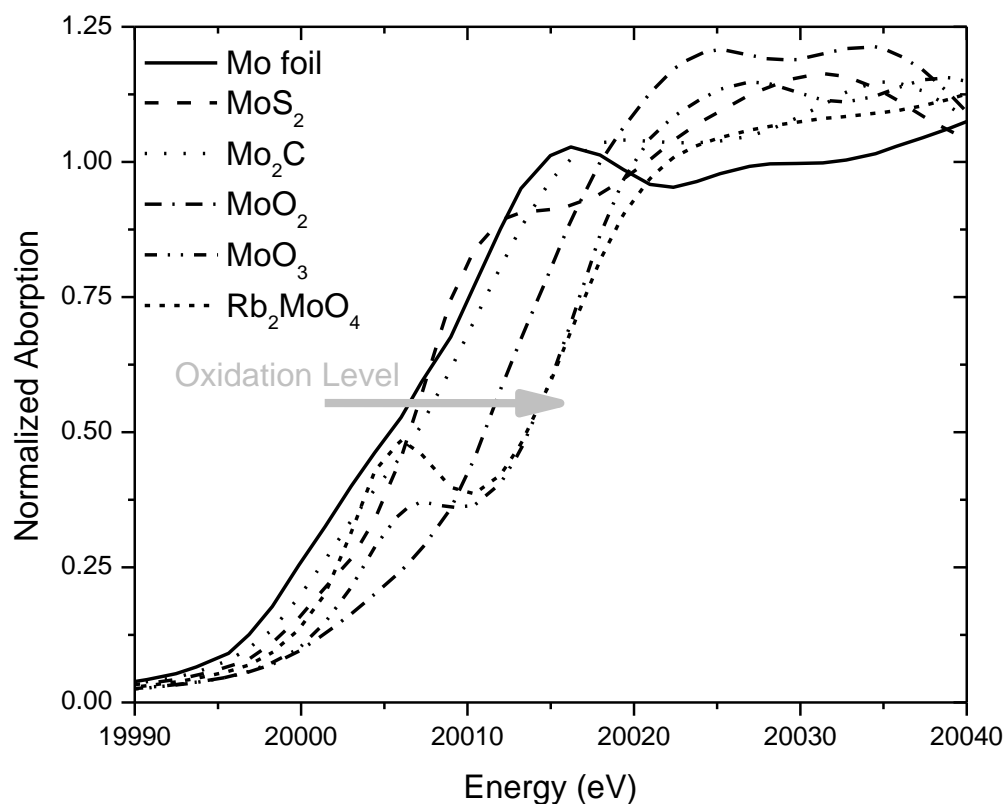


Figure 7.1: XANES data for Mo-containing compounds. Data were calibrated according to a Mo foil reference with the first derivative of the first peak assigned to 20000 eV.

To compare the different charge assignment methods, the K-edge energy (determined at half step height) is plotted as a function of the formal oxidation state, Bader charges and DDEC charges in Figs. 7.2, 7.3, and 7.4, respectively. As seen in Fig.

7.2, the formal oxidation states of Mo in these compounds do not necessarily correlate with the observed K-edge energy, with MoS_2 being an extreme outlier. This large deviation is not entirely surprising because formal oxidation state assumes all of the shared electrons are assigned to the element with larger electronegativity. This assumption works well for ionic systems, but fails in highly covalent materials.

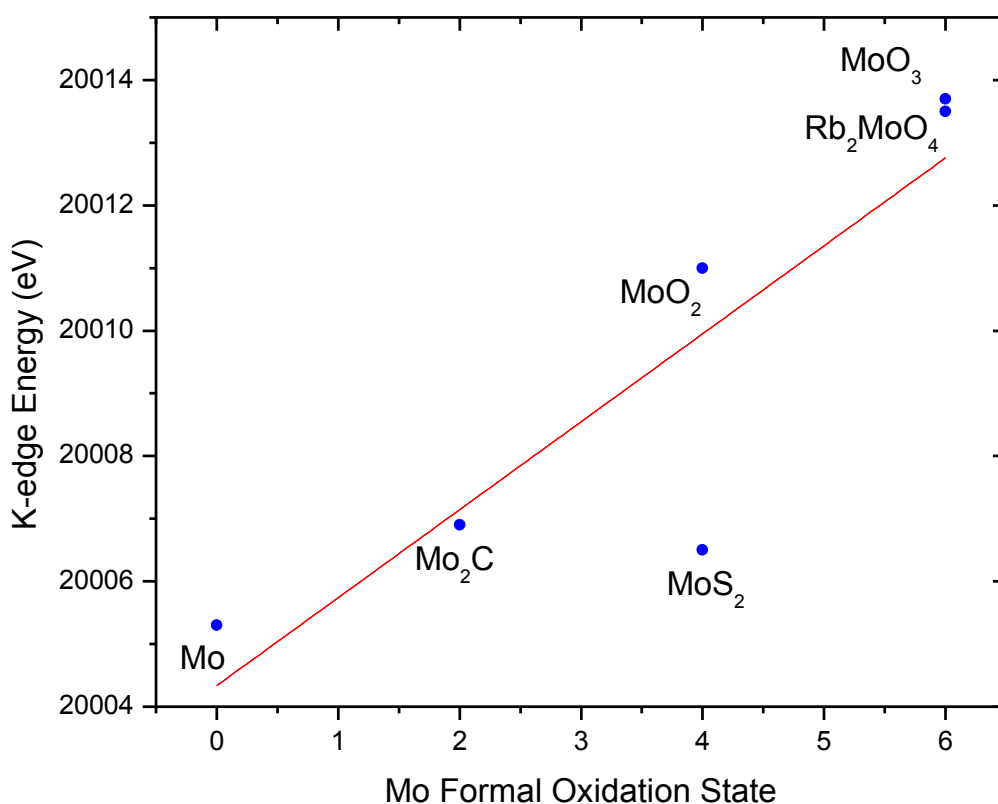


Figure 7.2: Mo K-edge energy vs. formal oxidation state for Mo-containing compounds. Fitted line has an R-squared value of 0.72155.

Figure 7.3 shows the correlation between the Bader Mo charges and the XANES observations. Although the Bader charges are better correlated with the experimental results than the formal oxidation states, the ranking of materials defined by these two

quantities are not the same. In particular, the Bader charge on Mo is considerably larger in MoS_2 than in Mo_2C , while the XANES results show the opposite trend.

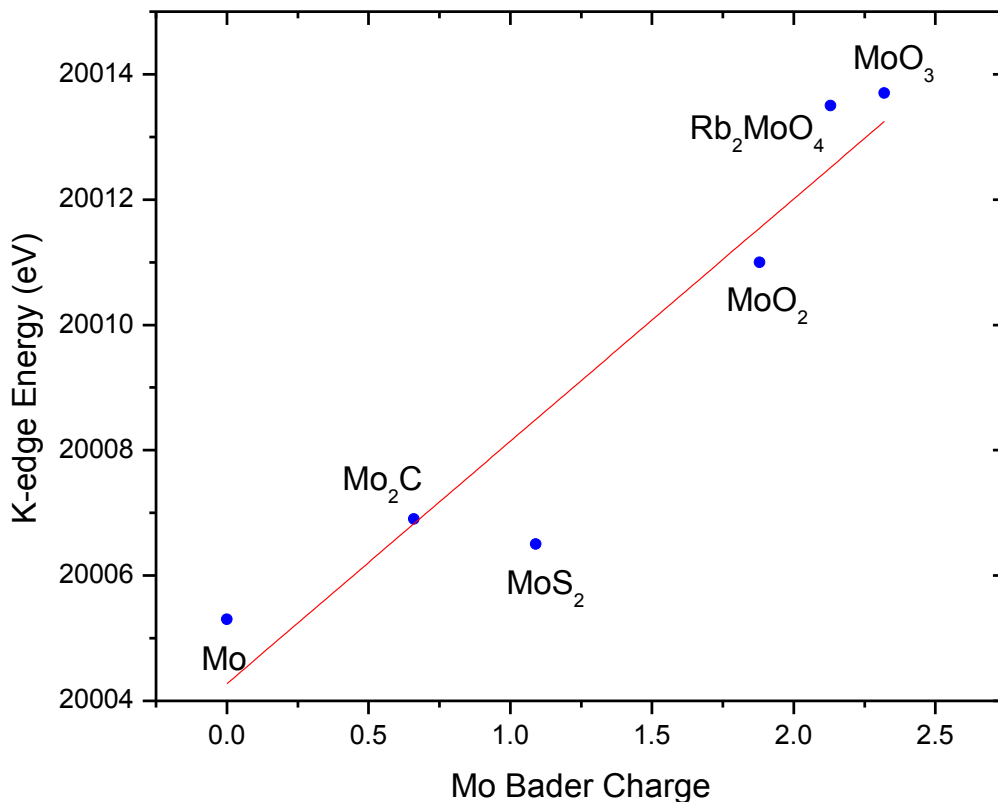


Figure 7.3: Mo K-edge energy vs. Bader charge for Mo-containing compounds. Fitted line has an R-squared value of 0.88282.

Figure 7.4 shows the correlation between the computed DDEC Mo charges and the observed XANES results. Unlike the similar results for formal oxidation states or Bader charges, the DDEC charges correlate well with the XANES results for the entire set of materials. Most critically, the DDEC approach assigns a Mo charge in MoS_2 that is smaller than the charge in Mo_2C , in agreement with the ordering given by the XANES results. Notably, among the Mo-containing materials we considered, MoS_2 is the case

where DDEC and Bader methods differ most significantly. Similar results were reported by Manz and Sholl in their comparison of different charge assignment methods for a broad range of materials¹⁵. In their examples, for dense materials (NaCl, MgH₂, Fe₂O₃, etc.), Bader charge and DDEC charge were typically in good agreement (difference in charge < 0.2), while for BN, a layered material, a substantial charge difference for B was found between Bader (+2.03)and DDEC method(+1.07). It is important to note that the Bader and DDEC methods are based on different ideas. In the Bader method, space is partitioned into non-overlapping volumes and the electron density in each volume is assigned to an atom. In the DDEC approach, the electron density associated with each atom can overlap and the assigned charges are explicitly developed to reproduce the electrostatic potential outside the electron distribution.

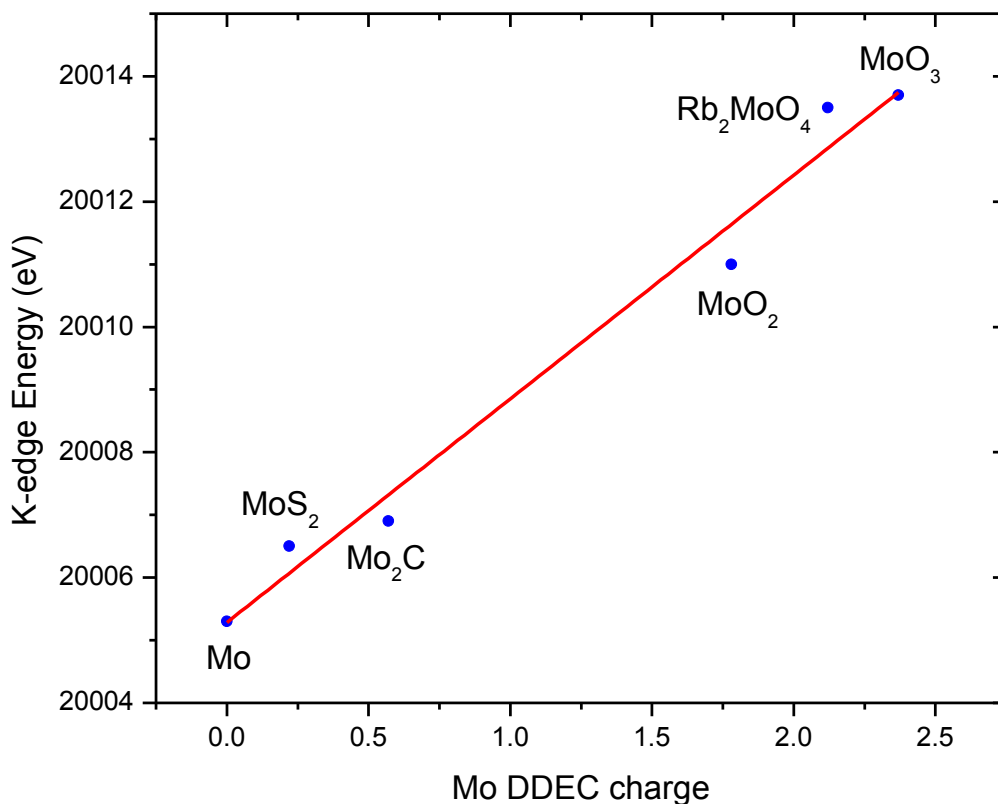


Figure 7.4: Mo K-edge energy vs. DDEC charge for Mo-containing compounds. The linear relation fitted by least squares regression is $\text{K-edge Energy} = 20005.28 + 3.57 \times \text{Mo DDEC charges}$ with an R-squared value of 0.97853.

The analysis above was performed using the K-edge energy from half the step height of the experimentally recorded data. The fraction of the step height used for this purpose is of course somewhat arbitrary. We verified that the qualitative conclusion that DDEC charges are better correlated with the experimental data than Bader charges holds for a range of the fraction of the step height that is used. For example, if the fraction is chosen to be 0.6, the R^2 value for the correlation between the experimental data and the Bader (DDEC) charges is 0.841 (0.975). If the fraction is increased to 0.7, these R^2 values are 0.773 (0.956).

The examples above do not prove that DDEC charges are “right” and Bader charges are “wrong”. As pointed out above, there is no unique way to assign point charges to individual atoms to capture all properties of the overall electron distribution of a material. With these caveats, our results support the idea that DDEC charges capture more of the physical information associated with point charges than Bader charges for these materials. The physical improvements offered by DDEC charges and the fact that DDEC charges can be computed for any example to which Bader analysis can be applied suggests that use of DDEC charges could be appropriate in a wide range of theoretical studies of dense materials.

Our results indicate that XANES edge energies can provide a simple probe of the oxidation state of metals in dense samples. We conclude with an example of using this observation to interpret experimental data.⁵⁴ Figure 7.5 shows XANES results from a $\text{MoO}_3/\text{K}_2\text{CO}_3$ catalyst supported on an Al/Mg mixed metal oxide (MMO) as it is exposed to H_2S containing syngas over the period of several days.⁵⁴ The catalyst is reacted at 310 °C, 1500 psig. Additionally the figure shows the state of the catalyst when first pretreated in 10% H_2S at 450 °C for 2 hours to generate a MoS_2 species from the supported molybdenum oxide. Although quantum chemistry calculations cannot be used, at least in any routine way, to predict the evolution of the catalyst under these conditions, the DDEC charges of these samples can still be predicted by the linear function of their K-edge energy we obtained in Fig. 7.4. As might be expected, the unreacted catalyst has an oxidation state close to the MoO_3 species. As the catalyst is reacted and exposed to sulfur, it slowly transitions to a MoO_2 -like phase. After three days on stream, that catalyst is more reduced than MoO_2 but still not as reduced as the same material when

pretreated in 10% H₂S/H₂ or a bulk MoS₂ sample. While the results presented in this manner do not provide the level of detail provided by linear combination analysis,⁵⁵ they do provide a simple, accurate “snapshot” of the state of the Mo in the catalyst. This information is especially significant because the oxidation state of the catalyst is transient.

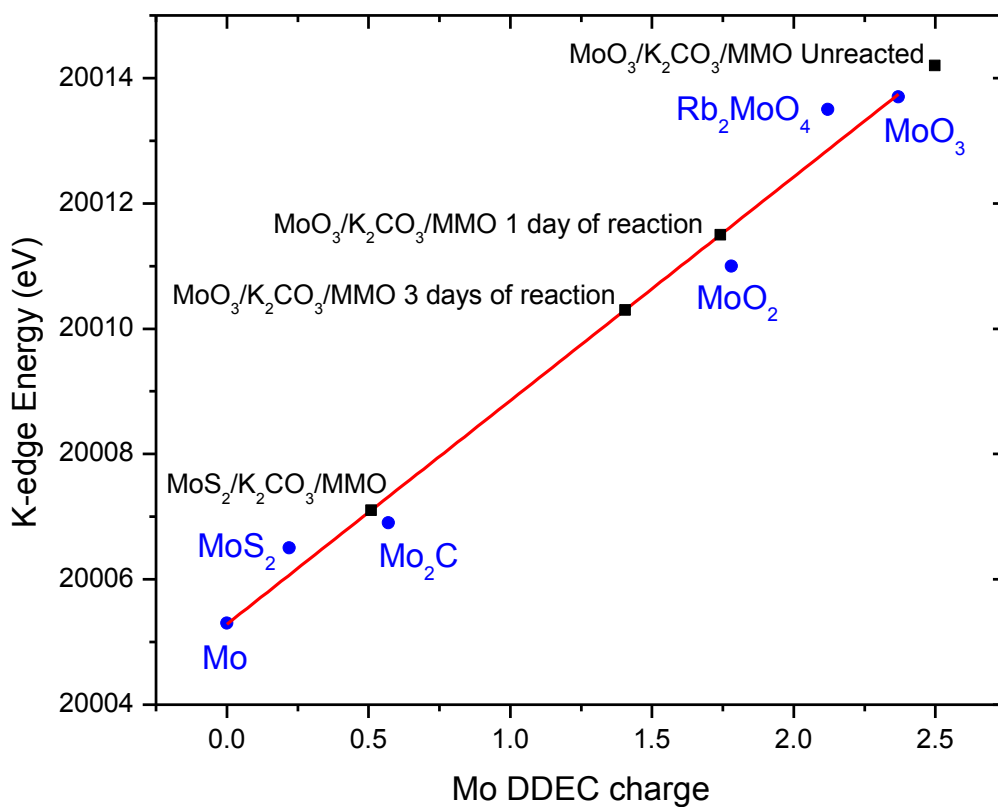


Figure 7.5: Prediction of DDEC charges of catalyst samples from their Mo K-edge energies using the linear relation found from Fig. 7.4.

7.4 Conclusions

In this chapter, XANES energies measured for several Mo containing materials were correlated with DFT computed charges from different charge assignment methods. The charges computed by quantum chemistry calculations correlated much better with the XANES results than charges estimated by formal oxidation states, which failed to describe the observed experimental trends. This is a useful example of the observation that for highly covalent materials, simply estimating charge from formal oxidation states would be inappropriate. Further, within the two charge assignment methods suitable for dense materials, namely Bader analysis and DDEC analysis, we found that DDEC charges correlated considerably better with the Mo K-edge energies derived from XANES than Bader charges. Our results suggested more physical information was captured by DDEC method for dense materials compared to the Bader charges. This is consistent with the conclusion drawn by Manz and Sholl in earlier work comparing the performance of DDEC and Bader methods for different sets of materials.¹⁵ Once a good correlation has been established between the charges on atoms in materials and XANES measurements, XANES can be used to probe the degree of oxidation and reduction in complex samples. We illustrated this idea by applying XANES to a set of supported catalysts.

7.5 References

- (1) Best, S. P.; Cheah, M. H. *Radiation Physics and Chemistry* **2010**, *79*, 185.
- (2) Rodriguez, J. A.; Hanson, J. C.; Brito, J. L.; Maiti, A. In *Applications of Synchrotron Radiation Techniques to Materials Science V*; Stock, S. R., Mini, S. M., Perry, D. L., Eds. 2000; Vol. 590, p 113.
- (3) Wilke, M.; Farges, F.; Petit, P. E.; Brown, G. E.; Martin, F. *American Mineralogist* **2001**, *86*, 714.
- (4) Farges, F.; Brown, G. E.; Rehr, J. J. *Physical Review B* **1997**, *56*, 1809.
- (5) Rockenberger, J.; zum Felde, U.; Tischer, M.; Troger, L.; Haase, M.; Weller, H. *Journal of Chemical Physics* **2000**, *112*, 4296.
- (6) McKeown, D. A.; Waychunas, G. A.; Brown, G. E. *Journal of Non-Crystalline Solids* **1985**, *74*, 325.
- (7) Mountjoy, G.; Pickup, D. M.; Wallidge, G. W.; Anderson, R.; Cole, J. M.; Newport, R. J.; Smith, M. E. *Chemistry of Materials* **1999**, *11*, 1253.
- (8) Millet, J. M. M.; Baca, M.; Pigamo, A.; Vitry, D.; Ueda, W.; Dubois, J. L. *Applied Catalysis A-General* **2003**, *244*, 359.
- (9) Shiro, Y.; Sato, F.; Suzuki, T.; Iizuka, T.; Matsushita, T.; Oyanagi, H. *Journal of the American Chemical Society* **1990**, *112*, 2921.
- (10) Berlier, G.; Pourny, M.; Bordiga, S.; Spoto, G.; Zecchina, A.; Lamberti, C. *Journal of Catalysis* **2005**, *229*, 45.
- (11) Loscher, S.; Schwartz, L.; Stein, M.; Ott, S.; Haumann, M. *Inorganic Chemistry* **2007**, *46*, 11094.
- (12) Mazalova, V. L.; Yalovega, G. E.; Soldatov, A. V. *Journal of Surface Investigation-X-Ray Synchrotron and Neutron Techniques* **2009**, *3*, 394.
- (13) Yalovega, G. E.; Shmatko, V. A.; Soldatov, A. V. *Journal of Structural Chemistry* **2010**, *51*, 1070.
- (14) Gota, S.; Gautier, M.; Douillard, L.; Thromat, N.; Duraud, J. P.; Lefevre, P. *Surface Science* **1995**, *323*, 163.
- (15) Manz, T. A.; Sholl, D. S. *Journal of Chemical Theory and Computation* **2010**, *6*, 2455.

- (16) Bader, R. F. W.; Macdougall, P. J.; Lau, C. D. H. *J. Am. Chem. Soc.* **1984**, *106*, 1594.
- (17) Bader, R. F. W.; Matta, C. F. *Journal of Physical Chemistry A* **2004**, *108*, 8385.
- (18) Henkelman, G.; Arnaldsson, A.; Jonsson, H. *Computational Materials Science* **2006**, *36*, 354.
- (19) Sholl, D. S.; Steckel, J. A. *Density functional theory: a practical introduction*; John Wiley & Sons, Inc., 2009.
- (20) Sanville, E.; Kenny, S. D.; Smith, R.; Henkelman, G. *Journal of Computational Chemistry* **2007**, *28*, 899.
- (21) Tang, W.; Sanville, E.; Henkelman, G. *Journal of Physics-Condensed Matter* **2009**, *21*.
- (22) Kim, H. W.; Jung, J.; Han, M. N.; Lim, S.; Tamada, K.; Hara, M.; Kawa, M.; Kim, Y.; Kuk, Y. *J. Am. Chem. Soc.* **2011**, *133*, 9236.
- (23) Manz, T. A.; Sholl, D. S. *Journal of Chemical Theory and Computation* **2011**, *7*, 4146.
- (24) Rogers, G. W.; Liu, J. Z. *J. Am. Chem. Soc.* **2011**, *133*, 10858.
- (25) Watanabe, T.; Manz, T. A.; Sholl, D. S. *Journal of Physical Chemistry C* **2011**, *115*, 4824.
- (26) Kresse, G.; Furthmuller, J. *Physical Review B* **1996**, *54*, 11169.
- (27) Kresse, G.; Hafner, J. *Physical Review B* **1993**, *47*, 558.
- (28) Kresse, G.; Hafner, J. *Journal of Physics-Condensed Matter* **1994**, *6*, 8245.
- (29) Perdew, J. P.; Burke, K.; Ernzerhof, M. *Physical Review Letters* **1996**, *77*, 3865.
- (30) Perdew, J. P.; Burke, K.; Ernzerhof, M. *Physical Review Letters* **1997**, *78*, 1396.
- (31) Blochl, P. E. *Physical Review B* **1994**, *50*, 17953.
- (32) Kresse, G.; Joubert, D. *Physical Review B* **1999**, *59*, 1758.
- (33) Bergerhoff, G.; Brown, I. D. **1987**.
- (34) Belsky, A.; HellenBrandt, M.; Karen, V. L.; Luksch, P. *Acta. Cryst.* **2002**, *B58*, 364.

- (35) Manz, T. A.; Sholl, D. S. *Journal of Chemical Theory and Computation* **2012**.
- (36) Woo, H. C.; Nam, I. S.; Lee, J. S.; Chung, J. S.; Kim, Y. G. *Journal of Catalysis* **1993**, *142*, 672.
- (37) Ozkan, U.; Schrader, G. L. *Journal of Catalysis* **1985**, *95*, 120.
- (38) Alonso, G.; Berhault, G.; Aguilar, A.; Collins, V.; Ornelas, C.; Fuentes, S.; Chianelli, R. R. *Journal of Catalysis* **2002**, *208*, 359.
- (39) Banares, M. A.; Pawelec, B.; Fierro, J. L. G. *Zeolites* **1992**, *12*, 882.
- (40) Ma, W. P.; Kugler, E. L.; Dadyburjor, D. B. *Energy & Fuels* **2010**, *24*, 4099.
- (41) Shou, H.; Ferrari, D.; Barton, D. G.; Jones, C. W.; Davis, R. J. *ACS Catalysis* **2012**, *2*, 1408.
- (42) Gutierrez, O. Y.; Kaufmann, C.; Lercher, J. A. *ACS Catalysis* **2011**, *1*, 1595.
- (43) Parthe, E.; Sadagopa. V *Acta Crystallographica* **1963**, *16*, 202.
- (44) Semiletov, S. A. *Kristallografiya* **1961**, *6*, 536.
- (45) Petkov, V.; Billinge, S. J. L.; Larson, P.; Mahanti, S. D.; Vogt, T.; Rangan, K. K.; Kanatzidis, M. G. *Physical Review B* **2002**, *65*.
- (46) Leisegang, T.; Levin, A. A.; Walter, J.; Meyer, D. C. *Crystal Research and Technology* **2005**, *40*, 95.
- (47) Negishi, H.; Negishi, S.; Kuroiwa, Y.; Sato, N.; Aoyagi, S. *Physical Review B* **2004**, *69*.
- (48) Kools, F. X. N.; Koster, A. S.; Rieck, G. D. *Acta Crystallographica Section B-Structural Crystallography and Crystal Chemistry* **1970**, *B 26*, 1974.
- (49) Hilbrig, F.; Michel, C.; Haller, G. L. *The Journal of Physical Chemistry* **1992**, *96*, 9893.
- (50) Ressler, T.; Wienold, J.; Jentoft, R. E.; Neisius, T. *Journal of Catalysis* **2002**, *210*, 67.
- (51) Chen, J. G.; Fruhberger, B.; Colaianni, M. L.; AVS: 1996; Vol. 14, p 1668.
- (52) Chen, J. G.; Kirn, C. M.; Fruhberger, B.; DeVries, B. D.; Touvelle, M. S. *Surface Science* **1994**, *321*, 145.

- (53) Kunkes, E. L.; Simonetti, D. A.; Dumesic, J. A.; Pyrz, W. D.; Murillo, L. E.; Chen, J. G.; Buttrey, D. J. *Journal of Catalysis* **2008**, *260*, 164.
- (54) Morrill, M. R.; Thao, N. T.; Agrawal, P. K.; Jones, C. W.; Davis, R. J.; Shou, H.; Barton, D. G.; Ferrari, D. *Catalysis Letters* **2012**, *142*, 875.
- (55) Kim, W. B.; Choi, S. H.; Lee, J. S. *Journal of Physical Chemistry B* **2000**, *104*, 8670.

APPENDIX 7.A

BULK STRUCTURE INFORMATION FOR MO CONTAINING

MATERIALS

This appendix lists the unit cells and coordinates for bulk structures of MoS₂, Mo₂C, MoO₂, MoO₃ and Rb₂MoO₄ discussed in this chapter.

Table 7.A.1: Unit cell vectors and coordinates for bulk MoS₂ in P63/mmc space group.

Lattice unit cell (Å)			
	x	y	z
a	2.744	-1.584	0.000
b	0.000	3.168	0.000
c	0.000	0.000	12.322
Coordinate			
Mo	0.333333	0.666667	0.250000
Mo	0.666667	0.333333	0.750000
S	0.333333	0.666667	0.625000
S	0.666667	0.333333	0.125000
S	0.666667	0.333333	0.375000
S	0.333333	0.666667	0.875000

Table 7.A.2: Unit cell vectors and coordinates for bulk MoS₂ in R3mH space group.

Lattice unit cell (Å)			
	x	y	z
a	1.826	0.000	6.123
b	-0.913	1.582	6.123
c	-0.913	-1.582	6.123
Coordinate			
Mo	0.000000	0.000000	0.000000
S	0.251600	0.251600	0.251600
S	0.415100	0.415100	0.415100

Table 7.A.3: Unit cell vectors and coordinates for bulk Mo₂C in Pbcn space group.

Lattice unit cell (Å)			
	x	y	z
a	4.724	0.000	0.000
b	0.000	6.004	0.000
c	0.000	0.000	5.199
Coordinate			
Mo	0.250000	0.125000	0.083000
Mo	0.250000	0.375000	0.583000
Mo	0.750000	0.375000	0.917000
Mo	0.750000	0.125000	0.417000
Mo	0.750000	0.875000	0.917000
Mo	0.750000	0.625000	0.417000
Mo	0.250000	0.625000	0.083000
Mo	0.250000	0.875000	0.583000
C	0.000000	0.325000	0.250000
C	0.500000	0.175000	0.750000
C	0.000000	0.675000	0.250000
C	0.500000	0.825000	0.750000

Table 7.A.4: Unit cell vectors and coordinates for bulk MoO₂ in P121/c1 space group.

Lattice unit cell (Å)			
	x	y	z
a	4.809	0.000	-2.881
b	0.000	4.857	0.000
c	0.000	0.000	5.624
Coordinate			
Mo	0.228100	0.993500	0.013300
Mo	0.771900	0.493500	0.486700
Mo	0.771900	0.006500	0.986700
Mo	0.228100	0.506500	0.513300
O	0.120000	0.229900	0.274800
O	0.880000	0.729900	0.225200
O	0.880000	0.770100	0.725200
O	0.120000	0.270100	0.774800
O	0.397500	0.685200	0.291800
O	0.602500	0.185200	0.208200
O	0.602500	0.314800	0.708200
O	0.397500	0.814800	0.791800

Table 7.A.5: Unit cell vectors and coordinates for bulk MoO₃ in Pbnm space group.

Lattice unit cell (Å)			
	x	y	z
a	3.961	0.000	0.000
b	0.000	13.862	0.000
c	0.000	0.000	3.697
Coordinate			
Mo	0.077000	0.100100	0.250000
Mo	0.923000	0.899900	0.750000
Mo	0.577000	0.399900	0.750000
Mo	0.423000	0.600100	0.250000
O	0.490000	0.430200	0.250000
O	0.510000	0.569800	0.750000
O	0.990000	0.069800	0.750000
O	0.010000	0.930200	0.250000
O	0.473000	0.091100	0.250000
O	0.527000	0.908900	0.750000
O	0.973000	0.408900	0.750000
O	0.027000	0.591100	0.250000
O	0.044000	0.226300	0.250000
O	0.956000	0.773700	0.750000
O	0.544000	0.273700	0.750000
O	0.456000	0.726300	0.250000

Table 7.A.6: Unit cell vectors and coordinates for bulk MoO₃ in Pbm space group.

Lattice unit cell (Å)			
	x	y	z
a	13.865	0.000	0.000
b	0.000	3.698	0.000
c	0.000	0.000	3.963
Coordinate			
Mo	0.101600	0.250000	0.084600
Mo	0.398400	0.750000	0.584600
Mo	0.601600	0.250000	0.415400
Mo	0.898400	0.750000	0.915400
O	0.437000	0.250000	0.496300
O	0.063000	0.750000	0.996300
O	0.937000	0.250000	0.003700
O	0.563000	0.750000	0.503700
O	0.086900	0.250000	0.521600
O	0.413100	0.750000	0.021600
O	0.586900	0.250000	0.978400
O	0.913100	0.750000	0.478400
O	0.218800	0.250000	0.037600
O	0.281200	0.750000	0.537600
O	0.718800	0.250000	0.462400
O	0.781200	0.750000	0.962400

Table 7.A.7: Unit cell vectors and coordinates for bulk Rb₂MoO₄ in C12/m1 space group.

Lattice unit cell (Å)			
	x	y	z
a	5.779	3.127	-2.774
b	5.779	-3.127	-2.774
c	0.000	0.000	-7.842
Coordinate			
Rb	0.848000	0.848000	0.731000
Rb	0.152000	0.152000	0.269000
Rb	0.515000	0.515000	0.763000
Rb	0.485000	0.485000	0.237000
Mo	0.174000	0.174000	0.773000
Mo	0.826000	0.826000	0.227000
O	0.084000	0.084000	0.649000
O	0.916000	0.916000	0.351000
O	0.336000	0.336000	0.623000
O	0.664000	0.664000	0.377000
O	0.380000	0.902000	0.926000
O	0.098000	0.620000	0.074000
O	0.620000	0.098000	0.074000
O	0.902000	0.380000	0.926000

CHAPTER 8

CONCLUSIONS

Syngas reactions on alkali promoted Mo₂C catalysts have been considered to be a promising way to produce alcohols in the chemical industry. However, due to the complexity of the reaction, limited knowledge of the reaction mechanism and the role of the alkali promoter was obtained experimentally. As an alternative approach, this thesis applied DFT calculations to investigate alcohol synthesis reactions on alkali promoted Mo₂C catalysts. Our results have provided fundamental information and useful insights into the bulk and surface structures of Mo₂C catalysts, syngas reactions mechanism, alkali promoter formation and its effect on the reaction selectivity.

In Chapter 3, our calculations examined the bulk and surface structures of Mo₂C to determine a representative surface structure for syngas catalysts.¹ The surface energies of several low Miller index Mo₂C surfaces were computed and used to predict the equilibrium crystal shape of Mo₂C particles. Adsorption of alkali atoms on these surfaces was investigated from DFT, and it was found the alkali atoms adsorbed most strongly on Mo₂C (001) surface. This surface was also found to favor a surface reconstruction, where surface carbons rearrange into a "honeycomb" structure, which is consistent with experimental observations.^{2,3} The reconstructed C-terminated Mo₂C (001) was chosen as a representative surface structure to be used in the following chapters.

In Chapter 4, syngas reactions on the reconstructed Mo₂C (001) surface were investigated in order to determine the elementary steps controlling the selectivity for hydrocarbons relative to alcohols. A surface reaction network was constructed where the

relevant syngas reaction elementary steps proposed in previous literature were included. The adsorption energies of the gas phase species was computed from DFT and corrected from experimental TPD results while the activation energies of all 53 elementary steps were approximated by a BEP relation. With these energies, a microkinetic model was developed where the effect of surface interactions was considered by the quasi-chemical approximation. The computed selectivity from our model was found to be in excellent agreement with experimental results from supported Mo₂C catalysts at industrially relevant temperatures and pressures. Sensitivity analysis was performed to quantify the contribution of each step to the overall selectivity, with CO insertion being identified as the step shifting reaction selectivity from hydrocarbons to alcohols.

In Chapter 5, the alkali promoter's effect on CO adsorption was investigated by DFT and IR spectroscopy.⁴ An alkali promoter formation mechanism was proposed, where RbO, produced from surface hydroxyl group by an ion exchange reaction, was suggested to be the likely form of alkali promoter. This hypothesis was supported by good agreement between the DFT computed vibrational frequency change and IR peaks shift of CO upon the addition of Rb as a promoter.

In Chapter 6, the effect of RbO on the CO insertion mechanism was examined. The CO insertion process was first examined by NEB calculations, where a [CH₃CO] transition state was identified. A charge analysis on the RbO promoter, the reactants (CO* and CH₃*), product (CH₃CO) and the [CH₃CO] transition state was performed. This analysis suggested that the dipole field created by RbO on the Mo₂C surface has opposite direction as that of the [CH₃CO] transition state and therefore will promote CO insertion mechanism.

In Chapter 7, the partial charges of Mo in several Mo-containing materials were investigated by XANES experiment and DFT with different charge assignment methods.⁵ It was found that the DDEC charges correlate better with XANES edge energy than the formal oxidation state and Bader charges. A linear relation between XANES edge energy and the DDEC charges was established and can be used to infer the oxidation state of Mo in supported catalyst samples.

In terms of the future work on this topic, several improvements can be made to our model. Firstly, the current model assumes the reactions take place when all the reaction intermediates are adsorbed on their most stable sites, although in reality, a reaction intermediate may need diffuse to a meta-stable site to react with another. Therefore, an improved model could be made in order to be capable of distinguishing different types of surface sites and considering possible diffusion of reaction intermediates for each elementary step. Secondly, as suggested in this thesis and other experimental evidence,^{6,7} surface oxygen can play an important role in syngas reactions on Mo₂C catalysts. Therefore, further studies on relevance of oxygen on surface structure of Mo₂C, alkali promoter formation, and key elementary steps could be performed. Finally, the alkali oxide group was found to be a possible form of the alkali promoter on Mo₂C catalysts in this thesis. However, the possibility of alkali promoter in other forms was not excluded. Since the alkali promoter effect depends strongly on the local adsorption geometry and charge distribution of the promoters, careful examination of alkali promoters should provide value information to understand the alkali promoter effect at a more detailed level.

References

- (1) Han, J. W.; Li, L.; Sholl, D. S. *The Journal of Physical Chemistry C* **2011**, *115*, 6870.
- (2) Lo, R. L.; Fukui, K.; Otani, S.; Iwasawa, Y. *Surface Science* **1999**, *440*, L857.
- (3) Lo, R. L.; Fukui, K.; Otani, S.; Oyama, S. T.; Iwasawa, Y. *Japanese Journal of Applied Physics Part 1-Regular Papers Short Notes & Review Papers* **1999**, *38*, 3813.
- (4) Shou, H.; Li, L.; Ferrari, D.; Sholl, D. S.; Davis, R. J. *Journal of Catalysis* **2013**, *299*, 150.
- (5) Li, L. W.; Morrill, M. R.; Shou, H.; Barton, D. G.; Ferrari, D.; Davis, R. J.; Agrawal, P. K.; Jones, C. W.; Sholl, D. S. *Journal of Physical Chemistry C* **2013**, *117*, 2769.
- (6) Oyama, S. T.; Delporte, P.; PhamHuu, C.; Ledoux, M. J. *Chemistry Letters* **1997**, 949.
- (7) St Clair, T. P.; Oyama, S. T.; Cox, D. F. *Surface Science* **2000**, *468*, 62.